LAPTH-033/25, LUPM:25-001 November 24, 2025

In-depth analysis of the clustering of dark matter particles around primordial black holes. Part II. Analytical prescriptions for spikes

Julien Lavalle a and Pierre Salati b

^aLaboratoire Univers et Particules de Montpellier (LUPM), Université de Montpellier & CNRS, Place Eugène Bataillon, 34095 Montpellier Cedex 05, France

E-mail: lavalle@in2p3.fr, pierre.salati@lapth.cnrs.fr

Abstract. Primordial black holes (PBHs) are very appealing dark matter (DM) candidates. It is highly plausible though, should they exist, that they would not make up all of the DM. Several studies showed that if the rest of DM is made of thermal particles, then these should accumulate around such PBHs, leading to the formation of very dense spikes in the radiation era. We contributed a detailed analytical study about this phenomenon, providing clear explanations as for the origin of scaling relations in the form of power-law density profiles with up to 3 different spectral indices, i.e. 3/4, 3/2, and 9/4, and 4 asymptotic regimes. Here, we further derive an approximate analytical solution that enables fast numerical predictions for the density profiles of these spikes. We also address the specific case of self-annihilating DM species and derive new approximate analytical formulae. Our approximate density yields the correct annihilation rate within $\pm 15\%$ precision. We then focus on indirect detection in the cosmic microwave background and in extragalactic gamma-rays. We shed new and subtle light on how mutually exclusive PBHs and self-annihilating DM species can really be. In particular, the discovery of a population of sub-solar PBHs would set stringent constraints on the s-wave annihilation cross-section of these particles, a point so far missed in the literature.

Keywords: Dark matter, early universe, cosmology, black holes, dark matter searches

ArXiv ePrint: 2511.xxxxx

^bLaboratoire d'Annecy de Physique Théorique (LAPTh), CNRS, Université Savoie Mont-Blanc, 9 Chemin de Bellevue, 74940 Annecy, France

Contents 1 Introduction 2 Dark matter post-collapse profiles 3 Asymptotic regimes 5 2.2Construction of the phase diagram 8 2.3 Numerical vs approximate semi-analytical results 16 Annihilation rate of the dark matter minispikes **18** Saturation density and truncation in the phase diagram 19 Behavior of the annihilation rate 20 3.3Numerical results 25 Using the soft approximation for the annihilation rate 29 3.4Observational constraints **31** Bounds on the fraction $f_{\rm BH}$ of primordial black holes 32 Cosmological γ -ray background 32 Injection of energy in the post-recombination plasma 36 4.2 Bounds on WIMP properties 41 Structure of the excluded region in the $(m_{\chi}, \langle \sigma_{\rm ann} v \rangle)$ plane 4.2.141 4.2.2Constraints on $\langle \sigma_{\rm ann} v \rangle$ from CMB angular distortions 46 4.2.3Constraints on $\langle \sigma_{\rm ann} v \rangle$ from cosmological γ -ray background 47 Conclusions **49** A Accelerating the code **51** A.1 DM cosmological density ρ_i as a function of radius \tilde{r} 51 A.2 Influence radius \tilde{r} as a function of DM cosmological density ρ_i 52 A.3 Calculation of v'53 A.4 Transition between Keplerian and radial infall regimes 54 B Effect of the Schwarzschild radius on the annihilation rate Γ_{BH} **55** B.1 Slope 0 and the saturation plateau 55 B.2 Slope 1/256

1 Introduction

Primordial black holes (PBHs) have exerted a strong (and not only gravitational) attraction over the years since their formulation by Hawking [1, 2], either as peculiar class of a stimulating theoretical object concentrating many open questions in theoretical physics (e.g. [3, 4]), or as potential dark matter (DM) candidates [5]. After a significant decrease of interest in these objects as serious contenders for DM in the late 90's due to the accumulation of observational constraints (see e.g. [6, 7] for reviews), in particular from microlensing searches (e.g. [8–10]), they gained popularity again after the discovery of gravitational waves (GW) originating in black-hole merger events rather aside from the typical mass range expected at the time [11, 12]. Even though GW observations have turned into constraints since then [13, 14], part of this renewed craze is also somewhat related to the so far unsuccessful searches for new particles beyond the standard model at colliders or with other experimental or observational strategies, although the latter do not preclude at all their existence at the moment [15–17].

Even though PBH production mechanisms are usually rather fine-tuned [18], and accumulated constraints leave only a small mass window for PBHs to be all of the DM [6, 7], contemplating the possibility that PBHs could still make a fraction of the DM is both exciting and legitimate, and actually turns out to be a very interesting theoretical question. Expressing it simply, to what extent can PBHs and other DM species co-exist? Indeed, even if subdominant in the matter content of the Universe, their co-existence as DM partners could lead to interesting phenomena, and might actually not be always possible. The role of PBHs as DM accreting objects and potential seeds of highly concentrated dark halos was envisaged in several early studies [19–21], leading in the meantime to constraints if the other DM species (assumed unique for simplicity) would be self-annihilating particles [22]—and later to studies of other potential signals through modifications of the waveforms expected in GW originating in black hole (BH) merger events [23, 24]. In all of these studies, the details of the DM density profiles accumulated around BHs is key, and so is the reliability in their determination.

A big step forward was made by Eroshenko [25] who realized that if the partner DM species is made of thermally produced particles that reach thermal equilibrium before kinetically decoupling from the plasma, then DM accretion could actually be determined on very precise footings by numerically integrating all particle orbits during the radiation domination era from kinetic decoupling on, allowing for exact (numerical) solutions in the description of this process. This very elegant method relies on two important facts: (i) thermal equilibrium fixes the initial conditions, and (ii) the local dynamics close to the BH is driven by the BH mass only. These solutions were found to be scale-invariant power-law density profiles $\propto r^{-\gamma}$, dubbed DM spikes owing to the impressively large DM densities accumulated around PBHs at such early times, further exhibiting a sharp decrease as a function of radius r. In a previous paper [26], we actually contributed a complete analytical derivation and physical understanding of the three power-law indices allowed for this accretion process, namely $\gamma = 3/4, 3/2$, and 9/4, which are fully determined by the main input parameters of the model configuration. We also corrected for a misconception in the angular part of the integral that propagated in the literature, leading to potentially large numerical errors.

The prediction of spikes in the mixed PBH-particle DM scenario is therefore fully established from theoretical grounds, and the corresponding density profiles can be determined very accurately insofar as the dynamics are fully controlled by the mass of the central PBH—a genuine linear problem as this holds. Simulations were carried out [27], though in a very

limited part of the available parameter space, which confirmed the trend of early numerical results. We note that non-linearities are still expected to manifest (i) in the outskirts of the spike region after secondary DM infall occurs during the matter domination era, i.e. when the accreted DM mass gets significant enough to backreact on itself, and (ii) in the case of self-annihilation in the central spike region. In the latter case, analytical solutions to such non-linearity can still be found if annihilation proceeds through s-wave processes [28, 29], as will be discussed later in this paper. In any case, an important question raised by this mixed DM scenario in which the partner DM species can self-annihilate is whether or not it is allowed at all by current observations. After some early work based on approximate scaling relations [21, 22], several studies using more or less controlled versions of Eroshenko's method have derived observational constraints inferred from extragalactic gamma-rays [30–32] and from the cosmic microwave background (CMB) measurements [33]. In this paper, we wish to revisit the way these constraints can be extracted on a more pedestrian and contemplative pace. Our goal is actually twofold: first, we want to revisit the relevant calculations in detail, providing analytical insights to back up both our understanding and numerical results; second, we want to come up with useful analytical approximations that would allow the interested reader to easily get numerical results correct up to a reasonably good precision, specializing in signal predictions for indirect DM searches in the extragalactic gamma-rays and in the CMB.

The paper develops as follows. In section 2, we first shortly revisit the scaling regimes featuring the postcollapse spike profiles, summarizing results we already derived in [26] but with a renewed perspective focused on the present work and aimed at justifying our analytical approximations. Next, in section 3, we enter the discussion of the spike annihilation rate. We carefully design an analytical approximation scheme, and derive our main results which are presented in the form of approximate analytical formulae. Then, in section 4, we turn to a review of the general methodology employed to derive observational constraints using both extragalactic gamma-rays and CMB measurements as our main observables. We pay a particular attention to the notion of "mutual exclusiveness" when discussing the range of parameter space where PBHs and self-annihilating DM would be either allowed or forbidden, and point to subtleties that were not clearly identified in previous works. In particular, we show that the discovery by GW observatories of a population of sub-solar PBHs would set stringent constraints on the s-wave annihilation cross-section of thermal DM species, a point so far missed in the literature. We emphasize that section 4 is more about the general methodology, and not meant to derive accurate constraints through a rigorous statistical treatment of the data. We leave this to future work. Finally, we conclude in section 5.

2 Dark matter post-collapse profiles

Three conditions are required for WIMPs to be captured by a PBH:

- (i) feeling the gravitational pull of a neighbor PBH,
- (ii) being free streaming through the ambient plasma, non-relativistic, and collisionless,
- (iii) having a velocity smaller than the local escape velocity.

To commence, DM particles must lie inside the so-called sphere of influence of the object, where they can feel its gravitational pull. In the early universe, space is actually filled with a dense plasma inside which the attraction of a PBH is overcome by the overall expansion beyond a critical distance $r_{\rm inf}$ identified with the radius of that sphere of influence. The

relation between $r_{\rm inf}$ and the black hole mass $M_{\rm BH}$ takes the form [27]

$$M_{\rm BH} = \frac{16\pi}{3\eta_{\rm ta}} r_{\rm inf}^3 \, \rho_{\rm tot} \,,$$
 (2.1)

where the coefficient $\eta_{\rm ta}$ has been found equal to 1.086 in [26]. As time goes on, the universe cools down, the energy density $\rho_{\rm tot}$ of the primordial plasma drops and the radius of influence $r_{\rm inf}$ increases. Should they feel the PBH attraction, DM species must also move freely inside the ambient medium. At early times, they collide onto the constituents of the primordial plasma and are pulled away from the black hole by the overall expansion. This drag stops at kinetic decoupling, which occurs when the exchange of energy between DM and surrounding plasma becomes slower than the expansion itself. WIMPs stream freely afterwards and move unimpeded. Thermalization between the radiation bath and DM breaks at kinetic decoupling, leaving WIMP momenta decreasing in time as they only undergo redshift. The last condition bears on DM velocities which should not exceed, at injection, the local escape velocity from the PBH.

During the radiation dominated era, DM skirts start building up around PBHs as soon as DM undergoes kinetic decoupling. This occurs at plasma temperature $T_{\rm kd}$. We define the kinetic decoupling parameter $x_{\rm kd}$ as the ratio $m_\chi/T_{\rm kd}$, with m_χ the WIMP mass. At kinetic decoupling, the particles lying inside the sphere of influence of a PBH start falling onto it. As time passes on, layers lying farther away from the PBH start falling in turn, hence an onion like structure of the pre-collapse DM distribution whose profile is well approximated by

$$\rho_i(r_i) \simeq \begin{cases} \rho_i^{\text{kd}} & \text{if } r_i \le r_{\text{kd}}, \\ \rho_i^{\text{kd}} \left(r_i / r_{\text{kd}} \right)^{-9/4} & \text{if } r_{\text{kd}} \le r_i \le r_{\text{eq}}. \end{cases}$$
 (2.2)

At kinetic decoupling, the cosmological DM density is $\rho_i^{\rm kd}$ while the radius of the sphere of influence is $r_{\rm kd}$. At matter-radiation equality, that radius is $r_{\rm eq}$ and the accretion of DM species stops to be considered as the radiation era comes to an end.

The pre-collapse DM velocities β_i follow a Maxwellian distribution $\mathcal{F}_{\mathrm{MB}}(\beta_i|r_i)$ with dispersion velocity σ_i . Particles injected at radii $r_i \leq r_{\mathrm{kd}}$ have the 1D dispersion velocity of DM at kinetic decoupling, i.e. $\sigma_{\mathrm{kd}} = x_{\mathrm{kd}}^{-1/2}$. Those trapped farther away at radius $r_i > r_{\mathrm{kd}}$ start orbiting the PBH at a later cosmic time t_i . After kinetic decoupling occurred, their dispersion velocity σ_i has been redshifted, hence a unique relation between σ_i , t_i and eventually r_i as discussed in [26]. According to Liouville's theorem, σ_i scales with r_i like $\rho_i^{1/3}$. At matter-radiation equality, the DM dispersion velocity has decreased down to σ_{eq} .

The initial state of a WIMP that feels for the first time the gravitational pull of a PBH is specified by the radius r_i , the velocity β_i and the angle $\theta_i = (\vec{\beta_i}, \vec{r_i})$ between the injection and radial directions. From now on, it is convenient to define the reduced radius \tilde{r}_i as the physical radius r_i expressed in units of the PBH Schwarzschild radius $r_S = 2GM_{\rm BH}/c^2$. Note also that velocities are expressed in units of the speed of light c. The particle is trapped provided that the parameter $u \equiv \beta_i^2 \tilde{r}_i$, describing the ratio of kinetic to potential energy, is less than 1. It reaches the radius \tilde{r} if $u \geq 1 - X$, where X stands for the ratio \tilde{r}_i/\tilde{r}_i , i.e. the destination potential to initial potential ratio. In the extreme case where u = 1 - X, the destination radius \tilde{r} is the apocenter of a purely radial trajectory. If both conditions are met, energy and angular momentum conservation implies that the radial velocity β_r at radius \tilde{r}

fulfills the equation

$$\sin^2 \theta_i + \left\{ \frac{\tilde{r}^2}{\tilde{r}_i^2 \beta_i^2} \right\} \beta_r^2 = \frac{\tilde{r}^2}{\tilde{r}_i^2} \left\{ 1 + \frac{1}{\beta_i^2} \left(\frac{1}{\tilde{r}} - \frac{1}{\tilde{r}_i} \right) \right\} \equiv 1 - \mathcal{Y}_{\rm m} \,. \tag{2.3}$$

This relation is a definition for the quantity \mathcal{Y}_m which plays an important role in the post-collapse DM profile. For obscure reasons, \mathcal{Y}_m has been constrained to be only positive in the past literature. Allowing it to be also negative, as it should, is not only the correct way to define it, but is actually paramount to avoid large numerical errors [26].

The contribution of each WIMP to the minispike density inside the layer of radius \tilde{r} and thickness $d\tilde{r}$ is proportional to the fraction $2dt/T_{\rm orb}$ of the orbital time spent inside it. The duration dt depends on the radial velocity β_r , which depends itself on the injection angle θ_i and on the parameter $\mathcal{Y}_{\rm m}$. The orbital period $T_{\rm orb}$ follows Kepler's third law of planetary motion. At fixed \tilde{r}_i and β_i , it does not depend on θ_i since it depends only on total energy, not on angular momentum. Equipped with all these notations, the post-collapse DM density at radius \tilde{r} can be readily derived as the integral over the initial phase space

$$\rho(\tilde{r}) = \frac{4}{\tilde{r}} \iint \tilde{r}_i \, d\tilde{r}_i \, \rho_i(\tilde{r}_i) \times d\beta_i^2 \, \mathcal{F}_{MB}(\beta_i | r_i) \times \left\{ \frac{1}{\tilde{r}_i} - \beta_i^2 \right\}^{3/2} \times \mathcal{J}(\mathcal{Y}_m) \,, \tag{2.4}$$

where the function $\mathcal{J}(\mathcal{Y}_m)$ is defined as the angular integral

$$\mathcal{J}(\mathcal{Y}_{\mathrm{m}}) = \int_{0}^{\theta_{i}^{0}} \frac{\mathrm{d}(-\cos\theta_{i})}{\sqrt{\cos^{2}\theta_{i} - \mathcal{Y}_{\mathrm{m}}}}.$$
 (2.5)

In the previous expression, the upper bound θ_i^0 is equal to $\arccos(\sqrt{\mathcal{Y}_m})$ if $\mathcal{Y}_m \geq 0$, and to $\pi/2$ if $\mathcal{Y}_m \leq 0$. A straighforward calculation yields

$$\mathcal{J}(\mathcal{Y}_{\mathrm{m}}) = \ln\left(1 + \sqrt{1 - \mathcal{Y}_{\mathrm{m}}}\right) - \frac{1}{2}\ln|\mathcal{Y}_{\mathrm{m}}|. \tag{2.6}$$

In spite of its simplicity, the numerical integration of relation (2.4) turns out to be tricky. The angular integral $\mathcal J$ diverges logarithmically when $\mathcal Y_{\rm m}=0$. The Gauss-Legendre method is by far the most stable way to compute the post-collapse DM density $\rho(\tilde r)$ but is time consuming. That is why we have devised a fast and accurate way to get $\rho(\tilde r)$, enabling further studies of the cosmological and astrophysical implications of DM minispikes around PBHs to be rapidly performed.

2.1 Asymptotic regimes

As featured in Fig. 4 of [26], the post-collapse DM profiles exhibit a rich diversity of behaviors depending on radius \tilde{r} and PBH mass $M_{\rm BH}$. The minispikes extend from the Schwarzschild radius $\tilde{r}_{\rm S} \equiv 1$ up to the radius of influence at matter-radiation equality $\tilde{r}_{\rm eq} \propto M_{\rm BH}^{-2/3}$. The DM profiles are power laws $\rho(\tilde{r}) \propto \tilde{r}^{-\gamma}$ where the slope γ can take three distinct values, i.e. $\gamma = 3/4$, 3/2 and 9/4. As showed in the analysis presented in [26], four distinct asymptotic behaviors can be identified, on which we will build our approximation. For each of these regimes, the expression of the DM profile is very simple, and involves a specific integral $\mathcal{T}^{\rm asy}$ running over a portion of the (X,u) phase space. As mentioned above, WIMP injection is described by the parameters $u \equiv \beta_i^2 \tilde{r}_i$ and $X \equiv \tilde{r}_i/\tilde{r}$, while the injection angle θ_i is integrated out in function \mathcal{J} whose argument $\mathcal{Y}_{\rm m}$ can be expressed in terms of X and u as

$$\mathcal{Y}_{\rm m} = 1 - \frac{1}{uX} + \frac{1}{X^2} \left(\frac{1}{u} - 1\right).$$
 (2.7)

• The caustic regime $\gamma = 3/4$

This regime dominates close to the PBH, for radii \tilde{r} much smaller than the kinetic decoupling parameter $x_{\rm kd}$. The dominant contribution to the minispike density comes from the accumulation of orbits around those whose periastrons and apoastrons are respectively located at \tilde{r} and \tilde{r}_i , and for which the angular integral \mathcal{J} diverges. These trajectories are piled up on \tilde{r} where they create a caustic. The slope 3/4 translates therefore some kind of resonant behavior where the DM density at \tilde{r} is built essentially from trajectories for which this radius behaves like an attractor. The post-collapse DM density can be expressed as

$$\rho_{3/4}(\tilde{r}) = \frac{\mathcal{A}_{3/4}}{\tilde{r}^{3/4}} \quad \text{with} \quad \mathcal{A}_{3/4} = \sqrt{\frac{2}{\pi^3}} \frac{\rho_i^{\text{kd}}}{\sigma_{\text{led}}^{3/2}} \zeta^{3/4} \mathcal{I}_{3/4}^{\text{asy}}, \tag{2.8}$$

where $\rho_i^{\rm kd}$ and $\sigma_{\rm kd}$ stand respectively for the cosmological density and dispersion velocity of DM at kinetic decoupling. The parameter ζ is equal to $2\Gamma(7/4)^{4/3} \simeq 1.78713$ while the phase space integral $\mathcal{I}_{3/4}^{\rm asy}$ is defined as

$$\mathcal{I}_{3/4}^{asy} = \frac{2}{3} \int_{-\infty}^{1} d\mathcal{Y}_{m} \frac{\mathcal{J}(\mathcal{Y}_{m})}{(1 - \mathcal{Y}_{m})^{5/4}} \simeq 4.18879.$$
 (2.9)

The coefficient $\mathcal{A}_{3/4}$ does not depend on $M_{\rm BH}$, hence a universal behavior of the DM density once expressed as a function of the reduced radius \tilde{r} .

• The Keplerian regime $\gamma = 3/2$

For light PBHs and large radii \tilde{r} , WIMPs are injected with velocities large with respect to the local escape speed at \tilde{r}_i . As a consequence, the DM species that are captured have a flat distribution in velocity space. The integral (2.4) over phase space simplifies into

$$\rho_{3/2}(\tilde{r}) = \frac{\mathcal{A}_{3/2}}{\tilde{r}^{3/2}} \text{ where } \mathcal{A}_{3/2} = \sqrt{\frac{2}{\pi^3}} \frac{\rho_i^{\text{kd}}}{\sigma_{\text{kd}}^3} \mathcal{I}_{3/2}^{\text{asy}}.$$
(2.10)

The phase space integral $\mathcal{I}_{3/2}^{\mathrm{asy}}$ can be expressed as

$$\mathcal{I}_{3/2}^{\text{asy}} = \int_0^{+\infty} \frac{\mathrm{d}X}{X^{3/2}} \int_{u_{\text{inf}}}^1 \mathrm{d}u \ (1 - u)^{3/2} \ \mathcal{J} \simeq 1.04720 \,, \tag{2.11}$$

where $u_{\rm inf} = \max\{0, (1-X)\}$. In this regime, the only scale dependence is set by the orbital period $T_{\rm orb}$. The post-collapse density $\rho(\tilde{r})$ scales like $1/T_{\rm orb}$, which is in turn proportional to $\tilde{r}^{-3/2}$ according to Kepler's third law of celestial mechanics, hence the slope $\gamma = 3/2$. Notice that the coefficient $\mathcal{A}_{3/2}$ does not depend on $M_{\rm BH}$, as in the 3/4 caustic regime. The post-collapse DM profile $\rho(\tilde{r})$ is also universal.

• Radial infall starting at kinetic decoupling $\gamma = 3/2$

For the heaviest PBHs, i.e. above the critical value M_2 defined hereafter, and at intermediate radii \tilde{r} smaller than the radius of influence $\tilde{r}_{\rm kd}$ at kinetic decoupling, the density profile also follows a slope 3/2, although for completely different reasons. In this regime of heavy black hole masses, the WIMP dispersion velocity at injection is everywhere smaller than the local escape speed. The post-collapse density results from the radial infall of the DM population starting already at kinetic decoupling. In this limit, we infer the power law

$$\rho'_{3/2}(\tilde{r}) = \frac{\mathcal{A}'_{3/2}}{\tilde{r}^{3/2}} \quad \text{where} \quad \mathcal{A}'_{3/2} = \sqrt{\frac{2}{\pi^3}} \, \rho_i^{\text{kd}} \, \tilde{r}_{\text{kd}}^{3/2} \, \mathcal{I}_{3/2}^{\text{asy}}' \,. \tag{2.12}$$

The phase space integral $\mathcal{I}_{3/2}^{\text{asy}\,\prime}$ is showed in [26] to be well approximated by $2\sqrt{2\pi} \simeq 5.01326$. In this regime, the profile is no longer universal. The coefficient $\mathcal{A}_{3/2}'$ depends actually on PBH mass through \tilde{r}_{kd} , and scales like $1/M_{\text{BH}}$.

• Radial infall starting after kinetic decoupling $\gamma = 9/4$

For PBHs with masses $M_{\rm BH}$ larger than the critical value M_1 defined hereafter, the dispersion velocity of DM at injection can be smaller than the local escape speed in the outer regions of the minispike, i.e. for radii \tilde{r} larger than the radius of influence $\tilde{r}_{\rm kd}$ at kinetic decoupling. The post-collapse density at \tilde{r} results in that case from the radial infall of the successive layers of the onion-like initial distribution located above \tilde{r} . The DM profile is given by

$$\rho_{9/4}(\tilde{r}) = \sqrt{\frac{2}{\pi^3}} \, \rho_i(\tilde{r}) \, \mathcal{I}_{9/4}^{\text{asy}} \,. \tag{2.13}$$

In this expression, $\rho_i(\tilde{r})$ is the cosmological pre-collapse DM density at the precise moment when \tilde{r} becomes the radius of influence of the PBH. Neglecting the evolution in time of the thermodynamical coefficients g_{eff} and h_{eff} that come into play in the calculation of the effective number of degrees of freedom of the energy and entropy densities of the primordial plasma, we can approximate $\rho_i(\tilde{r})$ by the second relation of Eq. (2.2) which yields the scaling $\tilde{r}^{-9/4}$ and the slope 9/4. In appendix A.1, we go beyond this approximation and derive the exact relation between ρ_i and \tilde{r} . The phase space integral is equal to

$$\mathcal{I}_{9/4}^{\text{asy}} = \sqrt{2\pi} \left\{ \int_{1}^{+\infty} \frac{\mathrm{d}X}{X^{5/4}} \frac{1}{\sqrt{X-1}} \equiv B(3/4, 1/2) \right\} = \frac{8\pi^2}{\Gamma(1/4)^2} \simeq 6.00658.$$
 (2.14)

At fixed \tilde{r} , the post-collapse DM density $\rho(\tilde{r})$ scales approximately like $\tilde{r}_{\rm kd}^{9/4} \propto 1/M_{\rm BH}^{3/2}$. Like in the previous regime, profiles are no longer universal.

Two critical values for the PBH mass $M_{\rm BH}$ can be defined, as briefly mentioned in the previous review of the various asymptotic regimes. The mass M_1 is the maximal value below which the DM average velocity $\bar{\beta}_i$ at injection is everywhere larger than the local escape speed from the radius of influence \tilde{r}_i . The mass M_2 is the exact opposite. It corresponds to the minimal value of $M_{\rm BH}$ above which the DM average velocity $\bar{\beta}_i$ at injection is everywhere smaller than the local escape speed from the radius \tilde{r}_i . Quantitative definitions of M_1 and M_2 have already been given in [26]. In this article, we adopt a more phenomenological point of view and derive these critical values from the phase diagram in section 2.2.

The post-collapse DM profile $\rho(\tilde{r})$ depends on how the PBH mass $M_{\rm BH}$ compares with M_1 and M_2 , hence three mass domains.

- (i) Very light PBHs $M_{\rm BH}$ < M_1 . The inner regions are dominated by a universal profile with slope 3/4 (caustic regime) while the outer regions follow a universal profile with slope 3/2 (Keplerian regime).
- (ii) Heavy PBHs $M_1 < M_{\rm BH} < M_2$. The behavior of the DM density in the inner regions of the minispike is the same as before, while the outer regions undergo radial infall and follow a non-universal profile with slope 9/4. The heavier the PBH, the thicker the region dominated by radial infall.
- (iii) Heaviest PBHs M_2 < $M_{\rm BH}$. Black holes are so heavy that radial infall occurs as early as kinetic decoupling and implies regions located well below the radius $\tilde{r}_{\rm kd}$. Very small radii are still dominated by the caustic regime with slope 3/4. As \tilde{r} increases, the minispike profile departs from this universal behavior and follows the radial infall regimes with slopes 3/2 below $\tilde{r}_{\rm kd}$ and 9/4 above.

2.2 Construction of the phase diagram

In this article, we give analytical prescriptions for a fast derivation of the post-collapse DM density profile $\rho(\tilde{r})$. We build an approximation from the asymptotic behaviors reviewed above. An efficient calculation requires to determine rapidly which of these regimes applies to the particular values of PBH mass and radius under scrutiny. This is where the phase diagram comes into play. In this section, we construct a map in the $(\tilde{r}, M_{\rm BH})$ plane where we delineate the various domains inside which each asymptotic regime dominates. Such a map will also allow us to get a better understanding of the minispike behavior once DM self-annihilations are taken into account in section 3.

The formation of minispikes around PBHs starts at WIMP kinetic decoupling and goes on until matter-radiation equality, after which the process is no longer considered. After equality, the accreted DM masses could actually grow beyond the PBH seed masses, such that non-linearities would be expected in the building up of these outer halos which could no longer be described by our analytical calculation. However, the very central parts of the spikes that we accurately describe are so dense that they can hardly be affected by this external dynamics. Accordingly, in the $(\tilde{r}, M_{\rm BH})$ plane of Fig. 1, the phase diagram extends rightward up to the radius of influence $\tilde{r}_{\rm eq}$ at matter-radiation equality. This radius represents the outer boundary of minispikes and corresponds to the solid red line of the plot. Borrowing from the Planck collaboration [34] the cosmological parameters $\Omega_{\rm b}h^2=0.02237$, $\Omega_{\rm dm}h^2=0.1200$ and $z_{\rm eq}=3,402$ while using a cosmic microwave background temperature of 2.72548 K [35], we can use relation (2.1) to get

$$\tilde{r}_{\rm eq}(m) = \tilde{r}_{\rm eq}^0 \, m^{-2/3} \quad \text{where} \quad m \equiv M_{\rm BH}/{\rm M}_{\odot} \,.$$
 (2.15)

At matter-radiation equality, the reduced radius of influence of a 1 M $_{\odot}$ black hole is found to be $\tilde{r}_{\rm eq}^0=2.87\times 10^{11}$. Since the Schwarzschild radius of such an object is $r_{\rm S}^0=2.95$ km, the corresponding physical radius $r_{\rm eq}^0$ is equal to 8.49×10^{11} km $\simeq 5,67$ AU. At that time, the plasma temperature is $T_{\rm eq}=9,275$ K $\equiv 7.99\times 10^{-10}$ GeV, and the cosmological DM density is $\rho_i^{\rm eq}\simeq 8.88\times 10^{-20}$ g cm $^{-3}$.

More generally, notice that the physical radii of influence increase like $m^{1/3}$ while the reduced radii decrease like $m^{-2/3}$. In the $(\tilde{r}, M_{\rm BH})$ plane, the reduced radius of influence $\tilde{r}_{\rm inf}$ at cosmological time t_i obeys the equation

$$m^2 \tilde{r}_{\rm inf}^3 \left\{ \frac{\rho_{\rm tot}(t_i)}{\rho_{\rm S}^0} \right\} = 1, \qquad (2.16)$$

where $\rho_{\rm tot}$ is the energy density of the plasma. This density can be expressed in units of the benchmark value

$$\rho_{\rm S}^0 = \frac{3\eta_{\rm ta}}{16\pi} \, \frac{1 \,{\rm M}_{\odot}}{(r_{\rm S}^0)^3} \simeq 5.00 \times 10^{15} \,{\rm g \, cm}^{-3} \,. \tag{2.17}$$

We find that \tilde{r}_{inf} is actually proportional to $m^{-2/3}$ with a scaling factor depending on cosmological time t_i , or alternatively on plasma temperature T_i . We will come back to this point very shortly.

Last but not least, we will hereafter define the boundary between domains a and b as the location in the phase diagram where the corresponding asymptotic expressions for the DM density are equal

$$\rho_{\mathbf{a}}(\tilde{r}, m) = \rho_{\mathbf{b}}(\tilde{r}, m). \tag{2.18}$$

This equation yields a unique relation between radius and PBH mass which is represented by an orange line in the $(\tilde{r}, M_{\rm BH})$ plane of Fig. 1. Before we introduce the notion of triple point, we emphasize that even though asymptotic regimes allow us to identify three different slopes for the spike profile, the slope of index 3/2 has two different origins, and therefore characterizes two different areas in the phase diagram of Fig. 1. In the following, we will distinguish these two 3/2 slopes when defining contact points or contact regions, hence the definition of two different triple points below.

• Triple point A and critical mass M_2

To start our exploration of the phase diagram, we must first define the properties of the DM particle, i.e. its mass m_{χ} and kinetic decoupling parameter $x_{\rm kd} = m_{\chi}/T_{\rm kd}$. In the illustration of Fig. 1, we have selected a 1 TeV WIMP with a kinetic decoupling temperature of 100 MeV. Calculating the plasma energy density at that time and using Eq. (2.16) yields, for a 1 $\rm M_{\odot}$ black hole, the radius of influence $\tilde{r}_{\rm kd}^0 = 3.42$, which physically amounts to 10.1 km.

At the triple point A of the phase diagram, both regimes with slope 3/2 (Keplerian and radial infall), and the caustic regime with slope 3/4, have same asymptotic DM densities

$$\rho_{3/4}(\tilde{r}_{A}) = \rho_{3/2}(\tilde{r}_{A}) = \rho'_{3/2}(\tilde{r}_{A}, m_{A}). \tag{2.19}$$

Recasting this relation as

$$\frac{\mathcal{A}_{3/4}}{\tilde{r}_{\rm A}^{3/4}} = \frac{\mathcal{A}_{3/2}}{\tilde{r}_{\rm A}^{3/2}} = \frac{\mathcal{A}'_{3/2}(m_{\rm A})}{\tilde{r}_{\rm A}^{3/2}},\tag{2.20}$$

we readily infer from Eqs. (2.8), (2.10) and (2.12) the coordinates of A in the $(\tilde{r}, M_{\rm BH})$ plane

$$\tilde{r}_{A} = \frac{x_{kd}}{\zeta} \left\{ \frac{\mathcal{I}_{3/2}^{asy}}{\mathcal{I}_{3/4}^{asy}} \right\}^{4/3} \text{ and } m_{A} \equiv \frac{M_{A}}{M_{\odot}} = \frac{\mathcal{I}_{3/2}^{asy}}{\mathcal{I}_{3/2}^{asy}} \left\{ \frac{\tilde{r}_{kd}^{0}}{x_{kd}} \right\}^{3/2}.$$
(2.21)

In the previous expression, the first equality is obtained by identifying $\rho_{3/4}$ with $\rho_{3/2}$. The boundary between the asymptotic regimes with slopes 3/4 (caustic) and 3/2 (Keplerian) corresponds in the phase diagram of Fig. 1 to a vertical line that goes all the way up to point A, where it stops. Its position does only depend on the kinetic decoupling parameter $x_{\rm kd}$ insofar as the ratio $\tilde{r}_{\rm A}/x_{\rm kd}$ is always equal to 8.81×10^{-2} .

The second identity is derived by equating $\rho_{3/2}$ (Keplerian) with $\rho'_{3/2}$ (radial infall) and yields the PBH mass $M_{\rm A}$. It also defines the frontier between these asymptotic regimes, which appears in Fig. 1 as a horizontal line connecting points A and B₂, where B₂ is yet another triple point to be discussed in more detail later. That border separates what we call the heaviest PBHs from the others. That is why we are tempted to identify the corresponding critical mass M_2 with $M_{\rm A}$. In the case of Fig. 1, we find a numerical value of $3.03 \times 10^{-5}~{\rm M}_{\odot}$.

Although this definition may seem ad hoc, we insist that it corresponds to the physical prescription given in section 2.1. Actually, around a PBH with mass $M_2 \equiv M_A$, the radius of the sphere of influence at kinetic decoupling is

$$\tilde{r}_{\rm kd}(m_2) = \tilde{r}_{\rm kd}^0 \, m_2^{-2/3} \,.$$
 (2.22)

The second identity of Eq. (2.21) can be recast into

$$\sigma_{\rm kd}^2 \tilde{r}_{\rm kd}(m_2) \equiv \frac{\tilde{r}_{\rm kd}(m_2)}{x_{\rm kd}} = \left\{ \frac{\mathcal{I}_{3/2}^{\rm asy}}{\mathcal{I}_{3/2}^{\rm asy}} \right\}^{2/3} \simeq 0.352.$$
 (2.23)

This expression is universal and does not depend on DM properties. Notice that a WIMP injected at radius r_i with initial velocity v_i is characterized by the kinetic-to-potential energy ratio

$$\frac{K_i}{|U_i|} = \frac{v_i^2/2}{GM_{\rm BH}/r_i} = \beta_i^2 \tilde{r}_i \equiv u \,.$$
 (2.24)

Replacing the velocity β_i by its root mean square $\bar{\beta}_i \equiv \sqrt{3}\sigma_i$, with σ_i the local 1D dispersion velocity, we conclude that most WIMPs in the surroundings of a PBH are captured provided that

$$\frac{\overline{K_i}}{|U_i|} = 3\sigma_i^2 \tilde{r}_i \le 1. \tag{2.25}$$

The kinetic-to-potential energy ratio is maximal on the surface of the sphere of influence at kinetic decoupling. For a PBH with critical mass M_2 , this yields

$$3\sigma_{\rm kd}^2 \tilde{r}_{\rm kd}(m_2) \simeq 1.056$$
. (2.26)

The ratio of the WIMP average velocity to the local escape speed, both taken at the radius $\tilde{r}_{\rm kd}$, is equal to 1.028. This result, obtained essentially from phenomenological arguments based on asymptotic expressions of the minispike density profile, is very close to the value of 1 implied by the physical definition of M_2 given in section 2.1. This remarkable agreement makes us confident that our approach based on the phase diagram is robust.

The frontier \tilde{r}_t between the asymptotic regimes with slopes 3/4 (caustic) and 3/2 (radial infall) is given by the condition

$$\rho_{3/4}(\tilde{r}_{t}) = \rho'_{3/2}(\tilde{r}_{t}, m)$$
 or alternatively by $\frac{\mathcal{A}_{3/4}}{\tilde{r}_{t}^{3/4}} = \frac{\mathcal{A}'_{3/2}(m)}{\tilde{r}_{t}^{3/2}}.$ (2.27)

The PBH mass must be larger than M_2 for the radial infall regime with slope 3/2 to exist. The last expression yields the radius of transition

$$\tilde{r}_{\rm t} = \tilde{r}_{\rm A} (m/m_2)^{-4/3} \equiv \tilde{r}_{\rm A} \left\{ \frac{M_{\rm BH}}{M_2} \right\}^{-4/3}.$$
 (2.28)

As featured in Fig. 1, this radius becomes unphysical at very large PBH masses as it lies in the shaded gray vertical band below the Schwarzschild radius.

• Definition of v' and triple point B_2

The transition between the two radial infall asymptotic regimes, with respective slopes 3/2 and 9/4, corresponds to the line in the phase diagram where

$$\rho_{3/2}'(\tilde{r}_{t}, m) = \rho_{9/4}(\tilde{r}_{t}, m). \tag{2.29}$$

Neglecting the evolution of the thermodynamical coefficients g_{eff} and h_{eff} around the plasma temperature T_{kd} at kinetic decoupling, we can use the second relation of Eq. (2.2) to calculate the cosmological DM density $\rho_i(\tilde{r})$ at injection. This yields the asymptotic density

$$\rho_{9/4}(\tilde{r}, m) = \sqrt{\frac{2}{\pi^3}} \,\mathcal{I}_{9/4}^{\text{asy}} \,\rho_i^{\text{kd}} \left\{ \frac{\tilde{r}_{\text{kd}}}{\tilde{r}} \right\}^{9/4} \,, \tag{2.30}$$

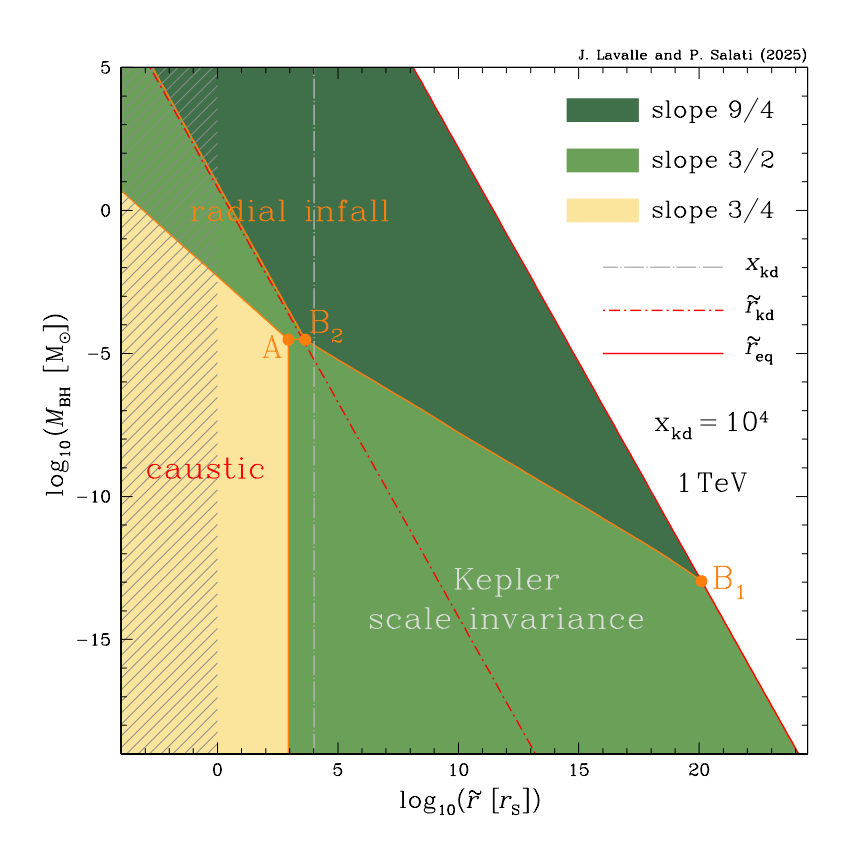


Figure 1. The post-collapse DM density follows a power law whose radial index depends on radius \tilde{r} and PBH mass $M_{\rm BH}$. The regions of prevalence for each particular index are plotted in this phase diagram with different colors. From the center of the DM halo to its outskirts, the slope is respectively equal to 3/4, 3/2 and, for heavy objects, 9/4. This phase diagram corresponds to a DM mass m_{χ} of 1 TeV and a thermal decoupling parameter $x_{\rm kd}$ of 10⁴. The shaded gray vertical band lies below the Schwarzschild radius.

where the dependence on PBH mass m goes through \tilde{r}_{kd} . Relation (2.29) yields the transition radius

$$\tilde{r}_{\rm t} = \upsilon \, \tilde{r}_{\rm kd} \quad \text{where} \quad \upsilon = \left\{ \frac{\mathcal{I}_{9/4}^{\rm asy}}{\mathcal{I}_{3/2}^{\rm asy}} \right\}^{4/3} \simeq 1.273 \,.$$
(2.31)

In appendix A.3, we go a step further and take into account the dependence of g_{eff} and h_{eff} with plasma temperature. We show that the coefficient v has to be replaced by the new value v' which depends now on kinetic decoupling temperature T_{kd} . We show that v' lies between 1 and v. The radius of transition \tilde{r}_{t} between the radial infall asymptotic regimes can be more correctly expressed as

$$\tilde{r}_{\rm t}(m) = v' \, \tilde{r}_{\rm kd} = v' \, \tilde{r}_{\rm kd}^0 \, m^{-2/3} \,.$$
 (2.32)

It is very convenient to tabulate once and for all the coefficient v' as a function of $T_{\rm kd}$. In the case of Fig. 1, where $T_{\rm kd}$ is equal to 100 MeV, we find $v' \simeq 1.261$, very close to v.

At the triple point B_2 of the phase diagram, the radial infall regimes with slope 3/2 and 9/4, as well as the Keplerian regime, have same asymptotic post-collapse DM densities

$$\rho_{3/2}(\tilde{r}_{\rm B_2}) = \rho'_{3/2}(\tilde{r}_{\rm B_2}, m_{\rm B_2}) = \rho_{9/4}(\tilde{r}_{\rm B_2}, m_{\rm B_2}). \tag{2.33}$$

The first identity yields the mass $M_{\rm B_2} = M_{\rm A} \equiv M_2$. In the configuration of Fig. 1, we already found a value of $3.03 \times 10^{-5} \rm \ M_{\odot}$ for M_2 . The last identity in Eq. (2.33) yields the radius

$$\tilde{r}_{\rm B_2} = v' \, \tilde{r}_{\rm kd}^0 \, m_2^{-2/3} \,. \tag{2.34}$$

Numerically, we find a ratio $\tilde{r}_{\rm B_2}/x_{\rm kd}$ of 0.444. In the phase diagram, the frontier between the asymptotic regimes with slopes 3/2 (Keplerian and radial infall) is represented by the orange horizontal segment connecting points A and B₂.

• Critical mass M_1 and point B_1

The transition between the Keplerian regime with slope 3/2 and the radial infall regime with slope 9/4 corresponds to the condition

$$\rho_{3/2}(\tilde{r}_{t}) = \rho_{9/4}(\tilde{r}_{t}, m). \tag{2.35}$$

As discussed above, the Keplerian regime exists only for PBH masses smaller than M_2 . Using the exact expression for the cosmological DM density is mandatory, but time consuming. We present in appendix A.4 a method allowing for a fast and accurate derivation of the radius of transition $\tilde{r}_{\rm t}$ for any values of the DM parameters m_{χ} and $T_{\rm kd}$, and for any given PBH mass $m = M_{\rm BH}/{\rm M}_{\odot}$.

Using expressions (2.10) and (2.13) for the asymptotic densities, as well as relation (A.5) for the cosmological DM density ρ_i^t at the cosmological time t_t and plasma temperature T_t for which the radius of influence of the PBH is precisely equal to \tilde{r}_t , the condition fulfilled by the radius of transition can be straightforwardly written as

$$\frac{\tilde{r}_{\rm t}}{\tilde{r}_{\rm eq}} = \Lambda \left\{ \frac{g_{\rm eff}(T_{\rm eq})}{g_{\rm eff}(T_{\rm t})} \right\} \left\{ \frac{h_{\rm eff}(T_{\rm t})}{h_{\rm eff}(T_{\rm eq})} \right\}^{4/3} \text{ where } \Lambda = (m_1/m)^{4/3} . \tag{2.36}$$

In the previous expression, m denotes the PBH mass while the benchmark value m_1 may be defined as

$$m_1 = \left\{ \frac{\mathcal{I}_{9/4}^{\text{asy}}}{\mathcal{I}_{3/2}^{\text{asy}}} \right\} \left\{ \frac{\tilde{r}_{\text{eq}}^0}{x_{\text{kd}}} \right\}^{3/2} \left\{ \frac{a_{\text{kd}}}{a_{\text{eq}}} \right\}^3.$$
 (2.37)

The mass m_1 depends only on the DM parameters through $x_{\rm kd}$ and $a_{\rm kd}$. The ratio of the cosmological DM densities $\rho_i^{\rm eq}$ (at matter-radiation equality) and $\rho_i^{\rm kd}$ (at kinetic decoupling) appears naturally in the derivation of m_1 . We have replaced it by the ratio of the corresponding scale factors $a_{\rm eq}$ and $a_{\rm kd}$ insofar as $\rho_i^{\rm eq}/\rho_i^{\rm kd}=a_{\rm kd}^3/a_{\rm eq}^3<1$. This allows for a more intuitive interpretation of m_1 . At this stage, several remarks are in order.

A minispike extends up to the radius of influence \tilde{r}_{eq} of its PBH taken at matterradiation equality. In expression (2.36), the radius \tilde{r}_{t} , at which the slope of the post-collapse radial profile transitions from 3/2 (Keplerian) to 9/4 (radial infall), cannot exceed that outer boundary. Since the reference temperature T_{t} is by construction larger than T_{eq} , the scaling with degrees of freedom goes approximately like

$$\left\{ \frac{g_{\text{eff}}(T_{\text{eq}})}{g_{\text{eff}}(T_{\text{t}})} \right\} \left\{ \frac{h_{\text{eff}}(T_{\text{t}})}{h_{\text{eff}}(T_{\text{eq}})} \right\}^{4/3} \simeq \left\{ \frac{h_{\text{eff}}(T_{\text{t}})}{h_{\text{eff}}(T_{\text{eq}})} \right\}^{1/3} \ge 1.$$
(2.38)

Therefore, only values of $\Lambda \leq 1$ yield acceptable physical solutions respecting $\tilde{r}_{\rm t} \leq \tilde{r}_{\rm eq}$, i.e. contained within the spike. As a consequence, the transition toward the radial infall

regime with slope 9/4 occurs only if the PBH mass m is larger than m_1 . For smaller masses, this asymptotic regime never appears. We are therefore led to identify m_1 , as defined in Eq. (2.37), with the critical mass M_1 discussed in section 2.1, setting $m_1 \equiv M_1/\mathrm{M}_{\odot}$. In the case of Fig. 1, we find a mass M_1 of $1.097 \times 10^{-13} \mathrm{M}_{\odot}$.

At the critical mass M_1 , the coefficient Λ is equal to 1. Relation (2.36) yields a transition at the minispike boundary with

$$\tilde{r}_{t}(m_{1}) = \tilde{r}_{eq}(m_{1}) = \tilde{r}_{eq}^{0} m_{1}^{-2/3}.$$
 (2.39)

The radius $\tilde{r}_{\rm t}(m_1) \equiv \tilde{r}_{\rm B_1}$ and mass $m_1 \equiv m_{\rm B_1}$ define the coordinates of B₁ in the phase diagram. This point lies on the line of the outer boundary $\tilde{r}_{\rm eq}$. Since the curve connecting B₁ to B₂ in Fig. 1 indicates the frontier between the Keplerian and radial infall regimes, we could have also derived the coordinates of B₁ by requiring that condition (2.35) is fulfilled at the minispike boundary $\tilde{r}_{\rm eq}$. This would have led to the same critical mass

$$m_1 = \left\{ \frac{\mathcal{I}_{9/4}^{\text{asy}}}{\mathcal{I}_{3/2}^{\text{asy}}} \right\} \left\{ \frac{\rho_i^{\text{eq}}}{\rho_i^{\text{kd}}} \right\} \left\{ \frac{\tilde{r}_{\text{eq}}^0}{x_{\text{kd}}} \right\}^{3/2}.$$
 (2.40)

Finally, although the mass m_1 has been derived essentially from graphical considerations pertaining to the phase diagram, it closely corresponds to the physical prescription given in section 2.1. As showed in [26], the kinetic-to-potential energy ratio of DM particles injected after kinetic decoupling, and hence beyond $\tilde{r}_{\rm kd}$, is a decreasing function of injection radius \tilde{r}_i where

$$\frac{\overline{K_i}}{|U_i|} = 3\sigma_i^2 \tilde{r}_i \propto \frac{1}{\sqrt{\tilde{r}_i}}.$$
 (2.41)

This ratio reaches a minimal value of $3\sigma_{\rm eq}^2 \tilde{r}_{\rm eq}$ at matter-radiation equality. After kinetic decoupling, the DM dispersion velocity scales like the inverse of the scale factor. Relation (2.37) can be converted into

$$\sigma_{\text{eq}}^{2} \tilde{r}_{\text{eq}}(m_{1}) = \left\{ \frac{\mathcal{I}_{3/2}^{\text{asy}}}{\mathcal{I}_{g/4}^{\text{asy}}} \right\}^{2/3} \text{ where } \tilde{r}_{\text{eq}}(m_{1}) \equiv \tilde{r}_{\text{eq}}^{0} m_{1}^{-2/3} \text{ while } \frac{\sigma_{\text{eq}}}{\sigma_{\text{kd}}} \equiv \frac{a_{\text{kd}}}{a_{\text{eq}}}.$$
 (2.42)

At M_1 , the minimal value of the kinetic-to-potential energy ratio is precisely equal to

$$\frac{\overline{K_{\text{eq}}}}{|U_{\text{eq}}|} = 3\sigma_{\text{eq}}^2 \tilde{r}_{\text{eq}} \equiv 3 \left\{ \frac{\mathcal{I}_{3/2}^{\text{asy}}}{\mathcal{I}_{9/4}^{\text{asy}}} \right\}^{2/3} \simeq 0.936.$$
(2.43)

This value is universal and falls very close to 1, in agreement with our physical definition of M_1 . For that particular mass, the kinetic-to-potential energy ratio of WIMPs at injection is expected to be equal to 1 at the boundary of the minispike. It exceeds unity everywhere else. For PBHs lighter than M_1 , the DM average velocity $\bar{\beta}_i$ at injection is everywhere larger than the local escape speed¹.

Equipped with all these notations, we have drawn in Fig. 1 the phase diagram for a 1 TeV DM particle whose kinetic decoupling parameter x_{kd} is equal to 10^4 . Kinetic decoupling

¹This is strictly true for radii larger than $\tilde{r}_{\rm kd}$ as well as for a large portion of the sphere of influence at kinetic decoupling. There is nevertheless an inessential region very close to the PBH where the potential energy always dominates over kinetic energy.

occurs at a temperature $T_{\rm kd}$ of 100 MeV. The construction starts by drawing in the $(\tilde{r}, M_{\rm BH})$ plane the radius of influence $\tilde{r}_{\rm eq}$ at matter-radiation equality as a function of PBH mass. We get the solid red line which represents the surface of DM minispikes as well as the boundary of the phase diagram. The radius of influence $\tilde{r}_{\rm kd}$ at kinetic decoupling is represented by the dotted short-dashed red line. For both lines, \tilde{r} varies as $m^{-2/3}$ with $m = M_{\rm BH}/{\rm M}_{\odot}$.

The next step is to draw the dotted long-dashed gray vertical line along which \tilde{r} is set equal to the kinetic decoupling parameter $x_{\rm kd}$. The intersection of that vertical line with the $\tilde{r}_{\rm kd}$ line falls always near the critical points A and B₂. According to relation (2.23), the radius of influence $\tilde{r}_{\rm kd}(m_2)$ at the critical mass $m_2 \equiv M_2/{\rm M}_{\odot}$ is roughly equal to $x_{\rm kd}/3$. A and B₂ are located along the same horizontal line at PBH mass M_2 . Both points are very close to the $x_{\rm kd}$ and $\tilde{r}_{\rm kd}$ lines. We actually showed above that

$$\frac{\tilde{r}_{\rm A}}{x_{\rm kd}} \simeq 0.0881$$
 while $\frac{\tilde{r}_{\rm A}}{\tilde{r}_{\rm kd}(m_2)} \simeq 0.250$. (2.44)

These ratios are universal and do not depend on WIMP parameters. The radius at B₂ fulfills similar relations with

$$\frac{\tilde{r}_{\rm B_2}}{\tilde{r}_{\rm kd}(m_2)} = v' \simeq 1.261 \quad \text{implying that} \quad \frac{\tilde{r}_{\rm B_2}}{x_{\rm kd}} \simeq 0.444 \,. \tag{2.45}$$

The parameter v' depends now on kinetic decoupling temperature $T_{\rm kd}$ but is always bounded by 1 and v = 1.273.

The critical point B_1 lies on the \tilde{r}_{eq} solid red line. The frontier between the Keplerian region with slope 3/2 (light-green) and the radial infall domain with slope 9/4 (dark-green) extends below M_2 . The radius \tilde{r}_t at which the transition occurs is the solution of Eq. (2.36). Neglecting the variations of the thermodynamical coefficients g_{eff} and h_{eff} , we find that \tilde{r}_t is proportional to $\tilde{r}_{eq}\Lambda \propto m^{-2}$, hence the straight line connecting B_2 to B_1 in Fig. 1. A closer inspection would reveal tiny wiggles insofar as g_{eff} and h_{eff} do vary with temperature during the radiation era.

The various asymptotic regions with their partition lines can be readily inferred from the prescriptions worked out in this section. The light-brown, light-green and dark-green areas correspond respectively to slopes 3/4, 3/2 and 9/4. The domain with slope 3/2 can be split into a radial infall part above M_2 and the Keplerian zone below.

To get a deeper insight in the structure of DM minispikes, we have explored in Fig. 2 how the density profiles change with PBH mass. With same DM parameters as before, we have first selected the critical values M_1 (dotted short-dashed blue) and M_2 (solid orange). These delineate three mass ranges. We have then chosen a value inside each of these intervals and considered the masses 10^{-17} M_{\odot} (solid purple), 10^{-9} M_{\odot} (long-dashed cyan) and 0.1 M_{\odot} (dotted short-dashed red). Each of the density profiles plotted in the right panel correspond to a particular horizontal line in the phase diagram of the left panel. A few remarkable points, including the critical points A, B₂ and B₁, are also plotted in both panels for pedagogical purposes and are discussed hereafter.

Like on a hiking map, the thin gray lines of the phase diagram are iso-density contours. In the caustic (light-brown) and Keplerian (light-green) regions, the lines are vertical insofar as the DM profile is universal once the post-collapse density is expressed as a function of the reduced radius \tilde{r} . All the profiles that we have considered lie at some point along the same curve which connects points C, A and G. This behavior occurs as long as the corresponding

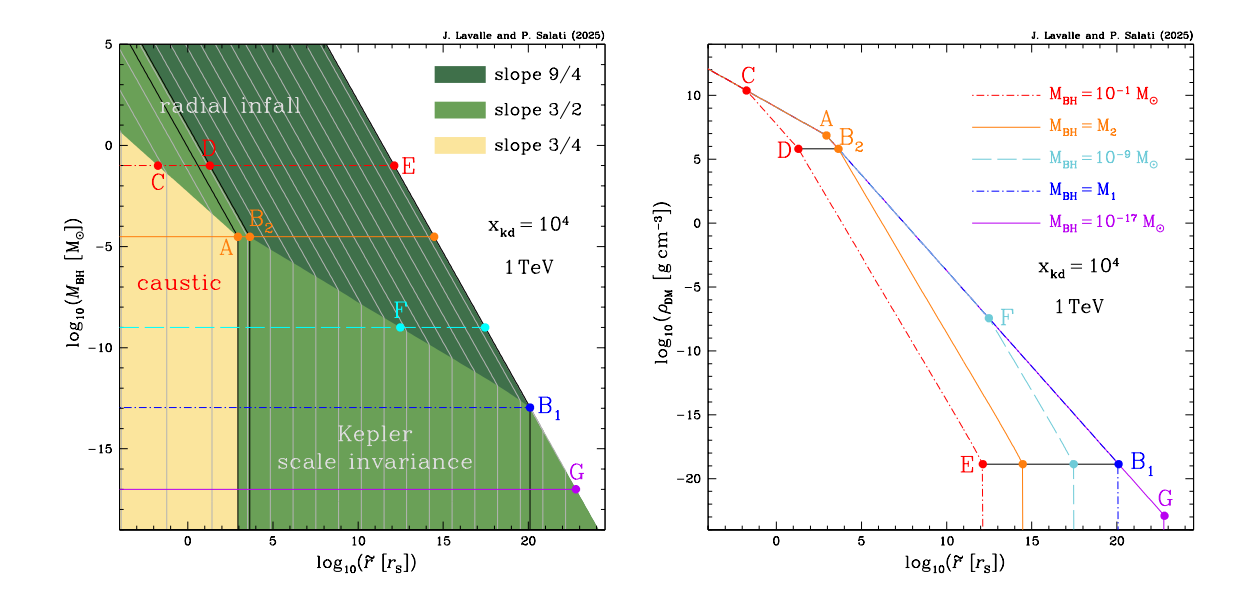


Figure 2. In the left panel, the phase diagram of Fig. 1 has been reproduced. Each thin gray line corresponds to a specific value of the post-collapse DM density which, from left to right, has been varied from 10^{12} down to 10^{-22} g cm⁻³ by decrements of 10^2 . The critical points A, B₂ and B₁ lie along the solid black iso-density lines where the DM density is respectively equal to 7.28×10^6 , 6.44×10^5 and 1.36×10^{-19} g cm⁻³. In the **right panel**, the DM density profiles have been plotted versus reduced radius \tilde{r} for different values of the PBH mass. These are coded with color and line type as indicated. Each profile of the right panel corresponds to a particular horizontal line in the left panel. A few remarkable points are also featured in both panels and discussed in the text.

horizontal slices in the phase diagram cross the caustic and Keplerian regions. When they enter the radial infall domains, profiles depart from the universal curve. In these regions, the iso-density lines are leaning leftward with $\tilde{r} \propto m^{-2/3}$.

The prototypical examples featured in Fig. 2 nicely summarize the rich dynamics of DM minispikes presented at the end of section 2.1. Below M_1 , the density profile is always universal. As \tilde{r} increases, the slope is 3/4 and switches to 3/2 at point A. It stays constant until the surface is reached at $\tilde{r}_{\rm eq}$, i.e. at point G in the case of the $10^{-17}~{\rm M}_{\odot}$ PBH of the solid purple curve. Increasing that mass would make G closer to B₁.

Between M_1 and M_2 , the density profile departs from the universal behavior when the radial infall regime with slope 9/4 sets in. This occurs at point F in the case of the 10^{-9} M_{\odot} PBH of the long-dashed cyan curve. In the left panel of Fig. 2, F sits at the border between the Keplerian (light-green) and radial infall (dark-green) domains. In the right panel, the profile leaves the universal curve at F and falls steeply with slope 9/4. Varying the PBH mass from M_1 to M_2 would make point F move from B₁ up to B₂. This two extreme situations are respectively featured by the dotted short-dashed blue and the solid orange curves.

The dotted short-dashed red curve highlights the case of the heaviest PBHs. As is clear in the left panel of Fig. 2, the frontier between the caustic (light-brown) and radial infall (light-green) regions is no longer vertical above M_2 . In our example, the transition between these asymptotic regimes occurs at point C^2 where the slope increases from 3/4 to 3/2. A

 $^{^2}$ In the plot, point C lies in the unphysical region below the Schwarzschild radius. Should we have taken a lighter PBH, with mass 10^{-3} M_☉ for instance, the transition from 3/4 to 3/2 would have turned physical.

new transition occurs at point D between the two radial infall regimes and the slope jumps from 3/2 to 9/4. Point E corresponds to the surface of the minispike. Varying the PBH mass from M_2 upward would make point C slip away from A along the universal curve and would shift the entire profile to the left.

2.3 Numerical vs approximate semi-analytical results

The aim of this work is to construct an acceptable semi-analytical approximation for the DM density inside minispikes. The calculation should be fast and yield a value close to the result of the lengthy numerical integration (2.4). To accelerate the code, a few tables can be pre-calculated as explained in appendix A, together with the thermodynamical coefficients g_{eff} and h_{eff} .

The post-collapse DM density ρ depends on reduced radius \tilde{r} , PBH mass $M_{\rm BH}$ and DM parameters. The WIMP mass m_{χ} and decoupling parameter $x_{\rm kd}$ need first to be specified. This allows to derive the properties of the phase diagram, i.e. the critical masses M_1 and M_2 as well as the coordinates in the $(\tilde{r}, M_{\rm BH})$ plane of the particular points A, B₁ and B₂. Expressions for these quantities have been thoroughly discussed in section 2.2.

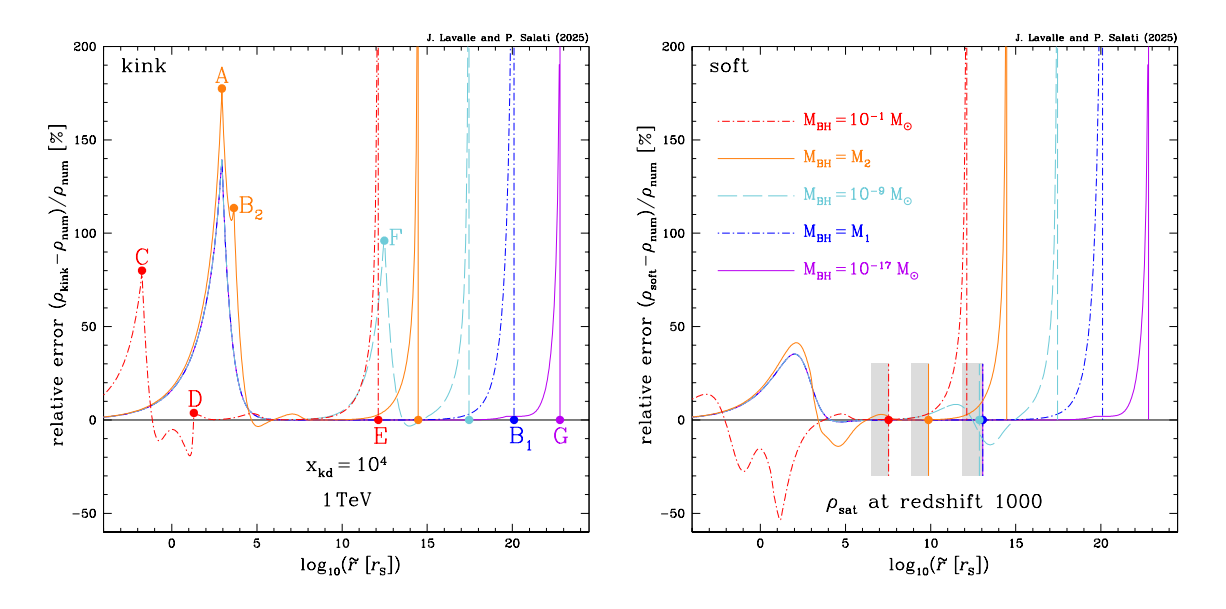


Figure 3. The relative difference between the approximate post-collapse DM density and the exact numerical result is featured as a function of reduced radius \tilde{r} . The DM parameters are the same as for the previous figures. We have also considered the same PBH masses as in Fig. 2 with the same code for colors and line type. The **left panel** is devoted to the kink approximation. The sharp peaks which the curves exhibit correspond to changes in the asymptotic regime occuring at the very same points A, B₂, C, D and F as in Fig. 2. The soft approximation is featured in the **right panel**. For each PBH mass, the colored vertical edges of the light-gray bands and their associated points indicate the radii below which the post-collapse DM density is larger than the saturation density ρ_{sat} taken at a redshift z of 10^3 for a thermal DM annihilation cross-section. To the left of these edges, the DM distribution has been erased by annihilation and the profiles have been flattened.

As a first approximation, dubbed kink, we simply use the asymptotic expressions in their respective domains of prevalence. The code determines the PBH mass regime by comparing $M_{\rm BH}$ to M_1 and M_2 . The prescription is as follows.

- If $M_{\rm BH} \leq M_1$, the density is given by relation (2.8) below $\tilde{r}_{\rm A}$, and by (2.10) above.
- If the PBH mass lies between M_1 and M_2 , the same algorithm can be used. Furthermore, somewhere between $\tilde{r}_{\rm B_2}$ and $\tilde{r}_{\rm eq}$, the profile enters the radial infall regime with slope 9/4. A fast derivation of the radius at which this transition occurs is presented in appendix A.4. The post-collapse density ρ is then given by the asymptotic expression (2.13), which makes use of the cosmological DM density ρ_i . The latter can be fastly derived as explained in appendix A.1.
- For the heaviest PBHs, i.e. above M_2 , three asymptotic regimes come successively into play as \tilde{r} increases. The transition radius between the caustic (slope 3/4) and radial infall (slope 3/2) regions is now given by Eq. (2.28). In this intermediate region, the density fulfills Eq. (2.12). Close to $\tilde{r}_{\rm kd}$, the radial infall regime changes as the slope switches from 3/2 to 9/4. Relation (2.32) yields the exact location of the transition. Beyond that point, we recover the asymptotic expression (2.13). As explained in appendix A.3, the coefficient v' can be rapidly calculated once $T_{\rm kd}$ is defined.

Using the asymptotic expressions makes the approximated density $\rho_{\rm kink}$ continuous, but not its derivative at the borders between domains of prevalence where $\rho_{\rm kink}$ presents sharp breaks by construction. In the left panel of Fig. 3, we have plotted the relative difference between the kink approximation and the result of the numerical integration (2.4), for the five profiles of Fig. 2. The code for color and line type is the same, as well as DM parameters. Notice that the vertical scale is linear and extends from -60% to +200%, while the radius \tilde{r} varies logarithmically over more than 28 decades.

As anticipated, the kink approximation overestimates the numerical result at the transition points. The curves exhibit sharp peaks precisely at the same points A, B₂, C, D and F as in Fig. 2 where the asymptotic regime changes and the density profile softens. The relative error is significant. It reaches 80% at C for a 0.1 $\rm M_{\odot}$ PBH. It exceeds 100% at A whatever the PBH mass. The two peaks of the solid orange curve at A and B₂ are noticeable. The peak at F corresponds to the onset of the radial infall regime in the intermediate case of a $\rm 10^{-9}~M_{\odot}~PBH$.

To suppress the peaks and obtain a DM density closer to the numerical result, we have considered a new approximation, dubbed soft. Once the PBH mass is defined, the various asymptotic regimes a are identified with their respective densities $\rho_{\rm a}$. The density $\rho_{\rm soft}$ fulfills the definition

$$\frac{1}{\rho_{\text{soft}}} = \sum_{\text{regimes a}} \frac{1}{\rho_{\text{a}}}.$$
 (2.46)

The relative error associated to $\rho_{\rm soft}$ is presented in the right panel of Fig. 3. The peaks have disappeared and the agreement between approximation and numerical integration has improved. As showed by the long-dashed cyan curve, the peak at F has vanished. The errors at A and B₂ have considerably decreased and do not exceed 40% now. The dotted short-dashed red curve exhibits wiggles though, and indicates that $\rho_{\rm soft}$ undershoots the numerical result by a factor of 2 at a radius \tilde{r} of order 10.

The soft approximation yields very decent results at radii \tilde{r} below 10^{-2} . In this region, the caustic regime dominates. To check if the post-collapse DM density is well approximated by relation (2.8), the numerical integration (2.4) has been performed with injection radius \tilde{r}_i varying from 0 up to \tilde{r}_{eq} . According to the right panel of Fig. 3, the relative error in that

range is less than 15%. It might be worth emphasizing that for the particular values which we have selected for m_{χ} and $x_{\rm kd}$, the transition between the caustic (slope 3/4) and radial infall (slope 3/2) regimes occurs at unphysical radii for PBHs heavier than 0.01 ${\rm M}_{\odot}$, but can move to larger radii for larger values of $x_{\rm kd}$.

An actual calculation should nevertheless take into account the existence of a horizon around each PBH. The numerical integration of relation (2.4) must be performed from an injection radius \tilde{r}_i of at least 1. We expect our approximations to break down at low radii. This might be a problem insofar as the annihilation rates $\Gamma_{\rm BH}$ of minispikes, which we are aiming at in this work, depend sensitively on the DM density at small radii where it is the largest.

We are rescued by the ongoing DM annihilations taking place inside minispikes as the universe expands. The DM density is erased and cannot exceed the so-called saturation value $\rho_{\rm sat}$ defined in section 3.1. The limits on PBHs and DM species which are discussed in section 4 are based on observations of the post-recombination universe. At the epochs under scrutiny, annihilation has considerably erased the post-collapse DM profiles. Our approximations are to be used in the outer parts of minispikes, where the DM density is less than $\rho_{\rm sat}$. At a redshift z of 10^3 for instance, a thermal DM annihilation cross-section of 3×10^{-26} cm³ s⁻¹ translates into the saturation density

$$\rho_{\text{sat}} = 4.97 \times 10^{-9} \text{ g cm}^{-3}$$
. (2.47)

In the right panel of Fig. 3, the colored vertical edges of the light-gray bands indicate, for each PBH mass, the saturation radius $\tilde{r}_{\rm sat}$ below which the minispike density has been erased down to $\rho_{\rm sat}$. A precise determination of the post-collapse DM density is therefore of no use below $\tilde{r}_{\rm sat}$ whereas it is mandatory above it. In this external region, the error is always small, except close to the surface at $\tilde{r}_{\rm eq}$.

In both panels, the relative error diverges actually at the outer boundaries of minispikes. Both approximations yield there a non-vanishing result while the numerical integration returns a much smaller value, sometimes set to 0 by brute force. We expect the relative error to explode at $\tilde{r}_{\rm eq}$, hence the spikes which both panels display. Although spectacular, these divergences are harmless in most cases. Close to the surface, the DM density is so small that it does not contribute significantly to $\Gamma_{\rm BH}$ in general. A detailed inspection of the right panel shows nevertheless that the dotted short-dashed blue spike at M_1 is particularly thick compared to the others. This point will be clarified at the end of section 3.3 where the annihilation rates calculated with the numerical integral (2.4) and the soft approximation (2.46) are compared.

3 Annihilation rate of the dark matter minispikes

DM minispikes around PBHs have kept the memory of how dense the universe was during the radiation era, especially at kinetic decoupling. DM species inside these structures are highly packed, and if made of self-annihilating particles, are subject to strong annihilation. The rate of annihilation of a PBH minispike is the integral over its volume of the local DM annihilation rate

$$\Gamma_{\rm BH} = \int d^3 \mathbf{r} \left\{ \frac{1}{2} \langle \sigma_{\rm ann} v \rangle n^2 \right\} (\mathbf{r}).$$
(3.1)

The integral runs over the sphere of influence at matter-radiation equality while the domain located below the horizon does not contribute. Here we assume that all of non-PBH DM is

made of self-annihilating Majorana fermions, hence the factor 1/2. In this article, we only deal with s-wave annihilation, whose thermally averaged cross-section $\langle \sigma_{\rm ann} v \rangle$ does not depend on DM velocity. As this quantity is constant throughout the minispike, it can be factored out of integral (3.1). The DM number density $n = \rho/m_{\chi}$ does depend on position \mathbf{r} through the density profile $\rho(\tilde{r})$ and WIMP mass m_{χ} . Under these conditions, the annihilation rate simplifies into the spherical integral

$$\Gamma_{\rm BH} = \frac{1}{2} \langle \sigma_{\rm ann} v \rangle \, r_{\rm S}^3 \int_{\tilde{r}_{\rm min}}^{\tilde{r}_{\rm max}} 4\pi \tilde{r}^2 \mathrm{d}\tilde{r} \left\{ \frac{\rho(\tilde{r})}{m_{\chi}} \right\}, \tag{3.2}$$

where $r_{\rm S}$ is the PBH Schwarzschild radius. The integral runs from $\tilde{r}_{\rm min} \sim 1$ up to $\tilde{r}_{\rm max} \equiv \tilde{r}_{\rm eq}$.

Because of annihilations, the density profile $\rho(\tilde{r})$ departs from the distribution resulting from the sole collapse of DM onto PBHs. The latter has been calculated by many authors [25– 27, 31, and section 2 is devoted to the presentation of a tractable approximation. But as soon as DM self-annihilates inside minispikes, the density profiles of these structures are eroded and their densest regions can be significantly depleted. The actual process is complicated to model and should, in principle, be included in the overall dynamical evolution of the spike and regulate the high density accumulated during the radiation era. This formally leads to a non-linear equation, as we shortly discuss below. Particles that were initially injected on a given trajectory annihilate as they move across the innermost regions. The larger the density, the stronger the annihilation. We expect their population to be depleted as time goes on. The contribution of each elliptical orbit to the overall DM distribution decreases, and so does the DM density. This leads in turn to a non-trivial variation of the rate of annihilation. To summarize, the DM density and its rate of destuction are entangled through a complex interplay between all orbits. Note also that the annihilation of DM starts in principle as soon as minispikes form at kinetic decoupling. A complete treatment of this destruction mechanism is beyond the scope of this paper. It requires a dedicated analysis taking into account the specificities of DM collapse onto PBHs during the radiation era. We note that the existence of an annihilation plateau has been discussed in [28, 29], although in a quite different context.

3.1 Saturation density and truncation in the phase diagram

An annihilation plateau has been so far considered in most publications as a reasonable proxy for the inner density profile of DM clumps undergoing annihilation after their formation. The underlying assumption is that DM particles move along a direction that is perpendicular to the gradient of their density. If so, we can identify the partial and total time derivatives of the DM density and write

$$\frac{\mathrm{d}\rho}{\mathrm{d}t} = \frac{\partial\rho}{\partial t} + \mathbf{v} \cdot \nabla\rho \equiv \frac{\partial\rho}{\partial t} \quad \text{insofar as} \quad \mathbf{v} \perp \nabla\rho.$$
 (3.3)

The DM density ρ decreases as a result of WIMP annihilations and evolves according to

$$\frac{\mathrm{d}\rho}{\mathrm{d}t} = m_{\chi} \frac{\mathrm{d}n}{\mathrm{d}t} = -2 \times \left\{ \frac{1}{2} \langle \sigma_{\mathrm{ann}} v \rangle n^2 \right\} \times m_{\chi} \quad \text{with} \quad \rho = n m_{\chi}. \tag{3.4}$$

Two particles are destroyed in a single annihilation, hence the extra factor of 2 in the previous equality. Assuming spherical symmetry while combining expressions (3.3) and (3.4) yields

$$\frac{\partial}{\partial t} \left\{ \rho(t, \tilde{r}) \right\} = -\frac{\langle \sigma_{\text{ann}} v \rangle}{m_{\chi}} \left\{ \rho(t, \tilde{r}) \right\}^{2}, \qquad (3.5)$$

where $\tilde{r} \equiv r/r_{\rm S}$ is the reduced radius. This equation is strictly correct if WIMPs move along circular orbits. Its straightforward solution can be written as

$$\frac{1}{\rho(t_2, \tilde{r})} = \frac{1}{\rho(t_1, \tilde{r})} + \int_{t_1}^{t_2} \frac{\langle \sigma_{\text{ann}} v \rangle}{m_{\chi}} dt.$$
 (3.6)

In the case of s-wave annihilation, the average cross-section $\langle \sigma_{\rm ann} v \rangle$ is a constant independent of WIMP velocity and we get

$$\frac{1}{\rho(t_2, \tilde{r})} = \frac{1}{\rho(t_1, \tilde{r})} + \frac{1}{\rho_{\text{sat}}}.$$
 (3.7)

The so-called saturation density appears, that is defined as

$$\rho_{\text{sat}} = \frac{m_{\chi}}{\langle \sigma_{\text{ann}} v \rangle \Delta t} \quad \text{where} \quad \Delta t = t_2 - t_1.$$
 (3.8)

We will herefater identify time t_1 with the age $t_{\rm eq}$ of the universe at the end of the radiation era, when minispikes have completely formed. Time t_2 is the epoch of the physical process under scrutiny in section 4, i.e. the injection of energy in the post-recombination plasma, or the recent extragalactic emission of gamma-rays. We will therefore identify $\rho(t_1, \tilde{r})$ with the post-collapse density profile without DM annihilation $\rho(\tilde{r})$ as derived by [25–27, 31]. This initial profile is eroded by annihilations to become, at time $t > t_{\rm eq}$, equal to

$$\rho(t,\tilde{r}) = \frac{\rho_{\text{sat}} \,\rho(\tilde{r})}{\rho_{\text{sat}} + \rho(\tilde{r})} \simeq \begin{cases} \rho_{\text{sat}} & \text{if } \rho(\tilde{r}) \gg \rho_{\text{sat}},\\ \rho(\tilde{r}) & \text{if } \rho(\tilde{r}) \ll \rho_{\text{sat}}. \end{cases}$$
(3.9)

The transition between these regimes occurs at the saturation radius $\tilde{r}_{\rm sat}$ where both densities $\rho(\tilde{r})$ and $\rho_{\rm sat}$ are equal. The inner regions of minispikes are erased and replaced by a plateau with density $\rho_{\rm sat}$ extending to $\tilde{r}_{\rm sat}$ as showed in the left panel of Fig. 4. The impact on the phase diagram of the DM annihilations taking place between matter-radiation equality and a redshift z of 10^3 is featured for the same WIMP parameters as in Fig. 2. In the dark-gray region extending to the left of the solid black iso-density line that crosses points T and H, the DM density has be flattened to its saturation value $\rho_{\rm sat}$ of 4.97×10^{-9} g cm⁻³. The effect is even more dramatic in the right panel. The post-collapse universal profile, which corresponds to the dotted long-dashed dark-gray curve, is now replaced by a horizontal segment featuring the saturation plateau. For radii larger than $\tilde{r}_{\rm sat}$, the post-collapse DM profiles are not modified, as a quick inspection of the differences between Figs. 2 and 4 would show.

In table 1, the saturation density has been calculated for two values of the redshift and for several DM parameters covering a large spectrum of possibilities. The annihilation cross-section has been set equal to its benchmark value of 3×10^{-26} cm³ s⁻¹. We remark that $\rho_{\rm sat}$ is always bounded by the post-collapse DM densities $\rho_{\rm B_1}$ and $\rho_{\rm B_2}$ at critical points B₁ and B₂ of the phase diagram. This allows to derive a simple approximation for the annihilation rate $\Gamma_{\rm BH}$ in the next section. The last line of the table corresponds to the plots of Fig. 4.

3.2 Behavior of the annihilation rate

The saturation density ρ_{sat} enters in the definition of the annihilation rate (3.2) of minispikes which we modify into

$$\Gamma_{\rm BH} = \frac{1}{2} \langle \sigma_{\rm ann} v \rangle \left\{ \frac{\rho_{\rm sat}}{m_{\chi}} \right\}^2 r_{\rm S}^3 \, \mathcal{J}_{\rm BH} \quad \text{where} \quad \mathcal{J}_{\rm BH} \equiv \int_{\tilde{r}_{\rm min}}^{\tilde{r}_{\rm eq}} 4\pi \tilde{r}^2 \mathrm{d}\tilde{r} \left\{ \frac{\rho(\tilde{r})}{\rho_{\rm sat}} \right\}^2. \tag{3.10}$$

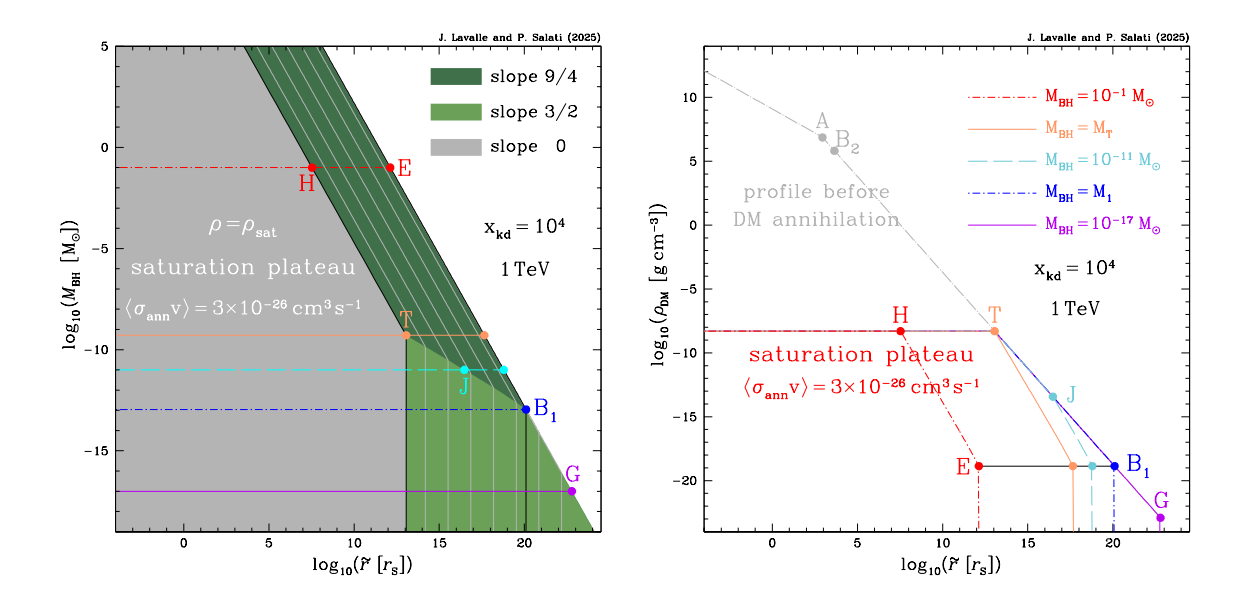


Figure 4. Same panels as in Fig. 2 where DM annihilation is now included. In the left panel, the inner region of the phase diagram is replaced by a saturation plateau where the DM density is equal to the constant ρ_{sat} . For a redshift z of 10^3 and a thermal DM annihilation cross-section, we find a value of $4.97 \times 10^{-9} \text{ g cm}^{-3}$. The solid black iso-density line that runs through points T and H corresponds to ρ_{sat} , and features the border \tilde{r}_{sat} of the saturation plateau. The critical point B₁ lies along the solid black iso-density line where the DM density is equal to $1.36 \times 10^{-19} \text{ g cm}^{-3}$. In the right panel, the DM density profiles have been plotted versus reduced radius \tilde{r} for different values of PBH mass. These are coded with color and line type as indicated. Each profile of the right panel corresponds to a particular horizontal line in the left panel. DM annihilation has erased the post-collapse profiles and flattened them into the saturation plateau A few remarkable points are also featured in both panels and discussed in the text.

x_{kd}	m_{χ}	$ ho_{ m B_1}$	$ \rho_{\rm sat} \text{ at } z = 0 $	$\rho_{\rm sat}$ at $z = 1000$	$ ho_{ m B_2}$
10^{2}	1 MeV	1.355×10^{-19}	1.363×10^{-19}	4.974×10^{-15}	1.543×10^{-7}
10^{2}	1 GeV	1.355×10^{-19}	1.363×10^{-16}	4.974×10^{-12}	4.223×10^{2}
10^{2}	1 TeV	1.355×10^{-19}	1.363×10^{-13}	4.974×10^{-9}	3.385×10^{12}
10^{4}	1 MeV	1.355×10^{-19}	1.363×10^{-19}	4.974×10^{-15}	1.547×10^{-13}
10^{4}	1 GeV	1.355×10^{-19}	1.363×10^{-16}	4.974×10^{-12}	1.917×10^{-4}
10^{4}	1 TeV	1.355×10^{-19}	1.363×10^{-13}	4.974×10^{-9}	6.439×10^5

Table 1. The saturation density $\rho_{\rm sat}$ taken at two different redshifts is compared to the post-collapse DM densities at points B₁ and B₂ of the phase diagram $(\tilde{r}, M_{\rm BH})$ (see Fig. 1) for different kinetic decoupling parameters $x_{\rm kd}$ and DM masses m_{χ} . Densities are expressed in g cm⁻³. The annihilation cross-section $\langle \sigma_{\rm ann} v \rangle$ has been set equal to its thermal value of 3×10^{-26} cm³ s⁻¹. The saturation densities in which we are interested in section 4 are always bounded by $\rho_{\rm B_1}$ and $\rho_{\rm B_2}$.

The radial integral $\mathcal{J}_{\rm BH}$ runs from the lower bound $\tilde{r}_{\rm min}$ up to the surface of the minispike at $\tilde{r}_{\rm eq}$. The latter radius depends on PBH mass as given in Eq. (2.15). The saturation density is defined by relation (3.8) in which $\Delta t = t_{\rm U}(z) - t_{\rm eq}$, with $t_{\rm eq}$ and $t_{\rm U}(z)$ respectively the age of the universe at matter-radiation equality and at redshift z. We defer to the next section the

numerical estimate of \mathcal{J}_{BH} using the soft approximation for the post-collapse DM density, and concentrate here on the derivation of a simplistic approximation which will prove to be very helpful to understand the observational bounds discussed in section 4.

To commence, we disregard the effect of the PBH horizon and set $\tilde{r}_{\rm min}$ equal to 0. In appendix B, we give more correct expressions where $\tilde{r}_{\rm min}$ is set to 1 since minispikes extend only outside the Schwarzschild radii of their central objects³. The correction turns out to be very small, except for super-heavy black holes. Then, as showed in table 1, the saturation density is in general bounded by $\rho_{\rm B_1}$ and $\rho_{\rm B_2}$, the densities at critical points B₁ and B₂ of the phase diagram. This is actually the case in the panels of Fig. 4 which we will use hereafter as a pedagogical example.

In the left panel, point T lies in the phase diagram at the intersection of the saturation plateau boundary (solid black line) with the frontier separating the Keplerian region with slope 3/2 (light-green) from the radial infall domain with slope 9/4 (dark-green). The coordinates of T in the $(\tilde{r}, M_{\rm BH})$ plane fulfill the conditions

$$\rho_{\rm sat} = \rho_{3/2}(\tilde{r}_{\rm T}) = \rho_{9/4}(\tilde{r}_{\rm T}, m_{\rm T}) \text{ where } m_{\rm T} \equiv M_{\rm T}/{\rm M}_{\odot}.$$
(3.11)

Once the saturation density $\rho_{\rm sat}$ has been derived, the first equality yields the reduced radius

$$\tilde{r}_{\rm T} = x_{\rm kd} \left\{ \frac{2^{1/3}}{\pi} \right\} \left\{ \mathcal{I}_{3/2}^{\rm asy} \, \frac{\rho_i^{\rm kd}}{\rho_{\rm sat}} \right\}^{2/3}.$$
 (3.12)

Deriving the mass $M_{\rm T}$ requires first to use Eq. (2.13) to get the cosmological DM density ρ_i corresponding to $\rho_{\rm sat}$. From the prescriptions of appendix A.2, it is straightforward to get the radius $\tilde{r}_{\rm T}^0$ of the sphere of influence of a 1 M $_{\odot}$ PBH at the exact moment t_i at which the cosmological DM density is equal to ρ_i . The mass $M_{\rm T}$ is given by

$$m_{\rm T} = \left(\tilde{r}_{\rm T}^0/\tilde{r}_{\rm T}\right)^{3/2} \,. \tag{3.13}$$

This mass $M_{\rm T}$ together with the critical mass $M_{\rm 1}$ delineate three regions which, in Fig. 4, are exemplified by the values 10^{-17} (solid purple), 10^{-11} (long-dashed cyan) and $0.1~{\rm M}_{\odot}$ (dotted short-dashed red) for $M_{\rm BH}$.

• $\rho_{\text{B}_1} \leq \rho_{\text{sat}} \leq \rho_{\text{B}_2}$ and $M_{\text{BH}} \leq M_1$

A close inspection of the solid purple curve shows that the density is flat up to \tilde{r}_T (saturation plateau) and decreases as a power law with slope 3/2 above. The radial integral \mathcal{J}_{BH} can be split into two parts

$$\mathcal{J}_{BH} = \int_0^{\tilde{r}_T} 4\pi \tilde{r}^2 d\tilde{r} + \int_{\tilde{r}_T}^{\tilde{r}_{eq}} 4\pi \tilde{r}^2 d\tilde{r} \left\{ \frac{\tilde{r}_T}{\tilde{r}} \right\}^3.$$
 (3.14)

This yields

$$\mathcal{J}_{\rm BH} = \frac{4}{3}\pi \,\tilde{r}_{\rm T}^3 \,\mathcal{K}_{\rm BH} \quad \text{with} \quad \mathcal{K}_{\rm BH} = 1 + 3\ln\left\{\frac{\tilde{r}_{\rm eq}}{\tilde{r}_{\rm T}}\right\}. \tag{3.15}$$

• $\rho_{\text{B}_1} \leq \rho_{\text{sat}} \leq \rho_{\text{B}_2}$ and $M_1 \leq M_{\text{BH}} \leq M_{\text{T}}$

This intermediate case corresponds to the long-dashed cyan curve. In the left panel of Fig. 4, point J lies on the demarcation line separating the Keplerian (slope 3/2) and radial infall

³Rigorously, relativistic corrections are expected close to the Schwarzschild radius of a PBH, a region where our calculation cannot be considered as reliable as elsewhere.

(slope 9/4) regions. The reduced radius \tilde{r}_J can be readily derived using the method described in section 2.2 and appendix A.4 based on the calculation of $\Lambda = (m_1/m)^{4/3}$. Three parts contribute now to \mathcal{J}_{BH} . The profile is flat up to \tilde{r}_T . It decreases with slope 3/2 between T and J. Above \tilde{r}_J and up to the surface at \tilde{r}_{eq} , the radial index is 9/4. The radial integral can be expressed as

$$\mathcal{J}_{BH} = \int_0^{\tilde{r}_T} 4\pi \tilde{r}^2 d\tilde{r} + \int_{\tilde{r}_T}^{\tilde{r}_J} 4\pi \tilde{r}^2 d\tilde{r} \left\{ \frac{\tilde{r}_T}{\tilde{r}} \right\}^3 + \int_{\tilde{r}_J}^{\tilde{r}_{eq}} 4\pi \tilde{r}^2 d\tilde{r} \left\{ \frac{\tilde{r}_T}{\tilde{r}_J} \right\}^3 \left\{ \frac{\tilde{r}_J}{\tilde{r}} \right\}^{9/2}, \tag{3.16}$$

which leads to

$$\mathcal{J}_{\rm BH} = \frac{4}{3}\pi\,\tilde{r}_{\rm T}^3\,\mathcal{K}_{\rm BH} \quad \text{where} \quad \mathcal{K}_{\rm BH} = 3 + 3\ln\left\{\frac{\tilde{r}_{\rm J}}{\tilde{r}_{\rm T}}\right\} - 2\left\{\frac{\tilde{r}_{\rm J}}{\tilde{r}_{\rm eq}}\right\}^{3/2}.\tag{3.17}$$

• $\rho_{\rm B_1} \leq \rho_{\rm sat} \leq \rho_{\rm B_2}$ and $M_{\rm T} \leq M_{\rm BH}$

The prototypical example of this configuration is featured by the dotted short-dashed red curve. The profile is flat up to the border of the saturation plateau at H, while it decrases above with slope 9/4 up to the surface at E. In the left panel, point H lies on the iso-density solid black line with density ρ_{sat} . The reduced radii at points H and T are related through

$$\tilde{r}_{\rm H}/\tilde{r}_{\rm T} \equiv (M_{\rm BH}/M_{\rm T})^{-2/3}$$
. (3.18)

Point E lies at the surface of the minispike at \tilde{r}_{eq} . Once the radii \tilde{r}_{H} and $\tilde{r}_{E} \equiv \tilde{r}_{eq}$ have been determined, the radial integral ensues

$$\mathcal{J}_{BH} = \int_0^{\tilde{r}_H} 4\pi \tilde{r}^2 d\tilde{r} + \int_{\tilde{r}_H}^{\tilde{r}_E} 4\pi \tilde{r}^2 d\tilde{r} \left\{ \frac{\tilde{r}_H}{\tilde{r}} \right\}^{9/2}.$$
 (3.19)

We can recast it into

$$\mathcal{J}_{\rm BH} = \frac{4}{3}\pi\,\tilde{r}_{\rm T}^3\,\mathcal{K}_{\rm BH} \quad \text{with} \quad \mathcal{K}_{\rm BH} = \left\{\frac{M_{\rm T}}{M_{\rm BH}}\right\}^2 \left\{3 - 2\left(\tilde{r}_{\rm H}/\tilde{r}_{\rm E}\right)^{3/2}\right\}.$$
 (3.20)

Increasing the PBH mass from M_1 to M_T makes point J shift from B_1 to T in the left panel of Fig. 4. In this regime, the integral \mathcal{K}_{BH} is defined by Eq. (3.17). Notice the continuity of this expression with the definitions (3.15) and (3.20) at the transition points B_1 and T.

Although the saturation density never exceeds the post-collapse density $\rho_{\rm B_2}$ in what follows, it may occasionally be smaller than $\rho_{\rm B_1}$. As showed in table 1, $\rho_{\rm sat}$ is close to $\rho_{\rm B_1}$ for a 1 MeV DM species. Increasing the annihilation cross-section $\langle \sigma_{\rm ann} v \rangle$ by a factor of 2 over its thermal value would make $\rho_{\rm sat}$ drop below $\rho_{\rm B_1}$. If so, two possibilities arise, depending on PBH mass. In this configuration, the saturation radius $\tilde{r}_{\rm T}$ is still defined by Eq. (3.12). We remark that now, at the transition mass $M_{\rm T}$, the radius of the minispike is precisely equal to $\tilde{r}_{\rm T}$. This translates into the definition

$$m_{\rm T} = \left(\tilde{r}_{\rm eq}^0/\tilde{r}_{\rm T}\right)^{3/2}$$
 where $m_{\rm T} \equiv M_{\rm T}/{\rm M}_{\odot}$. (3.21)

In the panels of Fig. 4, point T would lie between B₁ and G along the \tilde{r}_{eq} line, with M_T less than M_1 .

• $\rho_{\rm sat} \leq \rho_{\rm B_1}$ and $M_{\rm BH} \leq M_{\rm T}$

The saturation plateau extends up to $\tilde{r}_{\rm T}$ above which the density decreases with slope 3/2

until the surface is reached at \tilde{r}_{eq} . This case has already been examined. The radial integral \mathcal{J}_{BH} is given by Eq. (3.15). We can go a step further and take advantage of relations (2.15) and (3.21) to show that

$$\mathcal{J}_{\rm BH} = \frac{4}{3}\pi \,\tilde{r}_{\rm T}^3 \,\mathcal{K}_{\rm BH} \quad \text{with} \quad \mathcal{K}_{\rm BH} = 1 + 2\ln\left\{\frac{M_{\rm T}}{M_{\rm BH}}\right\}. \tag{3.22}$$

• $\rho_{\rm sat} \leq \rho_{\rm B_1}$ and $M_{\rm T} \leq M_{\rm BH}$

The minispike is homogeneous with density $\rho_{\rm sat}$. The radial integral $\mathcal{J}_{\rm BH}$ is readily given by

$$\mathcal{J}_{\rm BH} = \int_0^{\tilde{r}_{\rm eq}} 4\pi \tilde{r}^2 d\tilde{r} = \frac{4}{3}\pi \, \tilde{r}_{\rm eq}^3 \,, \tag{3.23}$$

which translates into

$$\mathcal{J}_{\rm BH} = \frac{4}{3}\pi \,\tilde{r}_{\rm T}^3 \,\mathcal{K}_{\rm BH} \quad \text{with} \quad \mathcal{K}_{\rm BH} = \left\{\frac{M_{\rm T}}{M_{\rm BH}}\right\}^2. \tag{3.24}$$

At the transition mass $M_{\rm T}$, both definitions (3.22) and (3.24) yield the same value of 1 for $\mathcal{K}_{\rm BH}$. We leave it to the interested reader to show that definitions (3.15), (3.17) and (3.20) boil down to Eq. (3.22) and (3.24) when the saturation density $\rho_{\rm sat}$ is equal to $\rho_{\rm B_1}$.

We also remark that for very light black holes, the integral $\mathcal{K}_{\rm BH}$ is a slowly varying function of PBH mass which becomes eventually dominated by $-2\ln(m)$ with $m \equiv M_{\rm BH}/{\rm M}_{\odot}$. Conversely, in the heavy PBH regime, $\mathcal{K}_{\rm BH}$ decreases like m^{-2} . This will have important consequences on the bounds derived in section 4. In particular, at fixed DM parameters, we anticipate that the annihilation rate $\Gamma_{\rm BH}$ scales like $-m^3\ln(m)$ in the low PBH mass regime and like m for heavy objects owing to the $r_{\rm S}^3 \propto m^3$ term in the definition (3.10).

In appendix B.1, we take into account the Schwarzschild radius in the minispike structure, and calculate integral (3.10) by setting the lower bound \tilde{r}_{\min} equal to 1. New expressions for \mathcal{K}_{BH} are given, which are very close to those derived in this section. In Fig. 4 for instance, point T lies at radius $\tilde{r}_T = 1.14 \times 10^{13}$ and mass $M_T = 5.15 \times 10^{-10} \ \mathrm{M}_{\odot}$. For PBH mass smaller than M_T , the correction to \mathcal{K}_{BH} is equal to $1/\tilde{r}_T^3 = 6.83 \times 10^{-40}$ and is vanishingly small. For heavy objects, the correction to \mathcal{K}_{BH} starts to be sensible when \tilde{r}_H approaches 1, i.e. for masses larger than $M_T \tilde{r}_T^{3/2} \simeq 1.97 \times 10^{10} \ \mathrm{M}_{\odot}$. As shown in Eq. (B.3), super-heavy black holes have a masse cut-off at $1.54 \times 10^{17} \ \mathrm{M}_{\odot}$, a value above which \mathcal{K}_{BH} vanishes. This bound is close to the amount of matter enclosed in the causal horizon at matter-radiation equality.

As DM particles orbit around the central PBH, they explore different regions of the minispike while continuously annihilating with each other. The actual density profile results from the intricate interactions of all bound trajectories. In this context, some analyses [28, 29] indicate that the saturation plateau should be replaced by a weak cusp with slope lying between 0 and 1/2. These publications explore the formation of black holes at the centers of already existing DM clumps during the matter dominated era. These clumps are dragged in turn by the collapsing central objects and compressed through adiabatic contraction, yielding very dense spikes which are subsequently erased by self-annihilations. In [29], the DM profile in the spike is evolved with time by integrating numerically the Botlzmann equation while assuming a power law in energy for the initial phase space distribution function. A weak cusp is showed to develop, which gradually extends.

In this article, the context is different since DM collapses during the radiation era around already existing PBHs. The initial phase space density is also completely determined, with a velocity distribution far from spherical. A dedicated analysis is well beyond the scope of this work though. Results will be derived hereafter by modeling DM annihilations through the formation of a saturation plateau which grows as time goes on. In appendix B.2, we nevertheless explore the effect on \mathcal{K}_{BH} of replacing the saturation plateau by a weak cusp with slope 1/2. The inner profile becomes

$$\rho(\tilde{r} \le \tilde{r}_{\text{sat}}) = \rho_{\text{sat}} \left(\tilde{r}_{\text{sat}}/\tilde{r}\right)^{1/2} . \tag{3.25}$$

We remark that \mathcal{K}_{BH} increases at most by 50% and does not change much. Replacing the saturation plateau by the weak cusp of [28, 29] implies a moderate increase of the annihilation rate Γ_{BH} and makes us confident about our procedure.

3.3 Numerical results

The calculation of \mathcal{J}_{BH} is performed numerically, using for the post-collapse DM density $\rho(\tilde{r})$ either the result of integral (2.4) or the soft approximation (2.46). The former procedure is time consuming, whereas the latter method allows to rapidly derive fairly accurate results as showed at the end of this section. A saturation plateau is always assumed.

The solid black curves in the panels of Fig. 5 feature the variations of $\Gamma_{\rm BH}$ as a function of PBH mass in the case of our fiducial configuration with a 1 TeV particle, a kinetic decoupling parameter $x_{\rm kd}$ of 10^4 and an annihilation cross-section $\langle \sigma_{\rm ann} v \rangle$ equal to its thermal value of $3 \times 10^{-26}~{\rm cm}^3~{\rm s}^{-1}$. The minispike annihilation rate is calculated at a redshift z of 10^3 . The effect of varying only one of these parameters is featured by the other curves. In the left panel, we explore how the solid line is modified by a change of redshift (dotted short-dashed) or by an increase of $\langle \sigma_{\rm ann} v \rangle$ (long-dashed). In the right panel, we decrease the kinetic decoupling parameter (dotted short-dashed) or the WIMP mass (long-dashed).

We observe that all curves exhibit the same behavior, with a characteristic power-law increase of the annihilation rate with PBH mass. We notice the existence of two distinct regimes. The spectral index is 3 at low masses and switches to 1 for heavy objects. As showed by the orange dots, the transition takes place approximately at $M_{\rm T}$. This mass is calculated for each set of parameters together with $\Gamma_{\rm BH}$, and positioned on the corresponding curve. All curves feature an inflection at the orange dots. For completeness, we have also included the blue dots at which the PBH mass is equal to M_1 .

The annihilation rate exhibits a rich diversity of behaviors. Changing the redshift for instance does not affect Γ_{BH} at low PBH mass, as showed by the dotted short-dashed line of the left panel. This is a remarkable result. Should DM minispikes be discovered around light black holes, we anticipate that their absolute luminosities would remain constant as the universe expands. This absence of variability would be a smoking gun signature for such objects insofar as other sources, like stars, are expected to evolve with redshift.

Another noticeable property is featured by the dotted short-dashed curve of the right panel. Modifying the kinetic decoupling parameter $x_{\rm kd}$ has no effect on $\Gamma_{\rm BH}$ for heavy black holes. In this regime, the annihilation rate depends furthermore linearly on PBH mass. We anticipate that the limits on the contribution of PBHs to the astronomical DM, derived in section 4.1, depend only on WIMP mass, and neither on $x_{\rm kd}$ nor on $M_{\rm BH}$. In summary, to understand this complex phenomenology, we need to derive scaling relations for

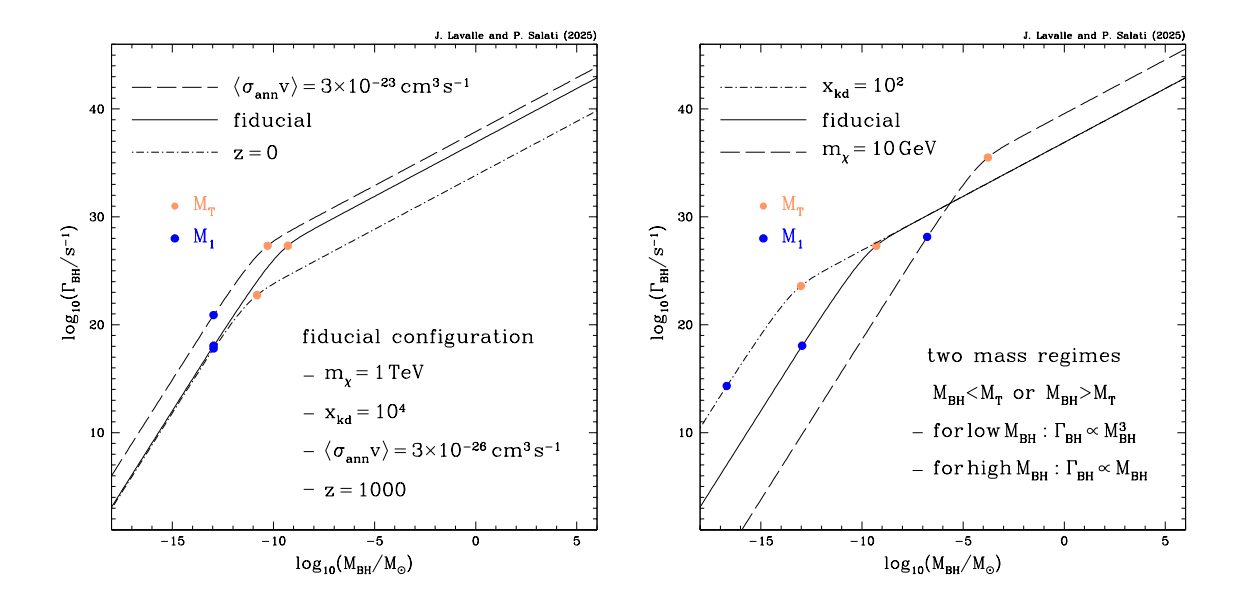


Figure 5. The DM annihilation rate of minispikes is plotted as a function of PBH mass. The solid line corresponds to the fiducial case as specified in the left panel, while the other curves feature each the effect on $\Gamma_{\rm BH}$ of modifying one of the parameters of the model. In the left panel, the redshift is decreased from 10^3 (post-recombination epoch) to 0 (today). The dotted short-dashed line shifts downward only at high PBH mass. The long-dashed curve shows how increasing the annihilation cross-section $\langle \sigma_{\rm ann} v \rangle$ by three orders of magnitude acts on $\Gamma_{\rm BH}$. In the right panel, decreasing the kinetic decoupling parameter $x_{\rm kd}$ from 10^4 down to 10^2 makes the annihilation rate grow only at low masses (dotted short-dashed). Varying the WIMP mass m_χ from 1 TeV down to 10 GeV induces an increase of $\Gamma_{\rm BH}$ at high mass but a decrease at low mass (long-dashed). All the curves indicate that the annihilation rate increases with $M_{\rm BH}$ as a power law with index 3 at low mass and 1 at high mass. These behaviors are further discussed in the text.

the annihilation rate as a function of model parameters in both the low and the high PBH mass regimes.

• $M_{\rm BH} \leq M_{\rm T}$

To commence, we remark that the extension $\tilde{r}_{\rm sat}$ of the saturation plateau, in reduced coordinates, does not vary with PBH mass as long as $M_{\rm BH} \leq M_{\rm T}$. This is true whether $\rho_{\rm sat}$ is larger or smaller than $\rho_{\rm B_1}$. In the left panel of Fig. 4 for instance, we observe that $\tilde{r}_{\rm sat}$ is equal to $\tilde{r}_{\rm T}$ below $M_{\rm T}$, and is constant. Injecting relations (3.15), (3.17) or (3.22) in definition (3.10) yields the same expression

$$\Gamma_{\rm BH} = \frac{1}{2} \langle \sigma_{\rm ann} v \rangle \left\{ \frac{\rho_{\rm sat}}{m_{\chi}} \right\}^2 r_{\rm S}^3 \times \frac{4}{3} \pi \, \tilde{r}_{\rm T}^3 \times \mathcal{K}_{3/2} \,, \tag{3.26}$$

where $K_{3/2}$ is identified with $K_{\rm BH}$. Refined expressions for $K_{3/2}$ are collected in appendix B.1 when the Schwarzschild radius of the black hole is taken into account. More specifically, $K_{3/2}$ is defined by (B.6) when $\rho_{\rm sat} \geq \rho_{\rm B_1}$ and $M_1 \leq M_{\rm BH} \leq M_{\rm T}$. Alternatively, expression (B.5) can be used if $\rho_{\rm sat} \geq \rho_{\rm B_1}$ and $M_{\rm BH} \leq M_1$, or if $\rho_{\rm sat} \leq \rho_{\rm B_1}$ and $M_{\rm BH} \leq M_{\rm T}$. In the latter situation, the mass $M_{\rm T}$ is smaller than M_1 , and $K_{3/2}$ is also given by (B.1). Parameter $K_{3/2}$ is of order $\mathcal{O}(1)$.

At low PBH mass, the saturation plateau is surrounded by a DM layer with slope 3/2,

and the saturation density scales like

$$\rho_{\rm sat} \propto \tilde{r}_{\rm T}^{-3/2} \quad \text{hence} \quad \rho_{\rm sat}^2 \, \tilde{r}_{\rm T}^3 \propto \text{constant.}$$
(3.27)

Using Eq. (3.12) to replace $\tilde{r}_{\rm T}$ in relation (3.26) makes the saturation density $\rho_{\rm sat}$ cancel out. The cosmological DM density at kinetic decoupling $\rho_i^{\rm kd}$ appears, which we express as a function of m_{χ} , $x_{\rm kd}$ and the effective number $h_{\rm eff}(T_{\rm kd})$ of entropic degrees of freedom at that time. Tossing all these ingredients together, we derive the scaling relation

$$\Gamma_{\rm BH}^{(3/2)} = (1.03 \times 10^{66} \,\mathrm{s}^{-1}) \,\mathcal{K}_{3/2} \left\{ \frac{h_{\rm eff}(T_{\rm kd})}{h_{\rm eff}(T_{\rm eq})} \right\}^2 \,\mathcal{S} \,\mu^4 \,x_{\rm kd}^{-3} \,m^3 \,, \tag{3.28}$$

where S is the annihilation cross-section expressed in units of its thermal value, μ is the WIMP mass in TeV and m is the PBH mass in solar units. The effective number of entropic degrees of freedom at matter-radiation equality is denoted by $h_{\rm eff}(T_{\rm eq})$. We notice that the duration $\Delta t = t_{\rm U}(z) - t_{\rm eq}$ has disappeared. The minispike annihilation rate does not depend on redshift. As time goes on, the density $\rho_{\rm sat}$ of the saturation sphere decreases, but its radius $\tilde{r}_{\rm T}$ increases in such a way that it compensates for that effect as showed by the scaling (3.27). According to relation (3.28), increasing $\langle \sigma_{\rm ann} v \rangle$ makes the solid curve of the left panel shift upward, while decreasing m_{χ} in the right panel makes it shift downward. Scaling (3.28) allows us to understand the results displayed in Fig. 5 in the low PBH mass regime.

For heavy black holes, the extension $\tilde{r}_{\rm sat}$ of the saturation plateau decreases with PBH mass like $M_{\rm BH}^{-2}$. Two cases must be distinguished depending on how the saturation density $\rho_{\rm sat}$ compares with $\rho_{\rm B_1}$.

• $M_{\rm BH} \geq M_{\rm T}$ and $\rho_{\rm sat} \geq \rho_{\rm B_1}$

Replacing \mathcal{J}_{BH} by expression (3.20) in its definition (3.10), we can write the annihilation rate as

$$\Gamma_{\rm BH} = \frac{1}{2} \langle \sigma_{\rm ann} v \rangle \left\{ \frac{\rho_{\rm sat}}{m_{\chi}} \right\}^2 r_{\rm S}^3 \times \frac{4}{3} \pi \, \tilde{r}_{\rm T}^3 \times \left\{ \frac{M_{\rm T}}{M_{\rm BH}} \right\}^2 \mathcal{K}_{9/4} \,. \tag{3.29}$$

The coefficient $\mathcal{K}_{9/4}$ can be derived from relations (B.7) and (B.8) depending on whether $\tilde{r}_{\rm H}$ is larger, or smaller, than 1. This yields

$$\mathcal{K}_{9/4} = \begin{cases}
3 - (1/\tilde{r}_{H}^{3}) - 2(\tilde{r}_{H}/\tilde{r}_{E})^{3/2} & \text{if } \tilde{r}_{H} \ge 1, \\
2\tilde{r}_{H}^{3/2} \left\{ 1 - (1/\tilde{r}_{eq})^{3/2} \right\} & \text{if } \tilde{r}_{H} \le 1.
\end{cases}$$
(3.30)

For super-heavy black holes, the minispike radius may become smaller than the Schwarzschild radius and $\mathcal{K}_{9/4}$ vanishes.

In this regime, the transition mass $m_{\rm T} \equiv M_{\rm T}/{\rm M}_{\odot}$ is given by (3.13). The saturation radius $\tilde{r}_{\rm T}$ cancels out from Eq. (3.29). It is replaced by the radius of influence $\tilde{r}_{\rm T}^0$ of a solar mass black hole at the exact time t_i when the cosmological DM density is equal to

$$\rho_i = \sqrt{\frac{\pi^3}{2}} \frac{\rho_{\text{sat}}}{\mathcal{I}_{9/4}^{\text{asy}}} \quad \text{where} \quad \rho_{\text{sat}} \equiv \rho_{9/4}(\tilde{r}_{\text{T}}, m_{\text{T}}) \equiv \rho_{9/4}(\tilde{r}_{\text{T}}^0, 1) \,. \tag{3.31}$$

The saturation sphere is surrounded by a DM layer with slope 9/4. Once the cosmological density ρ_i has been determined, the reduced radius $\tilde{r}_{\rm T}^0$ can be readily obtained as explained

in appendix A.2. Both quantities fulfill the relation

$$C_2(T_i) = \left\{\frac{\tilde{r}_{\mathrm{T}}^0}{\tilde{r}_{\mathrm{eq}}^0}\right\} \left\{\frac{\rho_i}{\rho_i^{\mathrm{eq}}}\right\}^{4/9} \quad \text{with} \quad C_2(T_i) \equiv \left\{\frac{g_{\mathrm{eff}}(T_{\mathrm{eq}})}{g_{\mathrm{eff}}(T_i)}\right\}^{1/3} \left\{\frac{h_{\mathrm{eff}}(T_i)}{h_{\mathrm{eff}}(T_{\mathrm{eq}})}\right\}^{4/9}, \tag{3.32}$$

where T_i denotes the temperature of the primordial plasma at time t_i while ρ_i^{eq} is the DM density at matter-radiation equality. In appendix A.2, we explain how \tilde{r}_{T}^0 can be derived from ρ_i , together with T_i and C_2 . Replacing \tilde{r}_{T}^0 by its expression in terms of ρ_{sat} and C_2 in Eq. (3.29), it is straightforward to establish the new scaling relation for the minispike annihilation rate

$$\Gamma_{\rm BH}^{(9/4)} = \left(6.26 \times 10^{34} \,\mathrm{s}^{-1}\right) \mathcal{K}_{9/4} \,\mathcal{C}_2^3 \,\mathcal{S}^{1/3} \,\mu^{-4/3} \,\tau^{-2/3} \,m\,,\tag{3.33}$$

where τ denotes the duration Δt expressed in units of 10^{15} s. Several remarks are in order.

- The annihilation rate scales now linearly with PBH mass. In Fig. 5, this new scaling appears clearly on all curves above the orange dots.
- As already discussed, the kinetic decoupling parameter x_{kd} does not come into play in the annihilation rate (3.33), in agreement with the behavior of the dotted short-dashed curve of the right panel.
- The annihilation rate is a decreasing function of the duration τ . As time goes on, minispikes around massive objects have a declining absolute luminosity. This explains why the high-mass part of the dotted short-dashed curve of the left panel shifts downward when the redshift decreases from 10^3 down to 0.
- As featured by the long-dashed curve of the right panel above the orange dot, the lighter the DM species, the larger the annihilation rate. Conversely, this rate decreases at low PBH mass. All curves are shifted rightward and upward in the $(M_{\rm BH}, \Gamma_{\rm BH})$ plane as m_χ is decreased.
- We finally observe that the rate $\Gamma_{\rm BH}$ is an increasing function of the annihilation cross-section $\langle \sigma_{\rm ann} v \rangle$.

• $M_{\rm BH} \geq M_{\rm T}$ and $\rho_{\rm sat} \leq \rho_{\rm B_1}$

In this configuration, the saturation plateau extends up to the surface of the minispike. The saturation radius $\tilde{r}_{\rm sat}$ can be identified with the influence radius $\tilde{r}_{\rm eq}$ of the object at matter-radiation equality. The radius $\tilde{r}_{\rm T}$ is still defined by (3.12) while the transition mass $m_{\rm T} \equiv M_{\rm T}/{\rm M}_{\odot}$ is now given by (3.21) so that

$$\tilde{r}_{\text{sat}} \equiv \tilde{r}_{\text{eq}}(m) = \tilde{r}_{\text{T}} (m/m_{\text{T}})^{-2/3} .$$
 (3.34)

Using expressions (3.24) and (B.2) in definition (3.10), we can write the annihilation rate as

$$\Gamma_{\rm BH} = \frac{1}{2} \langle \sigma_{\rm ann} v \rangle \left\{ \frac{\rho_{\rm sat}}{m_{\chi}} \right\}^2 r_{\rm S}^3 \times \frac{4}{3} \pi \, \tilde{r}_{\rm T}^3 \times \left\{ \frac{M_{\rm T}}{M_{\rm BH}} \right\}^2 \mathcal{K}_0 \,, \tag{3.35}$$

where $\mathcal{K}_0 = 1 - (1/\tilde{r}_{eq})^3$. The scaling of the annihilation rate as a function of the parameters of the model can be described by

$$\Gamma_{\rm BH}^{(0)} = (4.26 \times 10^{46} \,\mathrm{s}^{-1}) \,\mathcal{K}_0 \,\mathcal{S}^{-1} \,\tau^{-2} \,m.$$
(3.36)

The annihilation rate is still linear in PBH mass. Its decline with duration Δt is faster than in the previous configuration where $\rho_{\rm sat} \geq \rho_{\rm B_1}$. But the most important difference is that $\Gamma_{\rm BH}$ is now a decreasing function of the annihilation cross-section, in contrast with the other situations. We anticipate that the annihilation rate should exhibit at some point a maximum depending on $M_{\rm BH}$ and $\langle \sigma_{\rm ann} v \rangle$. Setting the other parameters fixed while keeping in mind that increasing $\langle \sigma_{\rm ann} v \rangle$ always makes the saturation density drop by virtue of relation (3.8), we can distinguish two cases.

1. If $M_{\rm BH}$ is larger than M_1 , the annihilation rate increases with $\langle \sigma_{\rm ann} v \rangle$ as long as $\rho_{\rm sat}$ exceeds $\rho_{\rm B_1}$. When $\rho_{\rm sat}$ becomes smaller than $\rho_{\rm B_1}$, the transition mass $M_{\rm T}$ gets smaller than M_1 . We are in the situation where the scaling (3.36) applies, with $\Gamma_{\rm BH}$ decreasing now with $\langle \sigma_{\rm ann} v \rangle$. The maximum of $\Gamma_{\rm BH}$ as a function of $\langle \sigma_{\rm ann} v \rangle$ is therefore reached when $\rho_{\rm sat}$ and $\rho_{\rm B_1}$ are equal, i.e. at the critical cross-section

$$\langle \sigma_{\rm ann} v \rangle_{\rm crit} = \frac{m_{\chi}}{\rho_{\rm B_1} \Delta t} = (1.32 \times 10^{-17} \,\mathrm{cm}^3 \,\mathrm{s}^{-1}) \,\mu \,\tau^{-1} \,.$$
 (3.37)

The numerical value derived here does not depend on PBH mass. Notice that the post-collapse DM density ρ_{B_1} is a constant as showed in table 1. The critical cross-section $\langle \sigma_{ann} v \rangle_{crit}$ increases with WIMP mass and decreases as cosmic time goes on.

2. If the PBH mass is smaller than M_1 , the maximum of $\Gamma_{\rm BH}$ as a function of $\langle \sigma_{\rm ann} v \rangle$ is now reached when the transition mass $M_{\rm T}$ becomes equal to $M_{\rm BH}$. The corresponding saturation density can be obtained from (3.12) and (3.21), with the masses $m_{\rm T}$ and $m_{\rm T}$ set equal. Defining the annihilation cross-section at the peak by the ratio $m_{\chi}/(\rho_{\rm sat}\Delta t)$ leads to the scaling relation

$$\langle \sigma_{\rm ann} v \rangle_{\rm crit} = (5.94 \times 10^{-36} \,\mathrm{cm}^3 \,\mathrm{s}^{-1}) \left\{ \frac{h_{\rm eff}(T_{\rm eq})}{h_{\rm eff}(T_{\rm kd})} \right\} \mu^{-2} x_{\rm kd}^{3/2} \tau^{-1} \,m^{-1} \,.$$
 (3.38)

We remark that this expression yields the same result as Eq. (3.37) when $M_{\rm BH}$ is set equal to M_1 .

3.4 Using the soft approximation for the annihilation rate

To close this section, we explore the impact on the minispike annihilation rate $\Gamma_{\rm BH}$ of using the soft approximation (2.46) instead of the result of integral (2.4) to derive the post-collapse DM density $\rho(\tilde{r})$. In the left panel of Fig. 6, we plot the relative difference between both rates as a function of PBH mass for three different models and redshift z=600. The agreement between the full numerical result, and the calculation based on the soft approximation, is fairly good for a 1 TeV DM particle (solid blue). Over most of the PBH mass range, the soft approximation yields the numerical result up to a relative error of $\pm 10\%$. The error reaches however +16% and -14% at PBH mass 10^{-13} M_{\odot} and 10^{-9} M_{\odot}. This is already an excellent result given that $\Gamma_{\rm BH}$ varies logarithmically over more than 39 decades.

The situation deteriorates though for smaller DM masses. For a 1 GeV WIMP, the error is acceptably bounded by $\pm 10\%$, except for PBH masses between 10^{-11} and 10^{-3} M $_{\odot}$. The dotted short-dashed orange curve exhibits a peak at 5×10^{-6} M $_{\odot}$ where it reaches +35%. The situation worsens even further in the 1 MeV case (dotted long-dashed red) for which the error exceeds +14% between 3×10^{-3} and 10^4 M $_{\odot}$, peaking at +70% for a mass of 4.5×10^2 M $_{\odot}$. As already noticed at the end of section 2.3, the post-collapse density $\rho(\tilde{r})$ is overestimated

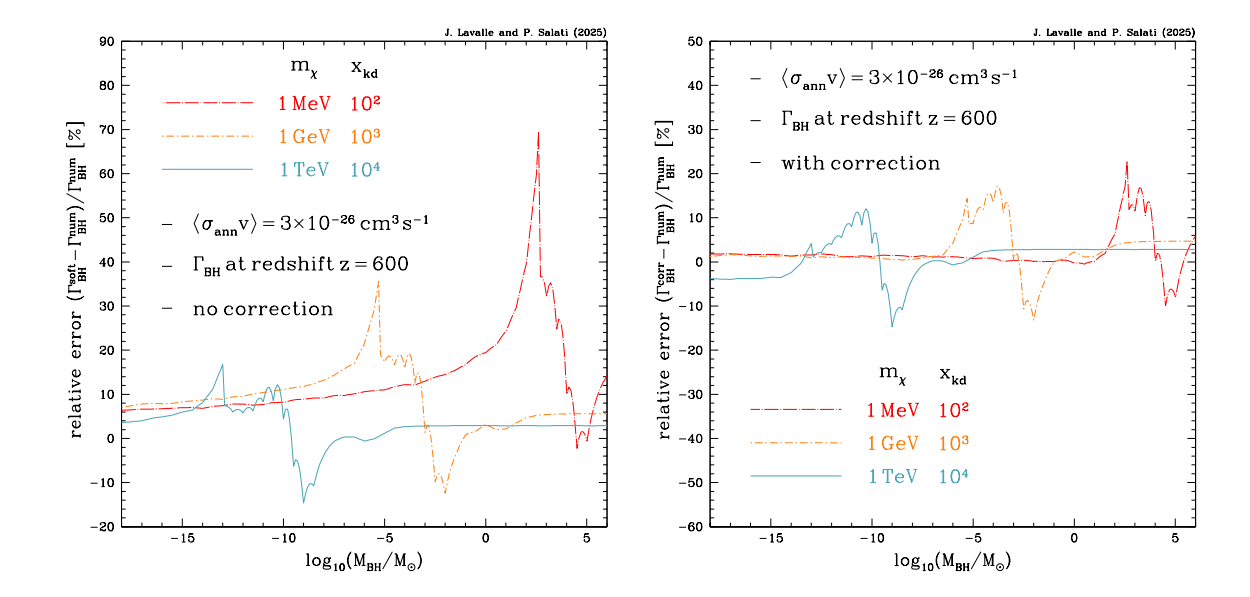


Figure 6. The relative error induced on the minispike annihilation rate $\Gamma_{\rm BH}$ by using the soft approximation (2.46) instead of the numerical integral (2.4) for the DM post-collapse density is presented in the left panel as a function of PBH mass. Three representative configurations have been selected for the WIMP mass m_{χ} and the kinetic decoupling parameter $x_{\rm kd}$. The annihilation rate is derived at a redshift z of 600, while a thermal annihilation cross-section is assumed. In the **right panel**, the soft approximation has been corrected close to the minispike surface by using expansions (3.39). The agreement with the numerical result improves significantly.

by the soft approximation (2.46) close to the surfaces of minispikes, and so is the annihilation rate. This effect is most important for PBH masses close to M_1 . The peaks, which the dotted short-dashed orange and dotted long-dashed red curves exhibit, can be actually associated to the critical mass M_1 , respectively equal to 5.282×10^{-6} and 4.512×10^2 M_{\odot}.

The larger the volume of the surface layer where the density is overestimated, relative to the volume of the entire minispike, the larger the annihilation rate derived using the soft approximation compared to the full numerical result. This effect is most sensitive for light DM species. Actually, at fixed kinetic decoupling parameter $x_{\rm kd}$, the smaller m_{χ} , the smaller the decoupling temperature $T_{\rm kd}$. In the phase diagram of Fig. 1, the dotted short-dashed red line corresponding to $\tilde{r}_{\rm kd}$ is shifted upward as $T_{\rm kd}$ decreases, hence a larger critical mass M_1 and a smaller extension of the corresponding minispike in reduced coordinates. The overestimation of $\rho(\tilde{r})$ becomes more acute in this situation than for heavier DM species.

In the next section, we will concentrate on DM particles heavier than a few tens of GeV. In that mass range, the soft approximation can perfectly be used to calculate decent values of $\Gamma_{\rm BH}$. One of the goals of this work is nevertheless to derive an acceptable approximation for the post-collapse density $\rho(\tilde{r})$, which ought to be valid over the entire parameter space. That is why we have slightly corrected the soft approximation by respectively replacing, in the asymptotic expressions (2.10) and (2.13), the integrals $\mathcal{I}_{3/2}^{\rm asy}$ and $\mathcal{I}_{9/4}^{\rm asy}$ by

$$\mathcal{I}_{3/2} = \mathcal{I}_{3/2}^{\text{asy}} - \frac{3\pi}{8} \frac{\tilde{r}}{\tilde{r}_{\text{eq}}} \quad \text{and} \quad \mathcal{I}_{9/4} = \mathcal{I}_{9/4}^{\text{asy}} - \frac{4}{3} \sqrt{2\pi} \left\{ \frac{\tilde{r}}{\tilde{r}_{\text{eq}}} \right\}^{3/4}.$$
 (3.39)

These relations have been derived in our previous study⁴[26]. The profile close to the surface is now better described, and so is the annihilation rate. As is clear in the right panel of Fig. 6, the tension between the approximated and fully numerical results for $\Gamma_{\rm BH}$ is alleviated by taking into account expansions (3.39). Although there is not much of an effect at 1 TeV, the situation dramatically improves for the other cases, with a discrepancy lying almost always in the band $\pm 15\%$. The peaks of the left panel have been substantially erased. In particular, while $\Gamma_{\rm BH}$ spans more than 66 decades in the 1 MeV case, the error is now confined between -10% and +22%. These results are remarkable and make us confident that the soft approximation (2.46), once corrected by (3.39), can be safely used for fast and robust calculations of the post-collapse density $\rho(\tilde{r})$ and minispike annihilation rate $\Gamma_{\rm BH}$. We will use it in the next section.

4 Observational constraints

In the mixed scenario explored in this article, primordial black holes and thermal species contribute respectively a fraction $f_{\rm BH}$ and $f_{\rm DM} \equiv 1-f_{\rm BH}$ to the astronomical DM. In the previous sections, results were derived assuming a fraction $f_{\rm DM}$ of 1. From now on, that fraction is left free to vary in the range from 0 (no WIMPs) to 1 (no PBHs). Whatever the value of $f_{\rm DM}$, the total amount of DM has been fixed once and for all by observations of the CMB [34]. All the relations previously derived between temperature and energy density of the primordial plasma, cosmological time and radius of influence for a given PBH mass can still be used.

The only modification bears on the cosmological density ρ_i of DM thermal particles, which is to be multiplied by a factor $f_{\rm DM} \leq 1$. According to its definition (2.4), so is the post-collapse density $\rho(\tilde{r})$. On the other hand, the saturation density $\rho_{\rm sat}$ is only determined by the WIMP mass m_{χ} and annihilation cross-section $\langle \sigma_{\rm ann} v \rangle$, as well as by the duration Δt . Once WIMP annihilations are taken into account, the DM density of minispikes is given by relation (3.9) where the post-collapse density $\rho(\tilde{r})$ is rescaled by a factor $f_{\rm DM}$. This yields

$$\rho(t, \tilde{r}) = f_{\rm DM} \times \frac{\rho'_{\rm sat} \, \rho(\tilde{r})}{\rho'_{\rm sat} + \rho(\tilde{r})} \quad \text{where} \quad \rho'_{\rm sat} \equiv \rho_{\rm sat} / f_{\rm DM} \,. \tag{4.1}$$

Up to a global rescaling by a factor $f_{\rm DM}$, the entire minispike structure is the same as that considered in the previous section, but now with a saturation density $\rho'_{\rm sat}$ instead of $\rho_{\rm sat}$. The smaller the fraction $f_{\rm DM}$, the larger $\rho'_{\rm sat}$. This leads us to the scaling relation for the annihilation rate

$$\Gamma_{\rm BH} \left\{ \rho_{\rm sat}, f_{\rm DM} \rho_i \right\} = f_{\rm DM}^2 \times \Gamma_{\rm BH} \left\{ \rho_{\rm sat}', \rho_i \right\}. \tag{4.2}$$

This relation has immediate implications for the asymptotic expressions (3.28), (3.33) and (3.36) derived in section 3.3.

Using relation (3.12), we first remark that the radius of the saturation plateau shrinks with $f_{\rm DM}$ like

$$\tilde{r}_{\rm T} \propto 1/\rho'_{\rm sat}^{2/3} \propto f_{\rm DM}^{2/3}$$
. (4.3)

The coordinates of the transition point T in the (\tilde{r}, M_{BH}) plane change. In the phase diagram of Fig. 4 for instance, T is shifted toward the upper-left direction along the line connecting points B_1 and B_2 . The coefficient C_2 of Eq. (3.33) corresponds now to ρ'_{sat} and grows slightly.

⁴More precisely, we have borrowed from [26] expansions (5.22) for $\rho_{3/2}$ and (5.50) for $\rho_{9/4}$.

Depending on whether the saturation density is larger or smaller than ρ_{B_1} , the transition mass M_T increases like

$$m_{\rm T} \propto f_{\rm DM}^{-1/3}$$
 if $\rho_{\rm sat} \ge \rho_{\rm B_1}$ or $\propto f_{\rm DM}^{-1}$ if $\rho'_{\rm sat} \le \rho_{\rm B_1}$. (4.4)

Making use of the rescaling relation (4.2), we realize that the asymptotic expressions (3.28) and (3.33) are still valid, with same normalization coefficients, but include now the fraction of DM species with

 $\Gamma_{\rm BH}^{(3/2)} \propto f_{\rm DM}^2 \quad \text{while} \quad \Gamma_{\rm BH}^{(9/4)} \propto f_{\rm DM}^{4/3} \,.$ (4.5)

The coefficients $\mathcal{K}_{3/2}$ and $\mathcal{K}_{9/4}$ also vary as they depend on \tilde{r}_{T} . Quite the contrary, $\Gamma_{\mathrm{BH}}^{(0)}$ is not sensitive to f_{DM} . In that configuration, annihilations have completely erased the minispike structure and transformed it into a homogeneous distribution with density ρ_{sat} .

Having understood how the annihilation rate $\Gamma_{\rm BH}$ depends on the WIMP fraction $f_{\rm DM}$, we are ready to explore two kinds of constraints on our mixed DM scenario.

- First, we can set limits on the abundance $f_{\rm BH}$ of PBHs assuming that most of the DM is made of thermal species. The goal is to close the asteroid window between 10^{-16} and 10^{-11} M_☉, supplementing the bounds already derived in the literature [6, 7].
- Then, if GW observatories were to discover PBHs and measure their mass and contribution to the DM, stringent limits could be derived on the properties of WIMPs. This point has been disregarded in the literature and is one of the novelties of this work.

The constraints discussed hereafter arise from the signals produced by a population of annihilating minispikes during the post-recombination era. We will concentrate on the γ -ray extragalactic background, and on the injection of energy in the primordial plasma in connection with CMB angular distortions. As a word of caution, we wish to warn the reader that what follows is mostly about setting up a detailed methodology to extract and interpret constraints. A detailed data analysis and statistical inference of the bounds is left to future and dedicated work.

4.1 Bounds on the fraction $f_{\rm BH}$ of primordial black holes

4.1.1 Cosmological γ -ray background

If a fraction $f_{\rm BH}$ of the DM is made of PBHs with monochromatic mass $M_{\rm BH}$, we expect the number density of these objects at redshift z to be

$$n_{\rm BH}(z) = \frac{f_{\rm BH} \, \rho_{\rm dm}^0}{M_{\rm BH}} \, (1+z)^3 \,,$$
 (4.6)

where the present DM density $\rho_{\rm dm}^0$ has been measured by the Planck collaboration [34] to be equal to 2.25×10^{-30} g cm⁻³. The associated DM minispikes continuously annihilate, producing standard model particles and eventually high-energy photons whose energy distribution, per annihilation event, is described by the primary spectrum

$$Q_{\gamma}^{\text{prim}}(E_{\gamma}) = \left. \frac{dN_{\gamma}}{dE_{\gamma}} \right|_{E_{\gamma}}.$$
(4.7)

A cosmological background of γ -rays is produced, with flux at the Earth

$$\Phi_{\gamma}^{\rm BH}(E_{\gamma}) = \frac{c}{4\pi} \frac{f_{\rm BH} \rho_{\rm dm}^{0}}{M_{\rm BH}} \int \frac{dz}{H(z)} \Gamma_{\rm BH}(z) e^{-\tau_{\rm opt}(E_{\gamma},z)} \mathcal{Q}_{\gamma}^{\rm prim}(E_{\gamma}'). \tag{4.8}$$

The integral is performed along the line of sight, with z running from 0 up to $(m_\chi/E_\gamma)-1$. Since high-energy photons interact with the CMB or the intergalactic medium as they propagate to the Earth, they cannot come from far away. Their flux undergoes extinction with optical depth $\tau_{\rm opt}$. The photon energy at the source is $E'_{\gamma}=(1+z)E_{\gamma}$. The annihilation rate of minispikes $\Gamma_{\rm BH}$ also depends on redshift, as showed in Fig. 5. The expansion rate of the universe at redshift z may be expressed as

$$H(z) \simeq H_0 \sqrt{\Omega_{\Lambda} + \Omega_{\rm m} (1+z)^3}, \qquad (4.9)$$

where H_0 is the Hubble constant, while $\Omega_{\rm m} = \Omega_{\rm dm} + \Omega_{\rm b}$ and Ω_{Λ} denote the matter and dark energy abundances today. Observations can set limits on the extragalactic γ -ray background, providing an upper bound on $\Phi_{\gamma}^{\rm BH}$ and eventually on the fraction $f_{\rm BH}$. The problem is quite involved though for at least two reasons

- Annihilating DM particles inside minispikes also produce electrons and positrons. These subsequently scatter on the CMB, which they convert into inverse Compton (IC) photons. This secondary component must be added to the primary source $\mathcal{Q}_{\gamma}^{\text{prim}}$.
- As regards γ-ray observations, several backgrounds must be thoroughly modeled. Interactions of high-energy cosmic ray protons and helium nuclei on the interstellar medium of the Milky Way, for instance, produce a Galactic foreground which needs to be substracted from data to get the extragalactic background. Another component arises from IC photons produced by Galactic electrons and positrons scattering on the CMB and stellar light. Such an analysis has been performed by the Fermi-LAT collaboration who derived [36] the extragalactic background, which is the sum of the isotropic background with the cumulative intensity from resolved Fermi-LAT sources. The latter needs to be modeled to extract the former, which is the only useful component for our analysis.

This onerous task has been first performed by Ando and Ishiwata [37] (see also Blanco and Hooper [38]) who considered various classes of extragalactic sources, namely blazars, star-forming galaxies and misaligned active galactic nuclei. Using the Fermi-LAT result [36], they performed a Bayesian statistical analysis to derive 95% credible lower limits on the lifetime $\tau_{\rm dm}$ of decaying DM species, for a large variety of DM masses and annihilation channels.

As originally proposed by Boucenna et al. [30], the bounds derived by Ando and Ishiwata can be recast into constraints on $f_{\rm BH}$. Actually, in our mixed scenario, each PBH with its minispike can be seen as some sort of huge particle which continuously decays. In that respect, genuine decaying DM species and annihilating minispikes around primordial black holes behave in a similar way. How these objects are clustered does not come into play. This is not quite the case with annihilation, for which concentration plays a major role.

Recasting the Ando and Ishiwata results [37] requires to take a decaying particle twice as massive as in the minispike scenario. We note that this little subtlety was actually missed in most of previous works [27, 30, 33]. As an illustration, let us consider the production of $b\bar{b}$ quark pairs. With that prescription, each b jet is always produced with the energy m_{χ} . Because of extinction, most of the photons detected at the Earth originate from the local universe. The rate of production of quark pairs, which in principle should be integrated along the line of sight, can be roughly taken at redshift $z \simeq 0$ (today) and is respectively given by

$$\frac{\rho_{\rm dm}^0 \tau_{\rm dm}^{-1}}{2m_{\chi}} \text{ (decaying DM)} \quad \text{and} \quad \frac{f_{\rm BH} \, \rho_{\rm dm}^0 \, \Gamma_{\rm BH}}{M_{\rm BH}} \text{ (minispike scenario)}. \tag{4.10}$$

Because of the correspondence between decaying DM and annihilating minispikes, the expressions in Eq. (4.10) can be equated. The lower limit $\tau_{\rm dm}^{\rm min}$ on the lifetime of a decaying DM species can be converted into a bound on PBHs, which we express as

$$f_{\rm BH}\Gamma_{\rm BH} \le \left\{\frac{M_{\rm BH}}{2m_{\chi}}\right\} \left\{\frac{1}{\tau_{\rm dm}^{\rm min}}\right\}.$$
 (4.11)

An upper limit applies on the product $f_{\rm BH}\Gamma_{\rm BH}$. Notice that $\Gamma_{\rm BH}$ also depends on $f_{\rm BH}$ through the WIMP fraction $f_{\rm DM}=1-f_{\rm BH}$. We remark that $f_{\rm BH}\Gamma_{\rm BH}$ vanishes for $f_{\rm BH}=0$ or 1, and that it reaches a maximum while $f_{\rm BH}$ runs from 0 to 1. If that maximum is smaller than the right-hand side term of Eq. (4.11), no limit applies on the fraction of PBHs. In the opposite situation, $f_{\rm BH}$ must be either small or close to 1. An entire range of values is excluded, over which $f_{\rm BH}\Gamma_{\rm BH}$ exceeds the Ando and Ishiwata constraint. Before proceeding any further, we have to emphasize that formally, since minispike annihilation has a time dependence that differs from standard dilution, it is very likely that the bound on decaying DM can actually not be recast as straightforwardly in terms of a bound on our mixed PBH-WIMP scenario. A more involved analysis is left to future work.

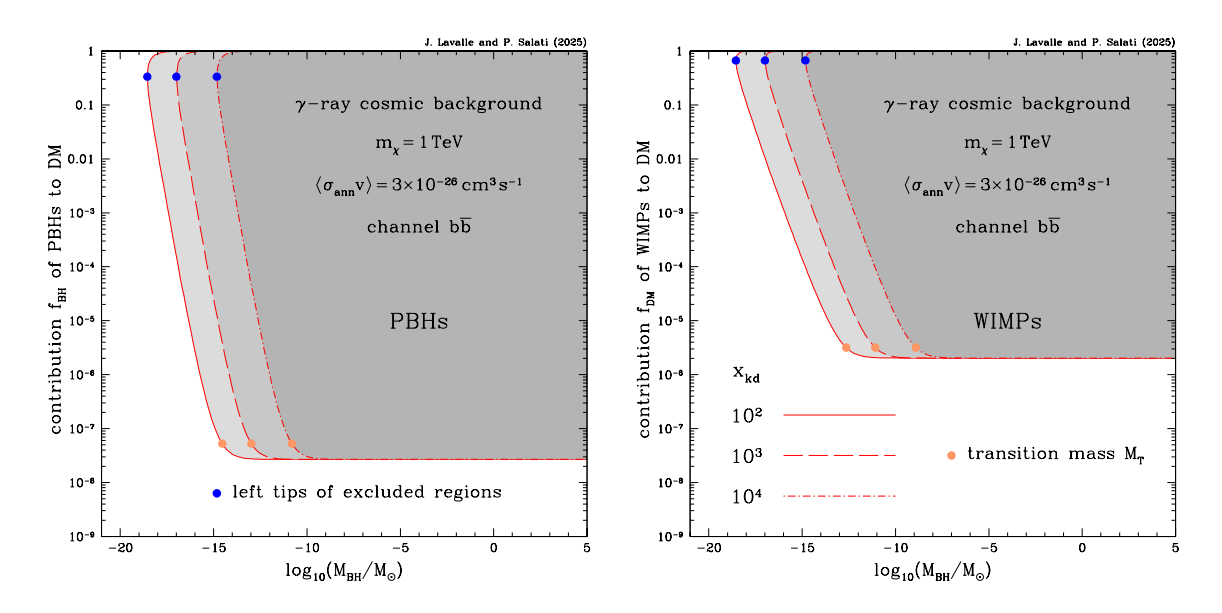


Figure 7. The Fermi-LAT measurements [36] of the extragalactic γ -ray background yield constraints on the contributions of PBHs and thermal species to the overall DM, respectively displayed in the left and right panels. Ando and Ishiwata [37] have used the Fermi-LAT data to set bounds on decaying DM particles, which have been recast into the forbidden gray regions in the case of a 1 TeV WIMP with thermal annihilation cross-section. The various shades of gray and contour types correspond to different values of the kinetic decoupling parameter $x_{\rm kd}$, as indicated. Each panel features the same excluded domains observed from a different perspective, depending on whether $f_{\rm BH}$ or $f_{\rm DM}$ is used. For heavy black holes, the PBH fraction $f_{\rm BH}$ is constrained to be either very small (left panel) or very close to 1 (right panel). As already noticed by [22], PBHs contribute all or almost nothing to the astronomical DM. Light PBHs evade the γ -ray constraint to the left of the blue dots.

In Fig. 7, we have used the results that Ando and Ishiwata have displayed in the Fig. 3 of their analysis [37]. The lower limit $\tau_{\rm dm}^{\rm min}$ on the lifetime of a 2 TeV DM particle decaying into $b\bar{b}$ pairs is found to be 3.02×10^{27} s. In the left panel, the regions excluded by the cosmological

 γ -ray background are plotted in the $(M_{\rm BH}, f_{\rm BH})$ plane for a 1 TeV annihilating DM species, and three different values of the kinetic decoupling parameter $x_{\rm kd}$, each corresponding to a particular shade of gray. The forbidden domains are delineated by a red line whose type depends on $x_{\rm kd}$ as specified in the right panel. For heavy black holes, the fraction $f_{\rm BH}$ cannot exceed 2.69×10^{-8} whatever $M_{\rm BH}$ and $x_{\rm kd}$. On the contrary, for light PBHs, the upper limit on $f_{\rm BH}$ becomes less stringent. It even disappears below some critical mass, respectively equal to 2.81×10^{-19} , 1.01×10^{-17} and 1.50×10^{-15} M $_{\odot}$ as $x_{\rm kd}$ is increased from 10^2 to 10^4 . At the left tips of the gray excluded areas, corresponding to the blue dots in both panels, the PBH fraction is equal to 1/3. Above that value, the red contours turn back rightward, while a lower limit, very close to 1, applies this time on $f_{\rm BH}$.

To observe it, the gray forbidden zones of the left panel have been plotted in the right panel as a function of WIMP fraction $f_{\rm DM}$. The lower limit on $f_{\rm BH}$ translates into an upper bound on $f_{\rm DM}$ at 2.03×10^{-6} , which is also independent of PBH mass and kinetic decoupling parameter. Once again, the constraint on $f_{\rm DM}$ weakens for light black holes and disappears at the same PBH masses as in the left panel, with a fraction $f_{\rm DM}$ equal to 2/3 as could have been guessed. Each panel of Fig. 7 features the same excluded regions observed from a different perspective, depending on whether $f_{\rm BH}$ or $f_{\rm DM}$ is used.

From the upper limits found on $f_{\rm BH}$ (left panel) and $f_{\rm DM}$ (right panel), we conclude that PBHs contribute either all or almost nothing to the astronomical DM, if the partner DM species is made of s-wave annihilating WIMPs. This curious property has been discovered more than 15 years ago by Lacki and Beacom [22], though on more qualitative grounds insofar as no exact solutions to the minispike profiles were known at the time. It has since then been confirmed by several studies [27, 31], which we improve over thanks to our careful analytical understanding, further correcting for the overlooked factor of 2 in WIMP mass necessary to convert DM decay bounds into minispike annihilation bounds. Primordial black holes and such s-wave annihilating particles seem to be incompatible. The former attract the latter to create dense minispikes which should have already been observed. The absence of a γ -ray excess points toward the scarcity or the overabundance of PBHs with respect to WIMPs. Several remarks are now in order to analyze the structure of the forbidden regions.

- In the right parts of the gray domains, the red cuves are horizontal. The upper bounds on $f_{\rm BH}$ (left panel) and $f_{\rm DM}$ (right panel) are insensitive to $M_{\rm BH}$ and $x_{\rm kd}$. In the regime of heavy black holes, the minispike annihilation rate is well approximated by the asymptotic expression (3.33) supplemented by (4.5), hence

$$\Gamma_{\rm BH}^{(9/4)} \propto \langle \sigma_{\rm ann} v \rangle^{1/3} \, \mu^{-4/3} \, m \, f_{\rm DM}^{4/3},$$
(4.12)

with no dependence on $x_{\rm kd}$. We recall that $m = M_{\rm BH}/{\rm M}_{\odot}$ and $\mu = m_{\chi}/1$ TeV. The PBH mass disappears from the inequality (4.11), together with the kinetic decoupling parameter.

– In this high PBH mass regime, the product $f_{\rm BH}\Gamma_{\rm BH}$ scales like $f_{\rm DM}^{4/3}$ when $f_{\rm BH}\simeq 1$, or like $f_{\rm BH}$ when $f_{\rm DM}\simeq 1$. It is no surprise if the upper bounds on the fractions of WIMPs and PBHs are related through

$$f_{\rm DM}^{\rm max} \simeq (f_{\rm BH}^{\rm max})^{3/4} , \qquad (4.13)$$

as can be checked directly with the numerical values given above.

 For light PBHs, relations (3.28) and (4.5) should be used for the minispike annihilation rate, which now scales like

$$\Gamma_{\rm BH}^{(3/2)} \propto \langle \sigma_{\rm ann} v \rangle \,\mu^4 \, x_{\rm kd}^{-3} \, m^3 \, f_{\rm DM}^2 \,.$$
 (4.14)

The upper bound on the product $f_{\rm BH}f_{\rm DM}^2$ is proportional to $x_{\rm kd}^3/M_{\rm BH}^2$. So are the left boundaries of the excluded domains in each panel of Fig. 7. Actually, the upper limits on the fractions $f_{\rm BH}$ and $f_{\rm DM}$ scale respectively like

$$f_{\rm BH}^{\rm max} \propto x_{\rm kd}^3 \, m^{-2} \, ({\rm PBHs})$$
 while $f_{\rm DM}^{\rm max} \propto x_{\rm kd}^{3/2} \, m^{-1} \, ({\rm WIMPs})$. (4.15)

In the left and right panels, we do observe that the left borders of the gray regions drop respectively like $1/M_{\rm BH}^2$ and $1/M_{\rm BH}$. At fixed fraction $f_{\rm BH}$, or $f_{\rm DM}$, the PBH masses at the left boundaries are expected to scale with kinetic decoupling parameter like

$$M_{\rm BH}^{\rm max} \propto x_{\rm kd}^{3/2} \,. \tag{4.16} \label{eq:M_BH}$$

As $x_{\rm kd}$ is increased from 10^2 to 10^3 , the gray regions shift righward in agreement with that relation. But between 10^3 and 10^4 , the observed shift is more important than expected. To explain this discrepancy, we note that the effective number of entropic degrees of freedom of the primordial plasma at kinetic decoupling $h_{\rm kd} \equiv h_{\rm eff}(T_{\rm kd})$ comes actually into play in relation (3.28). Taking it into account yields the new scaling

$$M_{\rm BH}^{\rm max} \propto x_{\rm kd}^{3/2} \, h_{\rm kd}^{-1} \, . \eqno(4.17)$$

As $x_{\rm kd}$ is increased from 10^3 to 10^4 , the kinetic decoupling temperature $T_{\rm kd}$ drops from 1 GeV down to 100 MeV, i.e. below the quark/hadron phase transition, with a sensible reduction of $h_{\rm kd}$ by a factor ~ 4 which cannot be disregarded anymore.

- The transition between light and heavy PBH regimes occurs at the critical mass $M_{\rm T}$ defined in section 3.2. In the configuration under scrutiny, the saturation density $\rho_{\rm sat}$ is 6 orders of magnitude larger than $\rho_{\rm B_1}$ (see table 1). We can apply relations (3.12), (3.13) and (4.4) to derive $M_{\rm T}$, whose positions in both panels of Fig. 7 are indicated by orange dots.
- The left tips of the excluded zones are indicated by blue dots. At these positions, the maximal value of $f_{\rm BH}\Gamma_{\rm BH}$ is barely equal to the right-hand side of inequality (4.11). The former scales like

$$f_{\rm BH}\Gamma_{\rm BH} \simeq f_{\rm BH}\Gamma_{\rm BH}^{(3/2)} \propto f_{\rm BH} (1 - f_{\rm BH})^2 ,$$
 (4.18)

since we are deeply in the low mass regime. The maximum, where the blue dots sit, is reached at $f_{\rm BH}=1/3$, hence $f_{\rm DM}=2/3$, as already mentioned.

4.1.2 Injection of energy in the post-recombination plasma

In the conventional WIMP scenario, thermal DM species still annihilate after recombination and inject energy into the primordial plasma with rate

$$\frac{\mathrm{d}E_{\text{wimps}}^{0}}{\mathrm{d}\mathcal{V}\,\mathrm{d}t}\bigg|_{\text{ini}} = \frac{1}{2}\langle\sigma_{\text{ann}}v\rangle n_{\chi}^{2} \times 2m_{\chi} \times f_{\text{eff}}.$$
(4.19)

The three terms in the right-hand side of this relation respectively refer to the number of annihilations per unit volume and time, the amount of energy released by each annihilation, and the fraction of that energy that is eventually deposited into the plasma. Just after recombination, DM particles are quasi-homogeneously distributed, and their average cosmological number density, at redshift z, is given by

$$n_{\chi}(z) = \frac{\rho_{\rm dm}^0}{m_{\chi}} (1+z)^3. \tag{4.20}$$

The rate of energy injection inside the plasma becomes

$$\frac{\mathrm{d}E_{\text{wimps}}^{0}}{\mathrm{d}\mathcal{V}\,\mathrm{d}t}\bigg|_{\text{ini}} = p_{\text{ann}} \times \left\{\rho_{\text{dm}}^{0}(1+z)^{3}\right\}^{2} \quad \text{where} \quad p_{\text{ann}} \equiv f_{\text{eff}} \frac{\langle \sigma_{\text{ann}} v \rangle}{m_{\chi}}. \tag{4.21}$$

The parameter $p_{\rm ann}$ naturally appears in the previous expression. The energy transferred to the intergalactic medium (IGM) reheats and reionizes it. This modifies the optical depth against Thomson scattering of the photons produced on the last scattering surface, with the consequence of blurring CMB angular anisotropies. The effect is most important at redshift $z_{\rm CMB}$ of order 600 [39], hence the limit⁵ [34]

$$p_{\rm ann} \le p_{\rm ann}^{\rm max} = 3.2 \times 10^{-28} \,\,\mathrm{cm}^3 \,\mathrm{s}^{-1} \,\mathrm{GeV}^{-1}$$
 (4.22)

In our mixed scenario with both a cosmological diffuse component of WIMPs, and very dense minispikes around PBHs, DM annihilation is also associated to energy injection in the IGM with rate

$$\frac{\mathrm{d}E_{\text{tot}}}{\mathrm{d}V\,\mathrm{d}t}\Big|_{\text{inj}} = \frac{\mathrm{d}E_{\text{wimps}}^{f_{\text{BH}}}}{\mathrm{d}V\,\mathrm{d}t}\Big|_{\text{inj}} + \frac{\mathrm{d}E_{\text{spikes}}}{\mathrm{d}V\,\mathrm{d}t}\Big|_{\text{inj}}.$$
(4.23)

Disregarding for the moment the contribution from the diffuse WIMP component, we concentrate on the effect of DM annihilation inside minispikes, whose rate of energy deposition at redshift z may be expressed as

$$\frac{\mathrm{d}E_{\mathrm{spikes}}}{\mathrm{d}\mathcal{V}\mathrm{d}t}\bigg|_{\mathrm{inj}} = \Gamma_{\mathrm{BH}}(z)n_{\mathrm{BH}}(z) \times 2m_{\chi} \times f_{\mathrm{eff}}.$$
(4.24)

The first term in the right-hand side of this relation is the number of annihilations per unit volume and time. The number density $n_{\rm BH}(z)$ of PBHs is given by Eq. (4.6). Requiring that at redshift $z_{\rm CMB}$, where CMB anisotropy data are most sensitive, minispikes do not inject in the IGM more energy than what the Planck limit on $p_{\rm ann}$ allows, we get the condition

$$\frac{\mathrm{d}E_{\mathrm{spikes}}}{\mathrm{d}\mathcal{V}\,\mathrm{d}t}\bigg|_{\mathrm{ini}} \simeq \left.\frac{\mathrm{d}E_{\mathrm{tot}}}{\mathrm{d}\mathcal{V}\,\mathrm{d}t}\right|_{\mathrm{ini}} \leq p_{\mathrm{ann}}^{\mathrm{max}} \times \left\{\rho_{\mathrm{dm}}^{0}(1+z_{\mathrm{CMB}})^{3}\right\}^{2},\tag{4.25}$$

which translates into the bound

$$f_{\rm BH}\Gamma_{\rm BH} \le \left\{\frac{M_{\rm BH}}{2m_{\chi}}\right\} \left\{\frac{1}{\tau_{\rm CMB}^{\rm min}}\right\} \quad \text{where} \quad \frac{1}{\tau_{\rm CMB}^{\rm min}} \equiv \frac{p_{\rm ann}^{\rm max}}{f_{\rm eff}} \rho_{\rm dm}^0 \left(1 + z_{\rm CMB}\right)^3.$$
 (4.26)

 $^{^{5}}$ More precisely, we have borrowed relation (89c) from the Planck analysis of the CMB, and corrected for the misprint 10^{-28} instead of 10^{28} .

Introducing the effective lifetime $\tau_{\rm CMB}^{\rm min}$, the constraint arising from CMB distortions takes the same form as the limit (4.11) derived from the extragalactic γ -ray background. Although not physically motivated, $\tau_{\rm CMB}^{\rm min}$ plays the same role as $\tau_{\rm dm}^{\rm min}$. For particles annihilating into $b\bar{b}$ pairs, the fraction $f_{\rm eff}$ of the energy released and effectively injected in the post-recombination plasma is of order 0.1, hence a value of 1.139×10^{24} s for $\tau_{\rm CMB}^{\rm min}$, independent of m_{χ} . The minispike annihilation rate $\Gamma_{\rm BH}$ must be effectively derived at redshift $z_{\rm CMB}$, and not today.

In Fig. 8, the upper bounds on $f_{\rm BH}$ extracted from the extragalactic γ -ray background and CMB distortions are respectively displayed in the left and right panels. These plots are remarkably similar. The annihilation cross-section $\langle \sigma_{\rm ann} v \rangle$ has been set equal to its thermal value, with $b\bar{b}$ final state. Three different WIMP masses are considered. In each panel, the hatched region corresponds to a 200 GeV particle, with kinetic decoupling parameter 10^4 . This domain, which is excluded by observations, behaves like the gray areas in the left panel of Fig. 7, the topologies of which have already been thoroughly discussed. The hatched area expands leftward to enclose the light-brown vertical band when $x_{\rm kd}$ is decreased down to 10^2 .

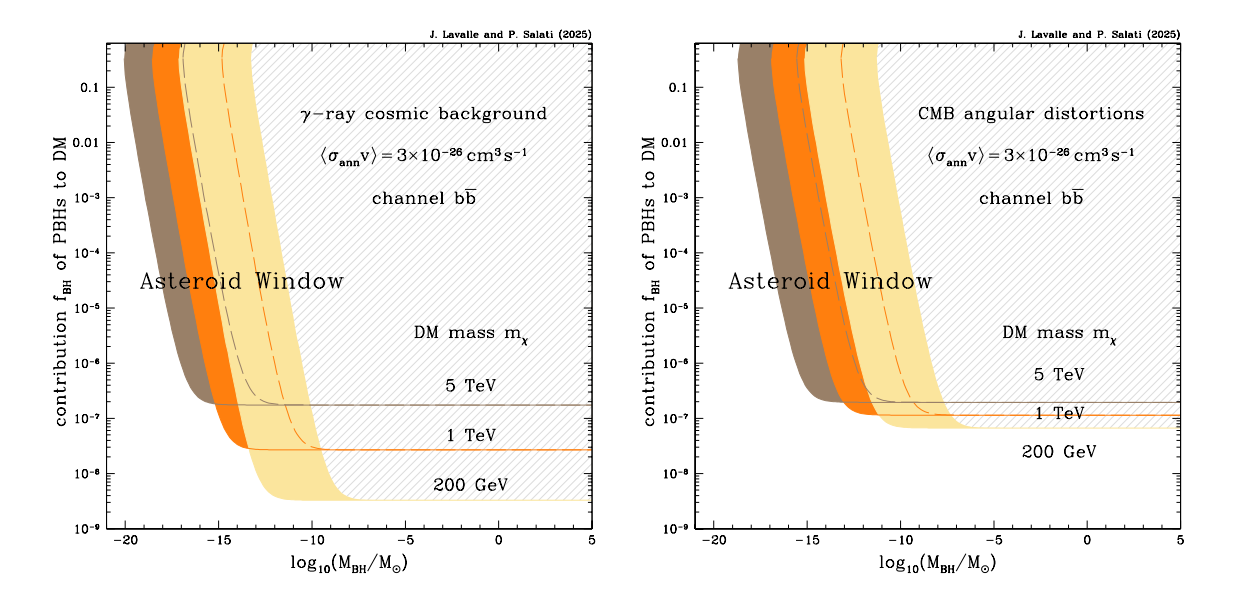


Figure 8. Measurements of the extragalactic γ -ray background [36, 37] and of the angular distortions of the CMB [34] set constrains on the fraction $f_{\rm BH}$ respectively displayed in the left and right panels. Three different WIMP masses have been selected, with thermal annihilation cross-section and $b\bar{b}$ final state. The hatched gray domain, which corresponds to a 200 GeV particle and a kinetic decoupling parameter of 10^4 , is excluded by observations. As $x_{\rm kd}$ is decreased down to 10^2 , this forbidden region expands to encompass the light-brown vertical band. The orange and dark-brown bands correspond respectively to 1 and 5 TeV DM species. All excluded areas encroach on the asteroid window, which is closed over a large range of $f_{\rm BH}$ values.

We observe the same behavior for the 1 and 5 TeV cases, respectively color coded in orange and dark-brown. The lower borders of the excluded zones are delineated by horizontal lines. Acually, for massive black holes, i.e. above the transition mass $M_{\rm T}$, the upper limit on the fraction $f_{\rm BH}$ neither depends on PBH mass nor on $x_{\rm kd}$. It scales like

$$f_{\rm BH}^{\rm max} \propto m_{\chi}^{1/3} \Delta t^{2/3} \left\{ \frac{1}{\tau_{\rm obs}^{\rm min}} \right\},$$
 (4.27)

where $\Delta t = t_{\rm U}(z) - t_{\rm eq}$, with $t_{\rm U}(z)$ and $t_{\rm eq}$ respectively the age of the universe at redshift z and at matter-radiation equality. The lifetime $\tau_{\rm obs}^{\rm min}$ denotes alternatively $\tau_{\rm dm}^{\rm min}$ (extragalactic γ -ray background) or $\tau_{\rm CMB}^{\rm min}$ (CMB distortions). The former lifetime is extracted from Fig. 3 of [37] for the $b\bar{b}$ channel. Taking a decaying DM species twice as massive as our annihilating WIMP, $\tau_{\rm dm}^{\rm min}$ is found respectively equal to 1.49×10^{28} , 3.02×10^{27} and 7.79×10^{26} s at 400 GeV, 2 TeV and 10 TeV. We emphasize that in contrast with the CMB bounds, the extragalactic bounds on the decaying DM lifetime does not exhibit any particular relation with the DM particle mass. So the hierarchy between the bounds at different decaying DM particle mass is purely accidental here, and could have actually been inverted with other choices of mass.

Although the extragalactic γ -ray background has little to do with plasma reionization and CMB distortions, the upper limits which these observations set on $f_{\rm BH}$ are almost identical at 5 TeV, with $f_{\rm BH}^{\rm max} \simeq 2 \times 10^{-7}$. With $\tau_{\rm dm}^{\rm min}$ almost three orders of magnitude larger than $\tau_{\rm CMB}^{\rm min}$, we would have expected γ -rays to be much more constraining than CMB distortions. This difference in lifetime is actually compensated by the increase of the duration Δt from 2.98×10^{13} s at $z_{\rm CMB} = 600$ up to 4.36×10^{17} s today. As the DM mass m_χ is decreased from 5 TeV down to 200 GeV, the constraint on $f_{\rm BH}$ becomes stronger, in agreement with scaling relation (4.27). In the right panel of Fig. 8, $f_{\rm BH}^{\rm max}$ is shifted downward by a factor $5^{1/3} \simeq 1.71$ between adjacent lines. In the left panel, the lower limit $\tau_{\rm dm}^{\rm min}$ comes into play, which varies approximately like m_χ^{-1} in the range of WIMP masses considered. There is this time a shift by a factor $5^{4/3} \sim 8$ between lines.

As the WIMP mass is decreased, the excluded domains in the plane $(M_{\rm BH}, f_{\rm BH})$ are not only shifted downward, as already discussed. They also move righward. The explanation is given in the right panel of Fig. 5, in section 3.2. The long-dashed curve exhibits the effect on the minispike annihilation rate $\Gamma_{\rm BH}$ of reducing m_{χ} from 1 TeV to 10 GeV. The annihilation rate decreases at low PBH masses, while it increases for heavy objects. The long-dashed curve is shifted rightward and upward with respect to the solid line of the fiducial configuration. Decreasing the WIMP mass makes the transition mass $M_{\rm T}$ increase and the colored bands of Fig. 8 move rightward to higher masses.

The colored bands, and associated excluded areas, extend over the asteroid window, i.e. roughly between 10^{-16} and 10^{-11} M $_{\odot}$. Until recently, this region was not constrained by observations [6, 7]. A new analysis [40], based on the effect of asteroid-mass PBHs on the heaviest stars of ultra-faint dwarf galaxies, has set constraints on $f_{\rm BH}$. In Triangulum II, objects around 10^{19} g are excluded at the 2σ (3σ) level from contributing more than $\sim 55\%$ ($\sim 78\%$) to the ambient DM, while the possibility that $f_{\rm BH}$ may reach 1 is excluded at the 3.7σ level. In that context, the bounds featured in Fig. 8 are a useful complement. In our mixed scenario, the fraction of the DM in the form of PBHs is much more severely constrained than in [40], with an upper bound as low as a few billionths in the case of a 200 GeV particle. However, as pointed out by Lacki and Beacom [22], nothing prevents PBHs from constituting all the astronomical DM. In the plots of Fig. 8, a very narrow strip close to $f_{\rm BH} \simeq 1$ is still allowed.

As a final point, we would like to examine how the CMB bounds are modified when the diffuse component of WIMPs is now taken into account. It contributes an energy injection

$$\frac{\mathrm{d}E_{\text{wimps}}^{f_{\text{BH}}}}{\mathrm{d}\mathcal{V}\mathrm{d}t}\bigg|_{\text{inj}} = f_{\text{DM}}^2 \frac{\mathrm{d}E_{\text{wimps}}^0}{\mathrm{d}\mathcal{V}\mathrm{d}t}\bigg|_{\text{inj}} \equiv \left(f_{\text{DM}}^2 p_{\text{ann}}\right) \times \left\{\rho_{\text{dm}}^0 (1+z)^3\right\}^2.$$
(4.28)

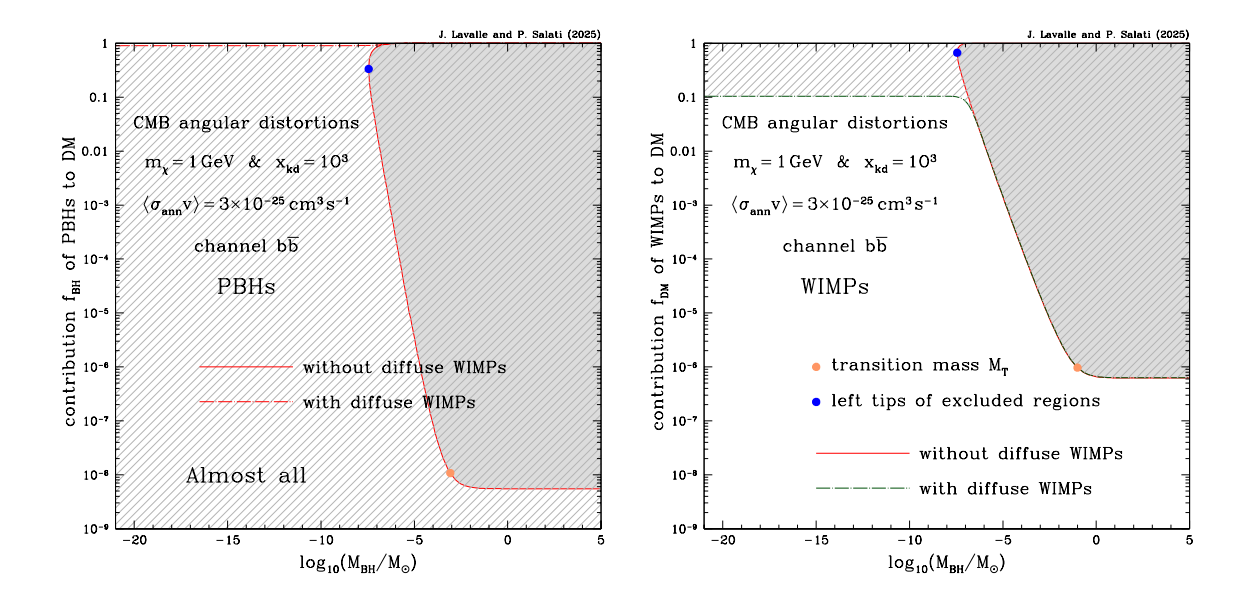


Figure 9. Same as in Fig. 7 with constraints from CMB distortions instead of extragalactic γ -ray background. For simplicity, one value only has been assumed for the kinetic decoupling parameter $x_{\rm kd}$. The contributions of PBHs and WIMPs to the DM are respectively displayed in the left and right panels. Considering energy injection in the post-recombination plasma induced solely by minispike annihilation yields the light-gray regions. These excluded domains expand to encompass the hatched areas when the contribution from the diffuse WIMPs is added. Although no bound applies in the former case below PBH mass of 3.6×10^{-8} M_☉, featured by the blue dots, the diffuse WIMP component is constrained to contribute less than 10% to the DM once it is included in the plasma reheating and reionization. The fraction $f_{\rm BH}$ is constrained to be at least larger than 90%. For a WIMP of 1 TeV though, the hatched region would be completely removed.

The constraint on the contribution from minispikes becomes

$$\frac{\mathrm{d}E_{\text{spikes}}}{\mathrm{d}\mathcal{V}\mathrm{d}t}\Big|_{\text{inj}} = \frac{\mathrm{d}E_{\text{tot}}}{\mathrm{d}\mathcal{V}\mathrm{d}t}\Big|_{\text{inj}} - \frac{\mathrm{d}E_{\text{wimps}}^{f_{\text{BH}}}}{\mathrm{d}\mathcal{V}\mathrm{d}t}\Big|_{\text{inj}} \le \left(p_{\text{ann}}^{\text{max}} - f_{\text{DM}}^{2} p_{\text{ann}}\right) \times \left\{\rho_{\text{dm}}^{0} (1 + z_{\text{CMB}})^{3}\right\}^{2}, \quad (4.29)$$

which eventually translates into

$$f_{\rm BH}\Gamma_{\rm BH} \le \left\{\frac{M_{\rm BH}}{2m_{\chi}}\right\} \left\{\frac{1}{\tau_{\rm CMB}^{\rm min}}\right\} \left\{1 - f_{\rm DM}^2 \left(\frac{p_{\rm ann}}{p_{\rm ann}^{\rm max}}\right)\right\}.$$
 (4.30)

As long as the ratio $p_{\rm an}/p_{\rm ann}^{\rm max}$ is small compared to 1, the bound on $f_{\rm BH}$ does not change much. In Fig. 8 for instance, $p_{\rm ann}$ is equal to $3\times 10^{-30}~{\rm cm^3\,s^{-1}\,GeV^{-1}}$ for a 1 TeV species, to be compared to a CMB limit $p_{\rm ann}^{\rm max}$ two orders of magnitude larger. Including the diffuse WIMP component strengthens the constraint on the fraction of PBHs. The larger $p_{\rm ann}$, the lower the upper bound $f_{\rm BH}^{\rm max}$. If $p_{\rm ann}$ turns out to be larger than the limit $p_{\rm ann}^{\rm max}$, a small admixture of PBHs is completely ruled out insofar as the astronomical DM would be essentially made of diffuse WIMPs, a possibility forbidden by CMB data.

On the other hand, PBHs evade observational constraints when their contribution to DM is close to 1. Changing perspective, we can examine whether or not WIMPs are allowed even though $p_{\rm ann}$ is larger than $p_{\rm ann}^{\rm max}$. Such a possibility is excluded in the pure WIMP scenario. But the presence of PBHs could alleviate CMB constraints. In Fig. 9, the case of a

1 GeV DM species is featured, with annihilation cross-section $\langle \sigma_{\rm ann} v \rangle$ an order of magnitude larger than the thermal value. With such parameters, and assuming that $f_{\rm eff}$ is still equal to 0.1, $p_{\rm ann}$ reaches 3×10^{-26} cm³ s⁻¹ GeV⁻¹, i.e. two orders of magnitude larger than the CMB limit.

The fractions $f_{\rm BH}$ and $f_{\rm DM}$ are respectively presented in the left and right panels. The gray regions are derived from the conservative limit (4.26). These domains are similar to the excluded areas of Fig. 7, although the latter was drawn assuming a 1 TeV species, and translate now the CMB data. No constraint applies below a PBH mass of 3.6×10^{-8} M_{\odot}, featured by the blue dots. On the contrary, the hatched regions are obtained by taking into account the diffuse WIMP contribution and by applying the more restrictive condition (4.30). PBHs are essentially excluded, apart from a very small fringe located in the upper part of the left panel. The right panel features the WIMP fraction $f_{\rm DM}$, which is now constrained to be less than 10% even for light black holes. In this region, PBHs must contribute more than 90% to the DM. While minispike annihilation provides most of the energy injected into the post-recombination plasma for PBH masses above 3.6×10^{-8} M_{\odot}, the diffuse WIMP component takes over below that value. Both regimes clearly show up in the structure of the hatched region of the right panel. Note finally that, had we assumed a WIMP mass of 1 TeV instead of 1 GeV, the hatched area would have completely disappeared since the diffuse contribution of such heavy particles is currently not constrained by CMB data.

4.2 Bounds on WIMP properties

Changing perspective, we assume now that a population of primordial black holes has been discovered, contributing a fraction $f_{\rm BH}$ to the astronomical DM. Searches for such objects are underway, and it is conceivable that GW observatories will find them in the near future, should they exist. Such a discovery would also be of great interest for thermal DM species. Even a minute admixture of PBHs to DM implies stringent limits on the annihilation cross-section of WIMPs, sometimes orders of magnitude below the thermal value of $3 \times 10^{-26} \ {\rm cm}^3 \ {\rm s}^{-1}$.

4.2.1 Structure of the excluded region in the $(m_{\gamma}, \langle \sigma_{\rm ann} v \rangle)$ plane

From now on, we conservatively concentrate on the limits set by the contribution of minispikes alone to either the cosmological γ -ray background, or the injection of energy in the post-recombination plasma. These constraints are respectively described by relations (4.11) and (4.26). They can be summarized by the inequality

$$f_{\rm BH}\Gamma_{\rm BH} \le \left\{\frac{M_{\rm BH}}{2m_{\chi}}\right\} \left\{\frac{1}{\tau_{\rm obs}^{\rm min}}\right\},$$
 (4.31)

with $\tau_{\rm obs}^{\rm min}$ being either equal to $\tau_{\rm dm}^{\rm min}$ or $\tau_{\rm CMB}^{\rm min}$. For pedagogical purposes, we choose the CMB constraints. They are the least stringent, with $\tau_{\rm CMB}^{\rm min}$ of order 10^{24} s while $\tau_{\rm dm}^{\rm min}$ lies between 10^{26} and 10^{28} s. Furthermore, as long as $f_{\rm eff}$ does not depend on WIMP mass, the effective lifetime $\tau_{\rm CMB}^{\rm min}$ is constant. This will make the discussion clearer.

To understand how relation (4.31) constrains the annihilation cross-section, we have plotted in Fig. 10 the minispike annihilation rate $\Gamma_{\rm BH}$ as a function of $\langle \sigma_{\rm ann} v \rangle$. In the left panel, the WIMP properties are specified while the PBH mass is varied. All curves have a maximum and exhibit a power law behavior, with slope +1 as $\Gamma_{\rm BH}$ increases with $\langle \sigma_{\rm ann} v \rangle$, and slope -1 as it decreases. We also notice that above $10^{-13}~{\rm M}_{\odot}$, a portion with slope 1/3

appears. The dotted short-dashed red and solid orange curves clearly flatten before reaching their maxima

The explanation of how $\Gamma_{\rm BH}$ evolves with $\langle \sigma_{\rm ann} v \rangle$ has been partially given in section 3.3. The minispike annihilation rate follows three distinct regimes depending on how the PBH mass $M_{\rm BH}$, the critical value M_1 and the transition mass $M_{\rm T}$ compare to each other. Once the WIMP mass m_{χ} and kinetic decoupling parameter $x_{\rm kd}$ are defined, as is the case in the left panel of Fig. 10, the phase diagram of Fig. 1 is completely determined. So is the critical mass M_1 , which we find here equal to $1.097 \times 10^{-13} \ {\rm M}_{\odot}$, a value corresponding to the long-dashed magenta curve. We also should keep in mind that the saturation density $\rho_{\rm sat}$ and the corresponding transition mass $M_{\rm T}$ decrease as $\langle \sigma_{\rm ann} v \rangle$ increases, while all the other parameters are kept fixed. Two cases can essentially be distinguished.

1. $M_1 \leq M_{\rm BH}$ – The annihilation rate is well approximated by $\Gamma_{\rm BH}^{(3/2)}$ and its definition (3.28) as long as the transition mass $M_{\rm T}$ exceeds $M_{\rm BH}$, i.e. for small values of the annihilation cross-section. In this regime, $\Gamma_{\rm BH}$ scales like $\langle \sigma_{\rm ann} v \rangle$, hence the slope +1. A transition is expected when $M_{\rm T}$ and $M_{\rm BH}$ become equal. In the case of the dotted short-dashed red curve, this takes place when $M_{\rm T}$ reaches down $10^{-9}~{\rm M}_{\odot}$, at the reduced annihilation cross-section of 3.16×10^{-12} . A close inspection of the plot indicates that the transition is very smooth and starts already an order of magnitude below that value.

Then, for $M_1 \leq M_{\rm T} \leq M_{\rm BH}$, the annihilation rate is given by $\Gamma_{\rm BH}^{(9/4)}$ and relation (3.33). In this intermediate regime, $\Gamma_{\rm BH}$ scales like $\langle \sigma_{\rm ann} v \rangle^{1/3}$, hence the slope 1/3 which the dotted short-dashed red curve of the left panel clearly exhibits. The maximal annihilation rate is expected to be reached when the saturation density $\rho_{\rm sat}$ becomes equal to $\rho_{\rm B_1}$, i.e. when $M_{\rm T}$ has decreased down to $M_{\rm I}$. This occurs when the annihilation cross-section is equal to $\langle \sigma_{\rm ann} v \rangle_{\rm crit}$ as defined by relation (3.37) that yields in our case a value of 4.4×10^{-16} cm³ s⁻¹ independent of PBH mass. Once again, the maximum is very smooth and is reached numerically slightly below $\langle \sigma_{\rm ann} v \rangle_{\rm crit}$.

Finally, for $M_{\rm T} \leq M_1$, the approximation $\Gamma_{\rm BH}^{(0)}$ as defined by (3.36) comes into play, hence a minispike annihilation rate decreasing like $1/\langle \sigma_{\rm ann} v \rangle$ and the slope -1 which the curves exhibit when the annihilation cross-section is large.

2. $M_{\rm BH} \leq M_1$ – Once again, for $M_{\rm T}$ exceeding $M_{\rm BH}$, $\Gamma_{\rm BH}^{(3/2)}$ is a good approximation for the annihilation rate. In the left panel of Fig. 10, the dotted short-dashed blue and solid purple curves do feature a power law increase with slope +1 when $\langle \sigma_{\rm ann} v \rangle$ is small. This regime extends up to the critical cross-section $\langle \sigma_{\rm ann} v \rangle_{\rm crit}$ as defined now by the more involved expression (3.38). At 10^{-15} and 10^{-17} M_{\odot}, the maxima are respectively expected at the reduced cross-sections of 10^2 and 10^4 , in good agreement with the numerical results of Fig. 10.

Finally, for $M_{\rm T}$ smaller than $M_{\rm BH}$, $\Gamma_{\rm BH}^{(0)}$ and its expression (3.36) can be used. The annihilation rate $\Gamma_{\rm BH}$ is inversely proportional to the annihilation cross-section, hence the slope -1 which the curves exhibit above $\langle \sigma_{\rm ann} v \rangle_{\rm crit}$.

To summarize, the minispike annihilation rate increases with slope +1 as long as the annihilation cross-section is smaller than the critical value $\langle \sigma_{\rm ann} v \rangle_{\rm crit}$. Above that value, $\Gamma_{\rm BH}$ decreases with slope -1. If $M_{\rm BH}$ is larger than the critical mass M_1 , $\langle \sigma_{\rm ann} v \rangle_{\rm crit}$ is defined

by (3.37) and a regime with slope 1/3 appears before the maximum is reached. In the opposite situation, there is no such regime, and $\langle \sigma_{\rm ann} v \rangle_{\rm crit}$ is defined by (3.38).

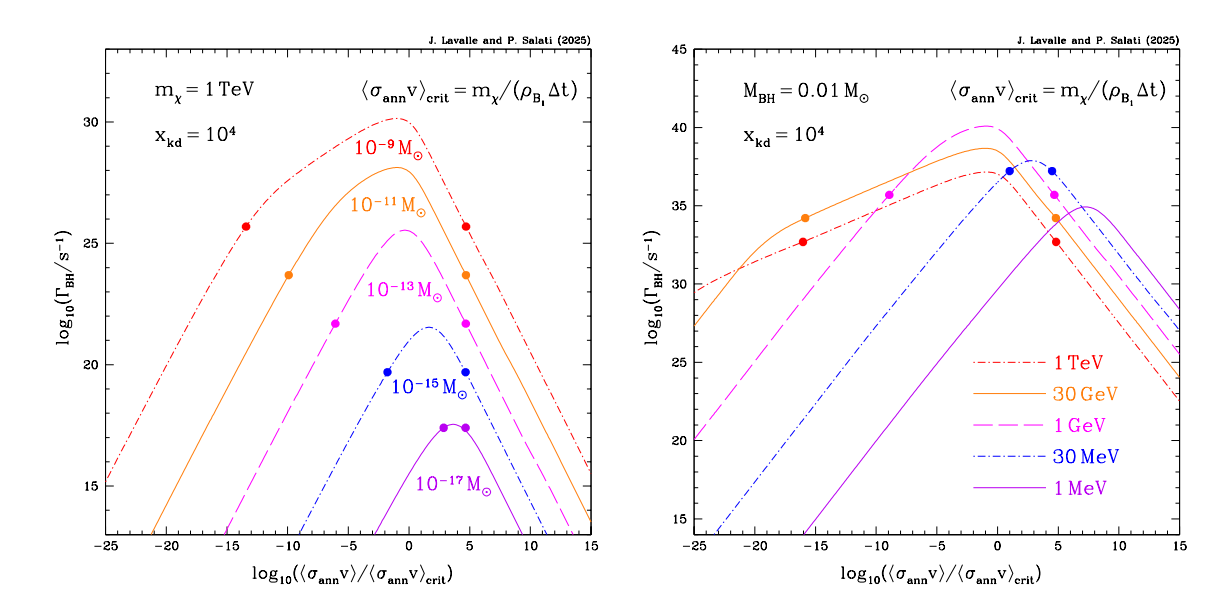


Figure 10. The minispike annihilation rate $\Gamma_{\rm BH}$ is plotted as a function of the WIMP annihilation cross-section $\langle \sigma_{\rm ann} v \rangle$. In the **left panel**, the properties of the thermal DM particle are specified, with a mass m_{χ} of 1 TeV and a kinetic decoupling parameter $x_{\rm kd}$ of 10⁴. The PBH mass is varied from 10^{-17} to 10^{-9} M_☉. A power law behavior with slope 1/3 appears for $M_{\rm BH}$ larger than 10^{-13} M_☉, a value close to the critical mass M_1 . In the **right panel**, the PBH mass is set equal to 0.01 M_☉ while the WIMP mass m_{χ} is increased from 1 MeV up to 1 TeV. The slope 1/3 also appears for the heaviest particles. For each curve, the colored dots indicate the critical value of $\Gamma_{\rm BH}$ above which the constraint (4.26) is violated, with $f_{\rm eff}$ and $f_{\rm BH}$ respectively set equal to 0.1 and 10^{-5} . In the case of the solid purple curve of the **right panel**, this condition is always met.

In the right panel of Fig. 10, the PBH mass is set equal to 0.01 M_{\odot} , while the WIMP mass m_{χ} is decreased from 1 TeV down to 1 MeV. We observe the same trend as in the left panel, with the slope 1/3 appearing for the heaviest DM species. At fixed kinetic decoupling parameter $x_{\rm kd}$, $T_{\rm kd}$ is proportional to m_{χ} . In the phase diagram of Fig. 1, decreasing the WIMP mass translates into shifting upward the dotted short-dashed red line (radius of influence \tilde{r}_{kd} at kinetic decoupling), moving it closer to the solid red line (radius of influence \tilde{r}_{eq} at matter-radiation equality). The intersection between the former line and the dotted long-dashed gray vertical also moves upward. So do points A and B₂, hence an increase of M_2 and an even larger increase of M_1 insofar as the radial infall domain with slope 9/4 has shrinked. As m_{χ} decreases, M_1 increases. For heavy DM particles, as long as M_1 is smaller than $M_{\rm BH}$, the curves exhibit a maximum when $\rho_{\rm sat}$ is equal to $\rho_{\rm B_1}$. They also contain a portion with slope 1/3, as is particularly clear in the 30 GeV and 1 TeV cases. At 1 GeV, the critical mass M_1 is still equal to 3.7×10^{-4} M_{\odot}, to be compared to a value of 16.7 M_{\odot} at 30 MeV. The transition occurs in between. The curves corresponding to a WIMP mass of 1 and 30 MeV exhibit the same kind of behavior as the smallest PBH masses of the left panel. The maximum is reached for a saturation density $\rho_{\rm sat}$ smaller than $\rho_{\rm B_1}$, i.e. for a reduced cross-section larger than 1. The regime with slope 1/3 has also disappeared.

In both panels of Fig. 10, the colored dots indicate the critical value of $\Gamma_{\rm BH}$ over which

constraint (4.31) is broken. For clarity, we have used the CMB bound (4.26) and set $f_{\rm eff}$ and $f_{\rm BH}$ respectively equal to 0.1 and 10^{-5} . The solid purple curve of the right panel does not have any dot. Whatever the annihilation cross-section, a 1 MeV DM species fulfills the CMB observational constraint on minispikes (and not on the diffuse contribution which is strongly constrained in this light mass range). This is not the case for the other configurations. On each curve of these, the portion lying between dots does not meet condition (4.26) and is excluded. The left and right dots respectively yield the upper and lower limits $\langle \sigma_{\rm ann} v \rangle_{\rm L}$ and $\langle \sigma_{\rm ann} v \rangle_{\rm R}$ set by CMB measurements on WIMP annihilation cross-section. The range extending between these values violates observations, hence the existence of an excluded domain in the $(m_\chi, \langle \sigma_{\rm ann} v \rangle)$ plane.

At fixed $f_{\rm BH}$ and $au_{\rm obs}^{\rm min}$, the minispike annihilation rate, at the dots, scales like

$$\Gamma_{\rm BH} \propto \frac{M_{\rm BH}}{m_{\gamma}} \,.$$
(4.32)

This scaling clearly appears in Fig. 10. In the left panel, dots shift downward by two orders of magnitude each time the PBH mass is decreased while in the right panel, they shift upward by a factor ~ 30 each time the WIMP mass is decreased. We also notice the peculiar alignment of the right dots. These are located on the decreasing parts of curves. In this regime, $\Gamma_{\rm BH}$ is given by relation (3.36) which, combined with condition (4.31), yields the scaling

$$\langle \sigma_{\rm ann} v \rangle_{\rm R} \propto f_{\rm BH} \times m_{\chi} \times \Delta t^{-2} \times \tau_{\rm obs}^{\rm min}$$
 (upper boundary). (4.33)

In the left panel, the WIMP mass is set equal to 1 TeV and does not vary. In the right panel, the annihilation cross-section is expressed in units of the critical value (3.37). The WIMP mass cancels out in the ratio $\langle \sigma_{\rm ann} v \rangle_{\rm R} / \langle \sigma_{\rm ann} v \rangle_{\rm crit}$, hence the vertical alignment which we also observe in that panel.

Inspired by our analysis of Fig. 10, we are ready to construct in the $(m_\chi, \langle \sigma_{\rm ann} v \rangle)$ plane the region excluded by Planck observations [34] of the CMB and determination of $p_{\rm ann}^{\rm max}$. We start scanning over WIMP mass. For each selected m_χ , we first check if the maximal minispike annihilation rate, i.e. the value of $\Gamma_{\rm BH}$ taken at $\langle \sigma_{\rm ann} v \rangle_{\rm crit}$, fulfills condition (4.26). If it does not, we use dichotomy to derive the upper and lower bounds $\langle \sigma_{\rm ann} v \rangle_{\rm L}$ and $\langle \sigma_{\rm ann} v \rangle_{\rm R}$ on the annihilation cross-section. Values of $\langle \sigma_{\rm ann} v \rangle$ lying in between are excluded. In Fig. 11, such a construction is presented for a PBH mass of 0.01 ${\rm M}_{\odot}$ and three different values of the fraction $f_{\rm BH}$. Each of these corresponds to a specific shade of gray and contour type, as indicated. The light-gray domain, drawn for a PBH fraction of 10^{-5} , is most extended. We have put the colored dots of the right panel of Fig. 10 in the $(m_\chi, \langle \sigma_{\rm ann} v \rangle)$ diagram. They all lie along the solid red contour which delineates that forbidden area, as they should. We observe that the smaller $f_{\rm BH}$, the less extended the excluded zones. Each contour clearly exhibits three portions over which $\Gamma_{\rm BH}$ has a specific behavior.

- The upper segment corresponds to the lower bound $\langle \sigma_{\rm ann} v \rangle_{\rm R}$, and to the declining parts of the curves in Fig. 10. The annihilation rate is well described by the asymptotic expression (3.36) which, combined with the generic constraint (4.31), yields the scaling (4.33). The upper borders of the forbidden regions increase with m_{χ} with slope +1, and extend upward by an order of magnitude each time the fraction $f_{\rm BH}$ is increased.
- In the lower-left section of contours, the WIMP mass is small. Inspired by the right panel of Fig. 10, we guess that the annihilation rate behaves asymptotically according

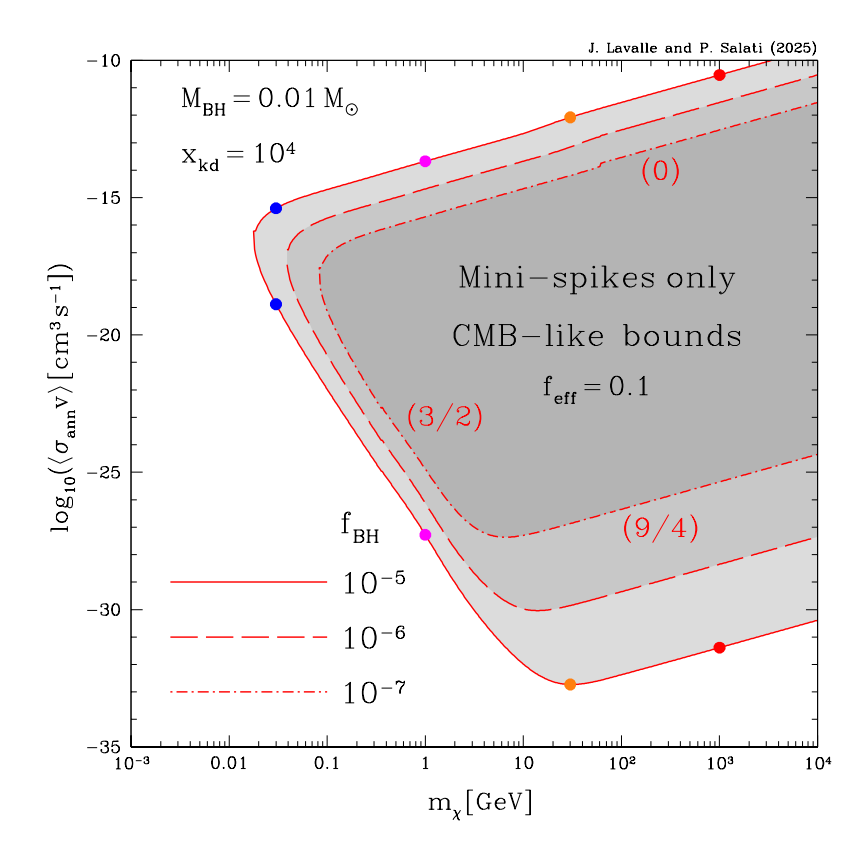


Figure 11. In this pedagogical plot, the bounds set by cosmological observations on DM annihilation inside minispikes only are featured in the $(m_\chi, \langle \sigma_{\rm ann} v \rangle)$ plane. The CMB constraint (4.26), based on Planck determination of $p_{\rm ann}^{\rm max}$ [34], has been chosen. The fraction $f_{\rm eff}$ has been set equal to 0.1 for simplicity. We assume the existence of a population of PBHs with mass 0.01 M_☉, contributing a fraction $f_{\rm BH}$ to the astronomical DM. The various shades of gray and contour types correspond to different values of this contribution, as indicated. The colored dots extracted from the right panel of Fig. 10 have been put on this diagram. They lie, as they should, on the boundary of the light-gray domain. We clearly distinguish, in the structure of the excluded regions, three different regimes for the minispike annihilation rate. The lower-right, lower-left and upper edges correspond respectively to the asymptotic behaviors (3.33), (3.28) and (3.36) of Γ_{BH}.

to expression (3.28) which, once combined with the generic bound (4.31), leads to the scaling

$$\langle \sigma_{\rm ann} v \rangle_{\rm L} \propto f_{\rm BH}^{-1} M_{\rm BH}^{-2} \times m_{\chi}^{-5} x_{\rm kd}^3 \times \frac{1}{\tau_{\rm obs}^{\rm min}}$$
 (lower-left boundary). (4.34)

In the plot, we do observe the contours dropping with m_{χ} while following a characteristic slope of -5. They also shift downward by an order of magnitude each time $f_{\rm BH}$ is increased.

For a PBH fraction of 10^{-5} , we remark that the lower-left boundary extends approximately from the left tip of the light-gray area at 18 MeV up to the orange dot at 30 GeV. At the latter location, the transition mass $M_{\rm T}$ associated to the upper bound $\langle \sigma_{\rm ann} v \rangle_{\rm L}$ is equal to 1.7×10^{-3} , well below $M_{\rm BH}{}^6$. Above 30 GeV, we enter in a new regime.

⁶The transition between the lower-left and lower-right boundaries can be more accurately determined by

- Along the lower-right edges of the exclusion regions, the WIMP mass is large. We can approximate $\Gamma_{\rm BH}$ by its asymptotic expression (3.33). Actually, the transition mass $M_{\rm T}$ corresponding to the upper limit $\langle \sigma_{\rm ann} v \rangle_{\rm L}$ is well below $M_{\rm BH}$. Combining relation (3.33) with the generic cosmological constraint (4.31) yields the scaling

$$\langle \sigma_{\rm ann} v \rangle_{\rm L} \propto f_{\rm BH}^{-3} \times m_{\chi} \times \Delta t^2 \times \left\{ \frac{1}{\tau_{\rm obs}^{\rm min}} \right\}^3$$
 (lower-right boundary). (4.35)

The lower-right and upper frontiers of the excluded regions are parallel, moving upward as m_{χ} increases with slope +1. The forbidden domains shift downward by three orders of magnitude each time $f_{\rm BH}$ is increased. The bound $\langle \sigma_{\rm ann} v \rangle_{\rm L}$ is also very sensitive to the lower limit $\tau_{\rm obs}^{\rm min}$. We expect the γ -ray constraints to be significantly more stringent than those extracted from the CMB. This conclusion should be nevertheless mitigated by the much larger cosmic duration Δt in the former case.

4.2.2 Constraints on $\langle \sigma_{ann} v \rangle$ from CMB angular distortions

The left panel of Fig. 12 is an enlargement of Fig. 11 and focuses on the upper bound $\langle \sigma_{\rm ann} v \rangle_{\rm L}$ set by CMB observations on the annihilation cross-section between 100 MeV and 10 TeV. In this panel, DM annihilation taking place only inside minispikes is considered, so that we have implemented constraint (4.26). The short-dashed magenta line corresponds to the thermal value $\langle \sigma_{\rm ann} v \rangle_{\rm th}$ required in the canonical scenario to get the observed DM abundance from WIMP freeze-out. We notice that even a small admixture of PBHs to the overall DM budget induces stringent constraints on $\langle \sigma_{\rm ann} v \rangle$. For a fraction $f_{\rm BH}$ of 10^{-6} , for instance, the upper bound stands more than four orders of magnitude below the thermal value at 10 GeV. The CMB constraints weaken considerably though in the sub-GeV region where essentially minispikes do not provide any leverage on WIMPs.

The gap left open at small masses can be closed if the contribution of the diffuse population of DM species is now taken into account, together with minispikes. In the right panel, constraint (4.30) has been implemented. The dotted long-dashed purple line is the upper limit set by Planck [34] on $\langle \sigma_{\rm ann} v \rangle$ in the conventional WIMP scenario, i.e. without black holes, and is trivially expressed as

$$\langle \sigma_{\rm ann} v \rangle \le \frac{p_{\rm ann}^{\rm max}}{f_{\rm eff}} m_{\chi} \,.$$
 (4.36)

A comparison between the left and right panels shows that the upper bound $\langle \sigma_{\rm ann} v \rangle_{\rm L}$ is either dominated by minispikes, or by the diffuse WIMP population, the most stringent constraint prevailing over the other. Relation (4.36) provides a conservative upper limit which $\langle \sigma_{\rm ann} v \rangle$ cannot exceed. Without minispikes, thermal DM species, at least in their simplest incarnation with s-wave annihilation, are ruled out below 10 GeV but allowed above.

This possibility would be further jeopardized if a population of light black holes were discovered in the near future and its abundance $f_{\rm BH}$ measured. As showed in the right panel, DM particles with mass below 700 GeV are already excluded by a PBH fraction $f_{\rm BH}$ as small as 10^{-7} . We can derive a lower limit on the WIMP mass m_{χ} by requiring that the upper bound $\langle \sigma_{\rm ann} v \rangle_{\rm L}$ should exceed the thermal value $\langle \sigma_{\rm ann} v \rangle_{\rm th}$. Using the scaling (4.35), we get

$$m_{\chi} \ge 7 \times 10^5 \text{ GeV} \left\{ \frac{f_{\text{BH}}}{10^{-6}} \right\}^3 \left\{ \frac{f_{\text{eff}}}{0.1} \right\}^3.$$
 (4.37)

finding the intersection of the corresponding tangent lines. A closer inspection shows that the transition takes place actually at 13 GeV, a value at which the transition mass $M_{\rm T}$ is equal to $1.1 \times 10^{-2} {\rm M}_{\odot}$.

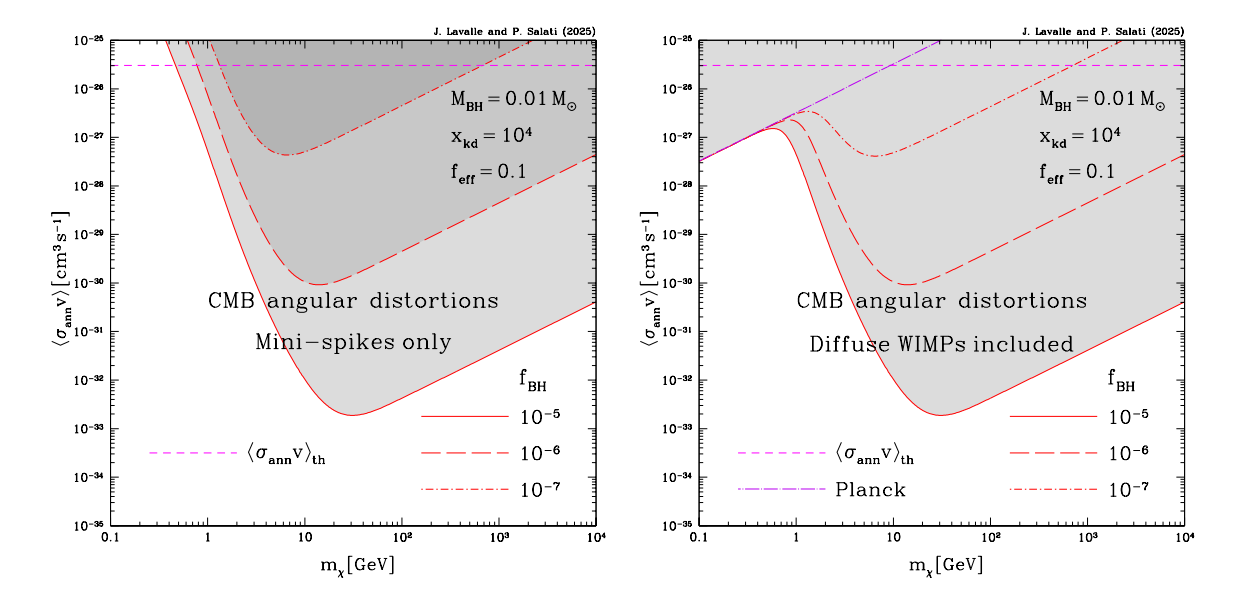


Figure 12. Planck observations of the CMB angular distortions constrain the amount of energy that is released by DM annihilations and eventually injected in the intergalactic medium after recombination [34]. In these plots, a population of PBHs with mass 0.01 M_{\odot} is assumed, which contributes a fraction $f_{\rm BH}$ to the astronomical DM. The CMB limit on $p_{\rm ann}^{\rm max}$ translates into an upper bound $\langle \sigma_{\rm ann} v \rangle_{\rm L}$ on the annihilation cross-section. In the left panel, the exclusive contribution of minispikes is considered, while the diffuse WIMP component is also taken into account in the right panel. The short-dashed magenta horizontal line indicates the thermal value of $\langle \sigma_{\rm ann} v \rangle$. The dotted long-dashed purple line is the upper limit set by Planck in the conventional WIMP scenario without primordial black holes.

This constraint is remarkably stringent and points toward heavy DM candidates.

The efficiency factor $f_{\rm eff}$ has been heuristically set equal to 0.1 insofar as our study aims primarily at clearing the field and paving the road for a forthcoming detailed investigation. We intend to investigate the CMB constrains on $\langle \sigma_{\rm ann} v \rangle$ using the public code CLASS (work in preparation). This would allow to get the correct variations of $f_{\rm eff}$ with cosmic time as well as its dependence on WIMP mass and annihilation channel. The second benefit would be to follow in time the actual energy deposition in the post-recombination plasma. We have recycled here limits derived in the conventional scenario of a pure diffuse WIMP component, for which the rate of energy injection scales like $(1+z)^6$ and peaks at $z_{\rm CMB}$ of order 600. In the case of minispikes, this rate scales either like $(1+z)^3$ or $(1+z)^4$ depending on whether the annihilation rate $\Gamma_{\rm BH}$ is given by relation (3.28) or (3.33). The redshift at which most of the energy deposition occurs should be different from the value of 600 assumed here. We nevertheless expect the results derived using CLASS to be qualitatively similar to those presented in this article.

4.2.3 Constraints on $\langle \sigma_{\rm ann} v \rangle$ from cosmological γ -ray background

From their analysis of the cosmological γ -ray background, Ando and Ishiwata have derived bounds on decaying DM particles [37] which we have translated, in the framework of our mixed DM model, into condition (4.11). As our focus is here on the WIMP annihilation cross-section, we apply the same method as in the previous sections, and implement that constraint to derive the upper bound $\langle \sigma_{\rm ann} v \rangle_{\rm L}$.

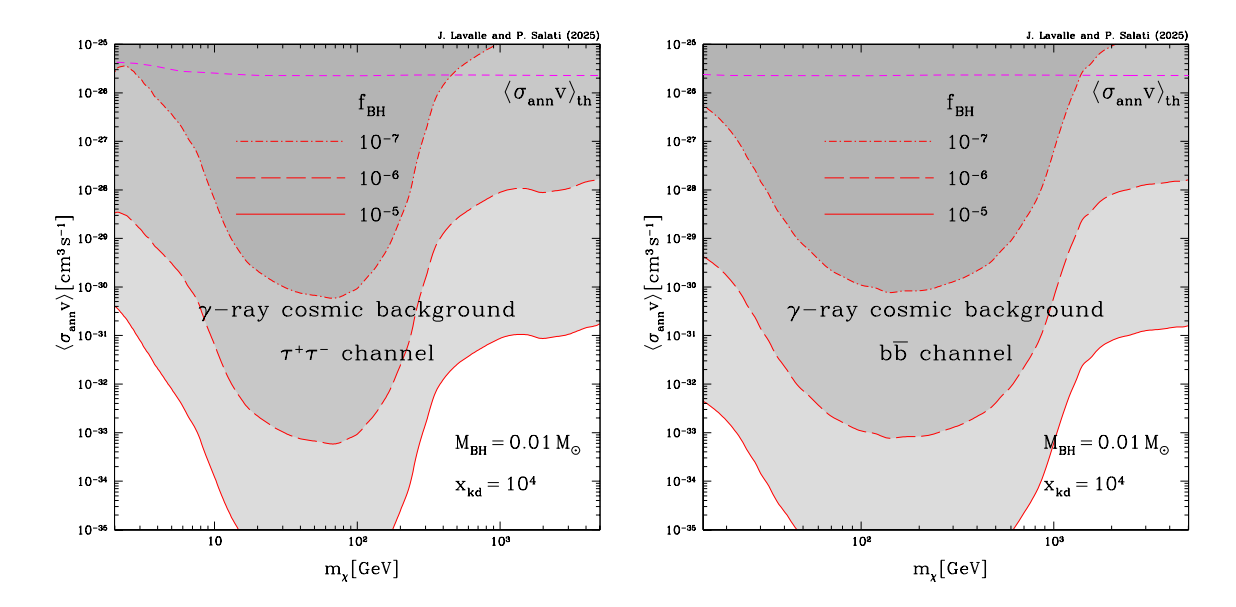


Figure 13. The upper bound on the annihilation cross-section set by the cosmological γ -ray background is plotted as a function of WIMP mass. The $\tau^+\tau^-$ and $b\bar{b}$ annihilation channels are respectively displayed in the left and right panels. A population of 0.01 M $_{\odot}$ primordial black holes is assumed, which contributes a fraction $f_{\rm BH}$ to the astronomical DM. The γ -ray constraint (4.11) has been implemented and translated into the excluded regions shaded in gray. Three values of $f_{\rm BH}$ are presented, each corresponding to a particular shade of gray and contour type as indicated. The short-dashed magenta horizontal line refers to the thermal value of the annihilation cross-section. The constraints on $\langle \sigma_{\rm ann} v \rangle$ are even more stringent than those derived from the CMB.

Should the lower limit $\tau_{\rm dm}^{\rm min}$ on the lifetime of decaying DM species had been constant, the exclusion plots of Figs. 11 and 13 would have been identical, up to a rescaling of the gray shaded regions. However, as is clear in Fig. 3 of Ando and Ishiwata analysis [37], the lifetime $\tau_{\rm dm}^{\rm min}$ varies strongly with m_χ , evolving between 10^{26} and 10^{28} s. As a consequence, the contours of the excluded domains of Fig. 13 exhibit festoon-like features. They also extend very deep downward. For the $\tau^+\tau^-$ annihilation channel, for instance, the most stringent upper limit on $\langle \sigma_{\rm ann} v \rangle$ is reached at 70 GeV and is equal to 6×10^{-34} cm³ s⁻¹ for a PBH fraction of a millionth. For the $b\bar{b}$ channel, we get 8×10^{-34} cm³ s⁻¹ at 150 GeV. We observe that the γ -ray bounds are even more stringent than those derived from the CMB. However, they are limited to WIMP masses below 5 TeV insofar as Ando and Ishiwata have considered DM decaying species lighter than 10 TeV. In that range, s-wave annihilating DM particles are forbidden, unless $f_{\rm BH}$ does not exceed 3.5 billionths.

To summarize our investigation of the CMB and γ -ray bounds on $\langle \sigma_{\rm ann} v \rangle$, the message which we would like to convey at this stage is the potentially strong perturbation which a tiny admixture of primordial black holes would bring on the phenomenology of thermal DM species. The simplest DM candidate, whose annihilation proceeds through s-wave, would be essentially ruled out if there are PBHs in the asteroid mass window or heavier, representing a DM fraction typically larger than a millionth. We emphasize again that statistically meaningful bounds require a more involved data analysis, which goes beyond the scope of this paper. Here, though, we have provided a very detailed qualitative understanding of those bounds and associated subtleties.

5 Conclusions

In this work, we have explored a scenario where the astronomical DM is made of both PBHs and thermal particles processed through freeze-out. The latter collapse around the former during the radiation dominated era to form very dense minispikes whose large densities are the remnants of the primeval universe. We completely elucidated the structure of these ultra-compact haloes in a former publication [26]. The DM post-collapse profiles exhibit four asymptotic behaviours which we explained by the interplay between the orbital injection of particles and the allowed phase space for their capture around the central object.

Using the results of this analysis, we have constructed in this article a simple and fairly accurate approximation, dubbed soft, for the DM density profile. Once the WIMP mass m_{χ} and kinetic decoupling temperature $T_{\rm kd}$ are specified, the phase space diagram in the radius vs PBH mass plane is completely set, together with critical masses M_1 and M_2 . By comparing these values with $M_{\rm BH}$, it is straightforward to determine the asymptotic behaviors of the density ρ as a function of radius \tilde{r} . The soft approximation combines these behaviors to yield a density that behaves smoothly and is satisfactorily close to the numerical result. Using it requires just a few lines of code and is extremely fast, in contrast with the numerical integration.

We have then focused on the minispike annihilation rate $\Gamma_{\rm BH}$. The on-going annihilation of DM species constantly reshapes the structure of minispikes. We have heuristically described this remodeling by the existence of an annihilation plateau, which results from the beheading of the central parts of minispikes. Its density $\rho_{\rm sat}$ can be associated to a critical value $M_{\rm T}$ of PBH mass that delineates two specific asymptotic behaviors of the density ρ . We have thoroughly analyzed how $\Gamma_{\rm BH}$ depends on WIMP parameters and redshift. We have explained these dependencies by the interplay between PBH mass $M_{\rm BH}$, transition mass $M_{\rm T}$ and critical mass $M_{\rm I}$, and identifed three asymptotic regimes for the minispike annihilation rate. By correcting the soft approximation near the surface of minispikes, we have obtained values for $\Gamma_{\rm BH}$ close, almost always, within $\pm 15\%$ to those derived using the lengthy numerical calculation. In the worst case of a 1 MeV particle, the discrepancy between both results is confined in the band between -10% and +22%, while $\Gamma_{\rm BH}$ spans more than 66 orders of magnitude.

We have finally analyzed how the extragalactic γ -ray background and CMB angular distortions constrain our mixed DM scenario. We started by fixing WIMP parameters and concentrated on the fraction $f_{\rm BH}$. Our results confirm what Lacki and Beacom [22] found more than 15 years ago, i.e. primordial black holes contribute either all or almost nothing to the astronomical DM. The former possibility is excluded by a host of cosmological and astrophysical arguments [6, 7], except in the asteroid window. Until recently, this region was not constrained by observations. A recent analysis [40] sets a weak upper limit of order 55% on $f_{\rm BH}$. In that context, the bounds which we have derived are a useful complement. The fraction of DM in the form of PBHs is severely constrained, with an upper bound as low as a few billionths in the case of a 200 GeV species annihilating into $b\bar{b}$ pairs with thermal cross-section.

One of the most important results of this article is the upper bound set by minispikes on the s-wave annihilation cross-section of thermal particles. To our knowledge, this is the first time that such an analysis is performed in the context of mixed DM. The limits set by cosmological observations on $\langle \sigma_{\rm ann} v \rangle$ are astonishingly stringent, even if the contribution of

PBHs to DM is vanishingly small. This result is exciting insofar as GW observatories are currently searching for sub-solar compact objects. Should these be discovered, thermal DM species would be partially ruled out, at least those annihilating through s-wave.

This work is nevertheless a preliminary investigation of a rich and promising topic. It is meant to pave the road for further studies. As already mentioned, we have heuristically set the efficiency factor $f_{\rm eff}$ equal to 0.1 in our study on the energy injected in the post-recombination plasma by DM annihilation inside minispikes. We plan to reinvestigate the CMB constrains using the public code CLASS. The factor $f_{\rm eff}$ and redshift $z_{\rm CMB}$ of injection will be correctly taken care of.

Another project should focuse on the possibility that minispikes may appear today as bright point-like sources in the γ -ray sky. These ultra-compact haloes behave like the DM skirts potentially surrounding intermediate mass black holes. It is conceivable that the observational programs dedicated to the latter could be applied to search for the former.

Finally, we have heuristically used the plateau approximation to describe how annihilations reshape the inner profiles of minispikes as the universe expands. This is correct if DM particles move along circular orbits around the central black hole, which is not quite the case for minispikes. In that context, some analyses [28, 29] indicate that the saturation plateau should be replaced by a weak cusp with slope lying between 0 and 1/2. But these studies explore the formation of black holes at the centers of already existing DM clumps during the matter dominated era. In our case, the context is different since DM collapses during the radiation era around already existing PBHs. The initial phase space density is also completely determined in our case, with a velocity distribution far from spherical. An analysis dedicated to this problem should be undertaken. This would make our bounds on the annihilation cross-section firmer, and would also allow us to deal with p-wave annihilating species.

Acknowledgments

We are indebted to Thomas Lacroix and Martin Stref for their participation in the very early stages of this work. We would also like to thank Vivian Poulin, Pearl Sandick, and Tracy Slatyer for inspiring discussions on aspects complementary to this paper. P.S. would like to thank colleagues from LUPM for several visits during which part of this work has been completed. This work has benefited financial support from the ANR project ANR-18-CE31-0006 (GaDaMa), and from European Union's Horizon 2020 research and innovation program under the Marie Skłodowska-Curie grant agreement N° 860881-HIDDeN—in addition to recurrent public funding from CNRS, the University of Montpellier, and the University of Savoie-Mont-Blanc.

A Accelerating the code

In order to accelerate the code, a few quantities of interest can be calculated beforehand once and for all, and stored in tables. Once the code runs, these quantities can be interpolated from these tables very quickly and with excellent precision. We give here a few examples of this procedure.

A.1 DM cosmological density ρ_i as a function of radius \tilde{r}

A key issue in the calculation of the DM minispike density surrounding a PBH is the precollapse density profile ρ_i . DM species located at radius \tilde{r} start to fall onto the black hole at cosmological time t_i , when they enter inside the gravitational horizon of the object. At that precise moment, the radius \tilde{r} can be identified with the radius \tilde{r}_{inf} of the sphere of influence. The pre-collapse density ρ_i is furthermore the DM cosmological density at time t_i , hence a unique relation between cosmological time t_i , plasma temperature T_i , DM cosmological density ρ_i , plasma density ρ_{tot} and radius of influence $\tilde{r} \equiv \tilde{r}_{inf}$. We can tabulate in advance the relation between ρ_i and the radius in the case of a 1 M_{\odot} PBH. As the code runs, we can very easily derive for any given PBH mass the pre-collapse DM density from the radius, or proceed reversely.

We first want to derive the pre-collapse DM density ρ_i from the radius \tilde{r} around a PBH with mass $m = M_{\rm BH}/{\rm M_{\odot}}$. Relation (2.16) allows to rescale the radius \tilde{r} into the radius \tilde{r}_0 corresponding to a 1 ${\rm M_{\odot}}$ black hole. At time t_i , the radii of influence \tilde{r} and \tilde{r}_0 are related to the plasma density $\rho_{\rm tot}$ through

$$\rho_{\text{tot}}(t_i)\,\tilde{r}_0^3 = \rho_{\text{tot}}(t_i)\,m^2\,\tilde{r}^3 = \rho_{\text{S}}^0\,,\tag{A.1}$$

with $\rho_{\rm S}^0$ a constant defined in Eq. (2.17). Once the radius \tilde{r} and the PBH mass m are given, the rescaling of the radius for a 1 M_{\odot} object takes the form

$$\tilde{r}_0 = \tilde{r} \ m^{2/3} \,.$$
 (A.2)

To proceed any further and calculate the cosmological DM density ρ_i corresponding to \tilde{r}_0 , i.e. to the epoch t_i and temperature T_i at which the radius of influence of a 1 M $_{\odot}$ PBH is actually equal to \tilde{r}_0 , we need to use a few ingredients. To commence, the energy and entropy densities of the primordial plasma at temperature T_i are given by

$$\rho_{\text{tot}}(T_i) = \frac{\pi^2}{30} g_{\text{eff}}(T_i) T_i^4 \text{ and } S_{\text{tot}}(T_i) = \frac{2\pi^2}{45} h_{\text{eff}}(T_i) T_i^3,$$
(A.3)

where g_{eff} and h_{eff} denote respectively the effective number of degrees of freedom (spin states) relative to energy and entropy. As the universe expands adiabatically, the product $\mathcal{S}_{\text{tot}}(T_i) a^3$, where a is the scale factor at time t_i , is furthermore constant. Finally, the cosmological DM density ρ_i at time t_i is related to the present DM density ρ_{dm}^0 through

$$\rho_i(t_i) = \frac{\rho_{\rm dm}^0}{a^3} \,, \tag{A.4}$$

with a the scale factor at time t_i . The Planck collaboration [34] has measured $\rho_{\rm dm}^0$ to be equal to $2.25401 \times 10^{-30} {\rm g \ cm^{-3}}$. At matter-radiation equality, this translates into a cosmological DM density of $\rho_i^{\rm eq} \simeq 8.88262 \times 10^{-20} {\rm g \ cm^{-3}}$.

Tossing these ingredients together, we can readily relate the cosmological DM density ρ_i at time t_i and temperature T_i to its value ρ_i^{eq} at matter-radiation equality through

$$\rho_i \equiv \rho_{\rm dm}(t_i) = \rho_i^{\rm eq} \left\{ \frac{\tilde{r}_{\rm eq}^0}{\tilde{r}_0} \right\}^{9/4} \left\{ \frac{g_{\rm eff}(T_{\rm eq})}{g_{\rm eff}(T_i)} \right\}^{3/4} \left\{ \frac{h_{\rm eff}(T_i)}{h_{\rm eff}(T_{\rm eq})} \right\}. \tag{A.5}$$

At matter-radiation equality, the reduced radius of influence of a 1 M $_{\odot}$ black hole is found to be $\tilde{r}_{\rm eq}^0 = 2.87404 \times 10^{11}$. We recover the $\tilde{r}^{-9/4}$ scaling of the second relation of Eq. (2.2). Notice that for any given PBH mass, the ratio $\tilde{r}/\tilde{r}_{\rm eq}$ is always equal to $\tilde{r}_0/\tilde{r}_{\rm eq}^0$. In our code, we have tabulated the combination

$$\frac{\rho_i}{\rho_i^{\text{eq}}} \times \left\{ \frac{\tilde{r}_0}{\tilde{r}_{\text{eq}}^0} \right\}^{9/4} \equiv \left\{ \frac{g_{\text{eff}}(T_{\text{eq}})}{g_{\text{eff}}(T_i)} \right\}^{3/4} \left\{ \frac{h_{\text{eff}}(T_i)}{h_{\text{eff}}(T_{\text{eq}})} \right\} \equiv \mathcal{C}_1(T_i), \tag{A.6}$$

as a function of the ratio $\tilde{r}_{\rm eq}^0/\tilde{r}_0$. The factor C_1 is a very slowly growing function of temperature. It actually increases from 1 at matter-radiation equality up to 3.43074 at 100 TeV. The table can be built once and for all as follows.

- Scan over \tilde{r}_0 from \tilde{r}_{eq}^0 downward.
- Use relation (A.1) to derive the plasma energy density ρ_{tot} from \tilde{r}_0 .
- Compute the plasma temperature T_i corresponding to this density ρ_{tot} . Since g_{eff} is a slowly varying function of the temperature, relation (A.3) can be used together with dichotomy.
- Compute the coefficient C_1 from Eq. (A.6) and store it together with the ratio $\tilde{r}_{\rm eq}^0/\tilde{r}_0$.

Once the table is built, our code uses it to derive quickly ρ_i as a function of \tilde{r} . Here are the steps of the procedure.

- From the input radius \tilde{r} (corresponding to PBH mass m), use Eq. (A.2) to derive \tilde{r}_0 (corresponding to a 1 M $_{\odot}$ black hole).
- Compute the ratio $\tilde{r}_{\rm eq}^0/\tilde{r}_0$.
- Interpolate in the table to get the value of C_1 .
- Use finally relation (A.6) to get the cosmological DM density ρ_i .

A.2 Influence radius \tilde{r} as a function of DM cosmological density ρ_i

Our calculation of the annihilation rate $\Gamma_{\rm BH}$ requires to know the influence radius \tilde{r} at which the DM cosmological density is ρ_i . The procedure of appendix A.1 must be inverted. The line of reasoning is still the same: at cosmological time t_i and temperature T_i , the radius of influence of a PBH with mass m is \tilde{r} , while the DM cosmological density is ρ_i . All these quantities are related through expressions given in appendix A.1. We can slightly modify Eq. (A.6) to get

$$\frac{\tilde{r}_0}{\tilde{r}_{\rm eq}^0} \times \left\{ \frac{\rho_i}{\rho_i^{\rm eq}} \right\}^{4/9} \equiv \left\{ \frac{g_{\rm eff}(T_{\rm eq})}{g_{\rm eff}(T_i)} \right\}^{1/3} \left\{ \frac{h_{\rm eff}(T_i)}{h_{\rm eff}(T_{\rm eq})} \right\}^{4/9} \equiv \mathcal{C}_2(T_i), \tag{A.7}$$

We can store beforehand the ratio $\rho_i/\rho_i^{\text{eq}}$ together with coefficient $C_2 \equiv C_1^{4/9}$ inside a table which we construct through several steps.

- Scan over ρ_i from ρ_i^{eq} upward.
- The coefficient C_2 is also a slowly varying function of plasma temperature T_i . It increases from 1 at matter-radiation equality up to 1.72962 at 100 TeV. Since C_2 is bounded by 1 and 2, we can use these values to derive the extreme radii $\tilde{r}_0^{\rm m}$ and $\tilde{r}_0^{\rm M}$ within which lies the true radius \tilde{r}_0 .
- Dichotomy can be used between the radii \tilde{r}_0^{m} and \tilde{r}_0^{M} to get the solution of Eq. (A.7). Once a value of \tilde{r}_0 is chosen, derive the corresponding plasma temperature T_i as explained in appendix A.1 and compute C_2 . This coefficient increases with increasing T_i and decreasing \tilde{r}_0 . At each step of the dichotomy, compare the left-hand side term of relation (A.7) with the value obtained for C_2 . If the former is larger than the latter, decrease \tilde{r}_0 . Otherwise, increase it. After a few tens of iterations, the solution of Eq. (A.7) is obtained.
- Store in a table the ratio $\rho_i/\rho_i^{\text{eq}}$ and the coefficient \mathcal{C}_2 .

When the code is running, it can quickly derive the radius \tilde{r}_0 from the cosmological DM density ρ_i as follows.

- From ρ_i compute the ratio $\rho_i/\rho_i^{\text{eq}}$.
- Use the table to interpolate the correct value of C_2 .
- Relation (A.7) readily yields the radius \tilde{r}_0 of the sphere of influence of a 1 M $_{\odot}$ PBH at the exact moment t_i for which the cosmological DM density is equal to ρ_i .
- Invert Eq. (A.2) to derive the radius \tilde{r} corresponding to the PBH mass m.

A.3 Calculation of v'

To derive the solution \tilde{r}_t of Eq. (2.29), we need to compute the cosmological DM density ρ_i^t at the exact time t_t and corresponding plasma temperature T_t at which the radius of influence of the PBH is equal to \tilde{r}_t . Inspired by relation (A.5), we can express ρ_i^t as a function of the cosmological DM density ρ_i^{kd} at kinetic decoupling. Keeping in mind that the ratio $\tilde{r}_t/\tilde{r}_{kd}$ does not depend on PBH mass m, this yields

$$\rho_i^{\rm t} \equiv \rho_{\rm dm}(t_{\rm t}) = \rho_i^{\rm kd} \left\{ \frac{\tilde{r}_{\rm kd}}{\tilde{r}_{\rm t}} \right\}^{9/4} \left\{ \frac{g_{\rm eff}(T_{\rm kd})}{g_{\rm eff}(T_{\rm t})} \right\}^{3/4} \left\{ \frac{h_{\rm eff}(T_{\rm t})}{h_{\rm eff}(T_{\rm kd})} \right\}. \tag{A.8}$$

The radius $\tilde{r}_{\rm t}$ of transition between the asymptotic regimes of radial infall fulfills the equation

$$\frac{\tilde{r}_{t}}{\tilde{r}_{kd}} = \upsilon \left\{ \frac{g_{\text{eff}}(T_{kd})}{g_{\text{eff}}(T_{t})} \right\} \left\{ \frac{h_{\text{eff}}(T_{t})}{h_{\text{eff}}(T_{kd})} \right\}^{4/3} \equiv \upsilon \, \mathcal{C}_{3}(T_{t}), \qquad (A.9)$$

where $\tilde{r}_t = \tilde{r}_{inf}(T_t)$ and $\tilde{r}_{kd} = \tilde{r}_{inf}(T_{kd})$. The coefficient C_3 is a very slowly increasing function of temperature insofar as

$$C_3(T_t) = \{C_1(T_t)/C_1(T_{kd})\}^{4/3}.$$
 (A.10)

The solution of Eq. (A.9) can be derived with the help of a dichotomy starting from the bounding values $\tilde{r}_{t}^{m} = \tilde{r}_{kd}$ and $\tilde{r}_{t}^{M} = v\,\tilde{r}_{kd}$. At the former (latter) bound, the left-hand side term of Eq. (A.9) is smaller (larger) than its right-hand side term. The plasma temperature

is actually equal to $T_{\rm kd}$ at the influence radius $\tilde{r}_{\rm t}^{\rm m}$. Notice also that function C_3 increases with $T_{\rm t}$ and decreases with influence radius $\tilde{r}_{\rm t}$. Before running the code, we can store in a table the values of $v' \equiv \tilde{r}_{\rm t}/\tilde{r}_{\rm kd}$ as a function of kinetic decoupling temperature $T_{\rm kd}$. The procedure is as follows.

- Scan over $T_{\rm kd}$ from $T_{\rm eq} = 7.99240 \times 10^{-10}$ GeV upward.
- At fixed $T_{\rm kd}$, derive the solution $\tilde{r}_{\rm t}$ of Eq. (A.9) using the above mentioned dichotomy. If the left-hand side term of Eq. (A.9) is larger than its right-hand side term, decrease $\tilde{r}_{\rm t}$. Otherwise increase it. The solution is obtained after a few tens of iterations.
- Store in a table the pre-calculated values of $T_{\rm kd}$ and v'.

Later on, as the code is running, v' can be interpolated whenever $T_{\rm kd}$ is defined. The radius of transition $\tilde{r}_{\rm t}$ between the radial infall asymptotic regimes with slopes 3/2 and 9/4 is given by relation (2.32).

A.4 Transition between Keplerian and radial infall regimes

The radius \tilde{r}_t where the post-collapse DM profile transitions from the Keplerian regime to the radial infall regime with slope 9/4 is defined by condition (2.35). It can be derived as the solution of Eq. (2.36) where the parameters of the model, i.e. the DM mass m_{χ} and kinetic decoupling temperature $T_{\rm kd}$ as well as the PBH mass m, come into play in the definition of parameter Λ . To save time while the code is running, we can calculate in advance \tilde{r}_t as a function of Λ by solving

$$\frac{\tilde{r}_{\rm t}}{\tilde{r}_{\rm eq}} = \Lambda \left\{ \frac{g_{\rm eff}(T_{\rm eq})}{g_{\rm eff}(T_{\rm t})} \right\} \left\{ \frac{h_{\rm eff}(T_{\rm t})}{h_{\rm eff}(T_{\rm eq})} \right\}^{4/3} \equiv \Lambda \, \mathcal{C}_4(T_{\rm t}) \,. \tag{A.11}$$

The function $C_4 \equiv C_1^{4/3}$ is an increasing function of T_t .

In equation (A.11), the radius \tilde{r}_t and temperature T_t are not independent. Actually the temperature of the plasma is T_t at the cosmological time t_t when the radius of influence of the PBH is precisely equal to \tilde{r}_t . As a consequence of Eq. (2.1), the larger the temperature T_t , the larger the plasma density ρ_{tot} and the smaller the radius \tilde{r}_t . In Eq. (A.11), increasing the left-hand side term yields a decrease of the right-hand side term through T_t . The solution of (A.11) can therefore be reached through a dichotomy. We notice that the coefficient C_4 increases from 1 at T_{eq} , up to 5.17429 at 100 TeV. At fixed Λ , the solution \tilde{r}_t lies between the bounds $\tilde{r}_t^{\rm m} \equiv \Lambda \tilde{r}_{eq}$ and, say, $\tilde{r}_t^{\rm M} \equiv 6\Lambda \tilde{r}_{eq}$. We store the results as follows

- Scan over Λ from 1 downward to 10^{-20} to reach a plasma temperature of ~ 100 TeV.
- For each value of Λ , use a dichotomy starting from the bounds $\tilde{r}_{\rm t}^{\rm m}$ and $\tilde{r}_{\rm t}^{\rm M}$. If the left-hand side term of Eq. (A.11) is larger than its right-hand side term, decrease $\tilde{r}_{\rm t}$. Otherwise increase it. The solution $\tilde{r}_{\rm t}$ is obtained after a few tens of iterations.
- In a table, store in advance the values of Λ and C_4 .

As the code is running, the mass m_1 can be calculated as soon as $T_{\rm kd}$ and $x_{\rm kd}$ are defined. For each PBH mass m, Λ can be readily computed. The radius $\tilde{r}_{\rm t}$ of transition between the Keplerian and radial infall (slope 9/4) regimes can be derived as follows.

- Interpolate from the table the value of C_4 corresponding to Λ .
- For a PBH with mass m, the radius \tilde{r}_t is given by $\Lambda C_4 \tilde{r}_{eq}^0 m^{-2/3}$.

B Effect of the Schwarzschild radius on the annihilation rate $\Gamma_{\rm BH}$

In this appendix, we refine the results derived in section 3.2. The integral \mathcal{J}_{BH} defined in Eq. (3.10) is now performed from the Schwarzschild radius of the central black hole by setting the lower bound \tilde{r}_{min} equal to 1. The new expressions for \mathcal{K}_{BH} are collected in section B.1 if a saturation plateau is assumed in the inner parts of minispikes, and in section B.2 if a weak cusp with slope 1/2 is assumed instead, as some numerical simulations suggest [28, 29].

B.1 Slope 0 and the saturation plateau

We use the saturation density and the PBH mass to classify the various configurations.

• $\rho_{\rm sat} \le \rho_{\rm B_1}$

$$-M_{\rm BH} \le M_{\rm T}$$

$$\mathcal{K}_{\rm BH} = 1 - \frac{1}{\tilde{r}_{\rm T}^3} + 2 \ln \left\{ \frac{M_{\rm T}}{M_{\rm BH}} \right\}. \tag{B.1}$$

 $-M_{\rm T} \leq M_{\rm BH}$

$$\mathcal{K}_{\rm BH} = \left\{ \frac{M_{\rm T}}{M_{\rm BH}} \right\}^2 \left\{ 1 - \frac{1}{\tilde{r}_{\rm eq}^3} \right\} \text{ if } \tilde{r}_{\rm eq} \ge 1 \text{ and } 0 \text{ otherwise.}$$
 (B.2)

For super-heavy black holes, the radius of the minispike may be less than 1. The entire DM distribution vanishes inside the black hole horizon. This occurs for $\tilde{r}_{eq} \leq 1$ which, by virtue of Eq. (2.15), translates into

$$m \ge (\tilde{r}_{\rm eq}^0)^{3/2}$$
 or $M_{\rm BH} \ge 1.54 \times 10^{17} \,\mathrm{M}_{\odot}$. (B.3)

This critical value corresponds appproximately to the heaviest black hole that can form at matter-radiation equality. The mass M_c enclosed inside the causal horizon at that epoch is actually given by

$$M_{\rm c} = \frac{4}{3}\pi r_{\rm c}^3 \rho_{\rm tot}(t_{\rm eq})$$
 where $r_{\rm c} = c t_{\rm eq}$. (B.4)

We get $4.98 \times 10^{16} \,\mathrm{M}_{\odot}$, i.e. a factor of 3 below the PBH mass previously derived.

• $\rho_{\rm B_1} \leq \rho_{\rm sat} \leq \rho_{\rm B_2}$

 $-M_{\rm BH} \leq M_1$

$$\mathcal{K}_{\rm BH} = 1 - \frac{1}{\tilde{r}_{\rm T}^3} + 3 \ln \left\{ \frac{\tilde{r}_{\rm eq}}{\tilde{r}_{\rm T}} \right\}. \tag{B.5}$$

 $-M_1 \le M_{\rm BH} \le M_{\rm T}$

$$\mathcal{K}_{\rm BH} = 3 - \frac{1}{\tilde{r}_{\rm T}^3} + 3\ln\left\{\frac{\tilde{r}_{\rm J}}{\tilde{r}_{\rm T}}\right\} - 2\left\{\frac{\tilde{r}_{\rm J}}{\tilde{r}_{\rm eq}}\right\}^{3/2}.$$
 (B.6)

 $-M_{\rm T} \le M_{\rm BH}$

Depending on the values of $\tilde{r}_{\rm H}$ and $\tilde{r}_{\rm E} \equiv \tilde{r}_{\rm eq}$ with respect to 1 (Schwarzschild radius), three possibilities can be distinguished. As long as $1 \leq \tilde{r}_{\rm H}$, we get

$$\mathcal{K}_{\rm BH} = \left\{ \frac{M_{\rm T}}{M_{\rm BH}} \right\}^2 \left\{ 3 - \frac{1}{\tilde{r}_{\rm H}^3} - 2 \left(\tilde{r}_{\rm H} / \tilde{r}_{\rm E} \right)^{3/2} \right\}. \tag{B.7}$$

For heavier black holes, $\tilde{r}_{\rm H}$ becomes smaller than 1 while the surface of the minispike lies outside the horizon. This yields

$$\mathcal{K}_{\rm BH} = 2 \left\{ \frac{M_{\rm T}}{M_{\rm BH}} \right\}^2 \tilde{r}_{\rm H}^{3/2} \left\{ 1 - \frac{1}{\tilde{r}_{\rm eq}^{3/2}} \right\}.$$
(B.8)

The integral \mathcal{K}_{BH} vanishes whenever $\tilde{r}_{eq} \leq 1$. This extreme case would correspond to super-heavy objects which cannot exist at matter-radiation equality since their formation would violate causality.

B.2 Slope 1/2

If the saturation plateau is replaced by a weak cusp with slope 1/2, the previous expressions for \mathcal{K}_{BH} are slightly modified as follows.

• $\rho_{\rm sat} \le \rho_{\rm B_1}$

$$-M_{\rm BH} \le M_{\rm T}$$

$$\mathcal{K}_{\rm BH} = \frac{3}{2} \left\{ 1 - \frac{1}{\tilde{r}_{\rm T}^2} \right\} + 2 \ln \left\{ \frac{M_{\rm T}}{M_{\rm BH}} \right\}.$$
(B.9)

 $-M_{\rm T} \leq M_{\rm BH}$

$$\mathcal{K}_{\rm BH} = \frac{3}{2} \left\{ \frac{M_{\rm T}}{M_{\rm BH}} \right\}^2 \left\{ 1 - \frac{1}{\tilde{r}_{\rm eq}^2} \right\} \text{ if } \tilde{r}_{\rm eq} \ge 1 \text{ and } 0 \text{ otherwise.}$$
 (B.10)

• $\rho_{\rm B_1} \le \rho_{\rm sat} \le \rho_{\rm B_2}$

$$-M_{\rm BH} \leq M_1$$

$$\mathcal{K}_{\rm BH} = \frac{3}{2} \left\{ 1 - \frac{1}{\tilde{r}_{\rm T}^2} \right\} + 3 \ln \left\{ \frac{\tilde{r}_{\rm eq}}{\tilde{r}_{\rm T}} \right\}. \tag{B.11}$$

 $-M_1 \le M_{\rm BH} \le M_{\rm T}$

$$\mathcal{K}_{\rm BH} = \frac{7}{2} - \frac{3}{2\tilde{r}_{\rm T}^2} + 3\ln\left\{\frac{\tilde{r}_{\rm J}}{\tilde{r}_{\rm T}}\right\} - 2\left\{\frac{\tilde{r}_{\rm J}}{\tilde{r}_{\rm eq}}\right\}^{3/2}.$$
 (B.12)

 $-M_{\rm T} \leq M_{\rm BH}$

As for the saturation plateau, three cases can be identified. We start with $1 \leq \tilde{r}_{\rm H}$ for which we get

$$\mathcal{K}_{\rm BH} = \left\{ \frac{M_{\rm T}}{M_{\rm BH}} \right\}^2 \left\{ \frac{7}{2} - \frac{3}{2\tilde{r}_{\rm H}^2} - 2\left(\tilde{r}_{\rm H}/\tilde{r}_{\rm E}\right)^{3/2} \right\}.$$
(B.13)

For heavier black holes, $\tilde{r}_{\rm H}$ is smaller than 1 while the minispike radius $\tilde{r}_{\rm E} \equiv \tilde{r}_{\rm eq}$ exceeds the Schwarzschild radius of the central object. This yields

$$\mathcal{K}_{\rm BH} = 2 \left\{ \frac{M_{\rm T}}{M_{\rm BH}} \right\}^2 \tilde{r}_{\rm H}^{3/2} \left\{ 1 - \frac{1}{\tilde{r}_{\rm eq}^{3/2}} \right\}.$$
(B.14)

In the last case where $\tilde{r}_{\rm eq} \leq 1$, the integral $\mathcal{K}_{\rm BH}$ vanishes.

References

- [1] S. Hawking, Gravitationally collapsed objects of very low mass, MNRAS 152 (Jan., 1971) 75.
- [2] B. J. Carr and S. W. Hawking, *Black holes in the early Universe*, MNRAS 168 (Aug., 1974) 399–416.
- [3] S. W. Hawking, Particle Creation by Black Holes, Commun. Math. Phys. 43 (1975) 199–220.
- [4] G. Dvali, L. Eisemann, M. Michel and S. Zell, *Black hole metamorphosis and stabilization by memory burden*, *Phys. Rev. D* **102** (Nov., 2020) 103523, [2006.00011].
- [5] G. F. Chapline, Cosmological effects of primordial black holes, Nature **253** (Jan., 1975) 251–252.
- [6] B. J. Carr, K. Kohri, Y. Sendouda and J. Yokoyama, Constraints on primordial black holes, Reports on Progress in Physics 84 (Nov., 2021) 116902, [2002.12778].
- [7] A. M. Green and B. J. Kavanagh, *Primordial black holes as a dark matter candidate*, *Journal of Physics G Nuclear Physics* 48 (Apr., 2021) 043001, [2007.10722].
- [8] P. Eros-2 Collaboration, Tisserand, L. Le Guillou et al., Limits on the macho content of the galactic halo from the eros-2 survey of the magellanic clouds, A&A 469 (July, 2007) 387–404, [astro-ph/0607207].
- [9] A. M. Green, Microlensing and dynamical constraints on primordial black hole dark matter with an extended mass function, Phys. Rev. D 94 (Sept., 2016) 063530, [1609.01143].
- [10] M. Petač, J. Lavalle and K. Jedamzik, Microlensing constraints on clustered primordial black holes, Phys. Rev. D 105 (Apr., 2022) 083520, [2201.02521].
- [11] S. Bird, I. Cholis, J. B. Muñoz, Y. Ali-Haïmoud, M. Kamionkowski, E. D. Kovetz et al., *Did LIGO Detect Dark Matter?*, *Phys. Rev. Lett.* **116** (May, 2016) 201301, [1603.00464].
- [12] M. Sasaki, T. Suyama, T. Tanaka and S. Yokoyama, Primordial Black Hole Scenario for the Gravitational-Wave Event GW150914, Phys. Rev. Lett. 117 (Aug., 2016) 061101, [1603.08338].
- [13] M. Raidal, V. Vaskonen and H. Veermäe, Formation of primordial black hole binaries and their merger rates, arXiv e-prints (Apr., 2024) arXiv:2404.08416, [2404.08416].
- [14] G. Hütsi, M. Raidal, V. Vaskonen and H. Veermäe, Two populations of ligo-virgo black holes, J. Cosmology Astropart. Phys. 2021 (Mar., 2021) 068, [2012.02786].
- [15] G. Arcadi, D. Cabo-Almeida, M. Dutra, P. Ghosh, M. Lindner, Y. Mambrini et al., *The waning of the wimp: endgame?*, European Physical Journal C 85 (Mar., 2025) 152, [2403.15860].
- [16] N. Bernal, M. Heikinheimo, T. Tenkanen, K. Tuominen and V. Vaskonen, The dawn of FIMP Dark Matter: A review of models and constraints, International Journal of Modern Physics A 32 (Sept., 2017) 1730023–274, [1706.07442].
- [17] L. Di Luzio, M. Giannotti, E. Nardi and L. Visinelli, *The landscape of qcd axion models*, *Phys. Rep.* **870** (July, 2020) 1–117, [2003.01100].
- [18] P. S. Cole, A. D. Gow, C. T. Byrnes and S. P. Patil, Primordial black holes from single-field inflation: a fine-tuning audit, J. Cosmology Astropart. Phys. 2023 (Aug., 2023) 031, [2304.01997].
- [19] M. Ricotti, Bondi accretion in the early universe, ApJ 662 (June, 2007) 53–61, [0706.0864].
- [20] K. J. Mack, J. P. Ostriker and M. Ricotti, Growth of Structure Seeded by Primordial Black Holes, Ap.J 665 (Aug., 2007) 1277–1287, [astro-ph/0608642].
- [21] M. Ricotti, J. P. Ostriker and K. J. Mack, Effect of primordial black holes on the cosmic microwave background and cosmological parameter estimates, ApJ 680 (June, 2008) 829–845, [0709.0524].

- [22] B. C. Lacki and J. F. Beacom, Primordial Black Holes as Dark Matter: Almost All or Almost Nothing, ApJ 720 (Sept., 2010) L67–L71, [1003.3466].
- [23] E. Barausse, V. Cardoso and P. Pani, Can environmental effects spoil precision gravitational-wave astrophysics?, Phys. Rev. D 89 (May, 2014) 104059, [1404.7149].
- [24] B. J. Kavanagh, D. A. Nichols, G. Bertone and D. Gaggero, Detecting dark matter around black holes with gravitational waves: Effects of dark-matter dynamics on the gravitational waveform, Phys. Rev. D 102 (Oct., 2020) 083006, [2002.12811].
- [25] Y. N. Eroshenko, Dark matter density spikes around primordial black holes, Astronomy Letters 42 (June, 2016) 347–356, [1607.00612].
- [26] M. Boudaud, T. Lacroix, M. Stref, J. Lavalle and P. Salati, In-depth analysis of the clustering of dark matter particles around primordial black holes. Part I. Density profiles, J. Cosmology Astropart. Phys. 2021 (Aug., 2021) 053, [2106.07480].
- [27] J. Adamek, C. T. Byrnes, M. Gosenca and S. Hotchkiss, WIMPs and stellar-mass primordial black holes are incompatible, Phys. Rev. D 100 (July, 2019) 023506, [1901.08528].
- [28] E. Vasiliev, Dark matter annihilation near a black hole: Plateau vs. weak cusp, Phys. Rev. D 76 (2007) 103532, [0707.3334].
- [29] S. L. Shapiro and J. Shelton, Weak annihilation cusp inside the dark matter spike about a black hole, Phys. Rev. D 93 (2016) 123510, [1606.01248].
- [30] S. M. Boucenna, F. Kühnel, T. Ohlsson and L. Visinelli, Novel constraints on mixed dark-matter scenarios of primordial black holes and WIMPs, J. Cosmology Astropart. Phys. 2018 (July, 2018) 003, [1712.06383].
- [31] B. Carr, F. Kühnel and L. Visinelli, Black holes and WIMPs: all or nothing or something else, MNRAS 506 (Sept., 2021) 3648–3661, [2011.01930].
- [32] P. Chanda, J. Scholtz and J. Unwin, Improved constraints on dark matter annihilations around primordial black holes, Journal of High Energy Physics 2024 (July, 2024) 273, [2209.07541].
- [33] E. U. Ginés, O. Mena and S. J. Witte, Revisiting constraints on WIMPs around primordial black holes, Phys. Rev. D 106 (Sept., 2022) 063538, [2207.09481].
- [34] Planck Collaboration et al., Planck 2018 results. VI. Cosmological parameters, A&A 641 (Sept., 2020) A6, [1807.06209].
- [35] D. J. Fixsen, The Temperature of the Cosmic Microwave Background, ApJ **707** (Dec., 2009) 916–920, [0911.1955].
- [36] FERMI-LAT collaboration, M. Ackermann et al., The spectrum of isotropic diffuse gamma-ray emission between 100 MeV and 820 GeV, ApJ 799 (2015) 86, [1410.3696].
- [37] S. Ando and K. Ishiwata, Constraints on decaying dark matter from the extragalactic gamma-ray background, J. Cosmology Astropart. Phys. **2015** (May, 2015) 024–024, [1502.02007].
- [38] C. Blanco and D. Hooper, Constraints on Decaying Dark Matter from the Isotropic Gamma-Ray Background, JCAP 03 (2019) 019, [1811.05988].
- [39] D. P. Finkbeiner, S. Galli, T. Lin and T. R. Slatyer, Searching for dark matter in the cmb: A compact parametrization of energy injection from new physics, Phys. Rev. D 85 (Feb., 2012).
- [40] N. Esser, C. Filion, S. De Rijcke, N. Kallivayalil, H. Richstein, P. Tinyakov et al., Constraints on asteroid-mass primordial black holes in dwarf galaxies using Hubble Space Telescope photometry, A&A 698 (2025) A290, [2503.03352].